

BEHAVIOR OF HIGHLY TE DOPED INGAAS

By

ETHAN LOWELL KENNON

A DISSERTATION PRESENTED TO THE GRADUATE SCHOOL  
OF THE UNIVERSITY OF FLORIDA IN PARTIAL FULFILLMENT  
OF THE REQUIREMENTS FOR THE DEGREE OF  
DOCTOR OF PHILOSOPHY

UNIVERSITY OF FLORIDA

2017

© 2017 Ethan Lowell Kennon

To my parents.

## ACKNOWLEDGMENTS

I would be lost without the support from my family and friends throughout graduate school. My advisors and lab-mates have been instrumental in taking on this work, for which I thank them dearly. I am also indebted to the support staff at the University of Florida since they have always kept equipment up and running.

## TABLE OF CONTENTS

	<u>page</u>
ACKNOWLEDGMENTS.....	4
LIST OF TABLES.....	7
LIST OF FIGURES.....	8
LIST OF ABBREVIATIONS.....	11
ABSTRACT .....	13
 CHAPTER	
1 INTRODUCTION AND MOTIVATION.....	14
Moore's Law .....	14
Physics of Electrical Conduction.....	16
Physics of Doping .....	23
Transistor Operation .....	27
Power Dissipation Challenges .....	31
Benefits of III-Vs Over Si.....	32
Challenges to III-V Integration .....	33
2 DOPANT STABILITY AND INCORPORATION METHODS .....	41
Dopant Saturation.....	41
Achieving Supersaturation .....	43
Returning Supersaturated Doping to Equilibrium.....	44
Growth From a Melt .....	46
Ion Implantation .....	48
Molecular Beam Epitaxy .....	50
Metal Organic Chemical Vapor Deposition .....	53
Opportunity for Study of Te.....	56
3 ANALYSIS TECHNIQUES.....	59
Hall Effect .....	59
Transmission Electron Microscopy .....	61
Focused Ion Beam Milling.....	63
X-Ray Diffraction.....	65
Secondary Ion Mass Spectrometry.....	67
Atomic Force Microscopy.....	70
4 ELECTRICAL DEACTIVATION OF SUPERSATURATED TE DOPING IN INGAAS .....	72

Deactivation of Heavily Te Doped Material .....	72
Growth Parameters.....	72
Sample Surface Protection .....	73
Hall Effect Results .....	76
Arrhenius Relation .....	79
Consistent Equilibrium Activation.....	79
No Clustering Visible.....	80
Summary .....	81
<b>5 EXPERIMENTAL INVESTIGATION OF POINT DEFECTS AND TE DOPING .....</b>	<b>88</b>
Strain of Te .....	88
X-Ray Diffraction Results.....	89
Early SIMS Results.....	90
Polishing of ALD Caps .....	91
AFM Results .....	92
Revisiting Atomic Layer Deposition .....	93
Te Diffusion.....	95
Diffusion Modelling .....	95
Marker Layer.....	97
Modifying Deactivation Kinetics .....	99
Strain.....	99
Ion Implantation.....	102
Summary .....	104
<b>6 AB INITIO MODELLING .....</b>	<b>124</b>
Basis of DFT .....	124
Bloch's Theorem.....	126
K-points .....	127
Plane Waves .....	128
GaAs Results.....	129
Single Defects .....	129
Defect Clusters.....	130
Clusters of Multiple Te Atoms.....	132
InAs Results.....	133
Summary .....	133
<b>7 CONCLUSIONS .....</b>	<b>145</b>
<b>LIST OF REFERENCES .....</b>	<b>148</b>
<b>BIOGRAPHICAL SKETCH.....</b>	<b>164</b>

## LIST OF TABLES

<u>Table</u>	<u>page</u>
6-1 Supercell energies for the elements, perfect cell and single defects. ....	135
6-2 Single point defect formation energies. ....	136
6-3 Reaction energies for Te-Te clusters.....	138
6-4 Reaction energies for Te-point defect complexes.....	141
6-5 Reaction energies for two Te atoms clustering to a Ga vacancy. ....	142
6-6 Reaction energies for multi-atom intrinsic point defect formation. ....	143
6-7 InAs reaction energies.....	144

## LIST OF FIGURES

<u>Figure</u>	<u>page</u>
1-1 Trend showing the continuation of Moore's law into modern devices, even when pushing against fundamental limits like the ability to dissipate excess heat. Replotted data from [32]. .....	35
1-2 Plot of allowed electron energy levels vs atomic spacing showing the formation of bands in carbon. Replotted data from [33]. .....	36
1-3 The Fermi-Dirac function showing the temperature trends of the probability of an electron energy state being occupied at different temperatures. ....	37
1-4 E vs. k diagram showing the band structure for GaAs. Replotted with data from [34]. .....	38
1-5 Semiconductor depletion and band bending at pn junction formation. ....	39
1-6 A basic planar NMOS transistor. ....	40
2-1 Deactivation of heavily Te doped InGaAs after 10 minute anneals at varying temperature. ....	58
4-1 Final InGaAs structures for heavily Te doped and control samples with 50nm Si marker layer buried 150 nm below the Te layer. ....	82
4-2 Hall Effect data for a time series of anneals at 700°C showing the minimal change in the control sample and deactivation of Te from $4.4 \times 10^{14} \text{ cm}^{-2}$ to $7 \times 10^{13} \text{ cm}^{-2}$ . The smooth fits the data to extract a deactivation rate .....	82
4-3 Deactivation curves for all anneal temperatures on a log time plot with all anneal temperatures deactivating to a similar value of $7\text{-}8 \times 10^{19} \text{ cm}^{-3}$ . The dotted line represents the starting carrier concentration for all samples. ....	83
4-4 Mobility changes in the Te doped samples during deactivation. Mobility increases, but not nearly to the level of the undoped material, meaning that there is still some defect scattering lowering the electron mobility.....	84
4-5 Mobility changes in the undoped samples during the same anneals as the deactivating Te doped samples. ....	85
4-6 Comparison of mobility and carrier concentration during deactivation.....	86
4-7 Arrhenius plot of electrical deactivation time constants over all anneal temperatures, showing an activation energy for the deactivation mechanism of 2.6 eV .....	87



4-8	TEM of the MOCVD grown InGaAs structure after a 700 °C 30 second anneal.....	87
5-1	XRD scans off of the 400 plane showing a sharp Si peak on the right, GaAs peak in the center, and broad InP, InAlAs, and InGaAs peaks superimposed on the left.....	105
5-2	HRXRD scan around the peak for InGaAs, InAlAs, and InP. There is minimal difference between the sample with the heavily Te doped layer (red) and the control sample (blue). .....	106
5-3	Te SIMS profiles as grown, with apparent enhanced tail diffusion after 30 seconds at 700 °C, and with Fickian diffusion after 4 hours. ....	107
5-4	SIMS showing Te background concentration tracking fluorine contamination in the sample, while Si background tracks oxygen and carbon contamination. ....	108
5-5	SIMS of a sample with a polished off cap showing no carbon, oxygen, or fluorine contamination, but also having very non-abrupt interfaces. ....	109
5-6	AFM images of the sample surface after various stages of capping.....	110
5-7	A hydrogen blister in exposure ALD deposited Al <sub>2</sub> O <sub>3</sub> . ....	111
5-8	SIMS profiles of the Te layer diffusion at 700 °C showing an average diffusivity of $3.6 \times 10^{-17} \text{ cm}^2 \text{ s}^{-1}$ .....	112
5-9	Diffusivities of Te in InGaAs extracted using FLOOPS from the SIMS profiles for 700 °C anneals. ....	113
5-10	Comparison of Te diffusivity in InGaAs to values found in literature for Te diffusion in GaAs and InAs. ....	114
5-11	Diffusion profiles of the Si marker layer in the control sample with a diffusivity of $6 \times 10^{-17} \text{ cm}^2 \text{ s}^{-1}$ at 700 °C.....	115
5-12	Extracted diffusivities for the Si marker layer control sample. ....	116
5-13	Diffusion profiles of the Si marker layer in the sample with Te exhibiting the same diffusivity as the control sample. ....	117
5-14	Extracted diffusivities of Si in the Te doped sample in the same range as Si diffusivities in the undoped sample.....	118
5-15	Superimposed profiles of the Si marker layers in the control (black line) and Te doped (red line) samples.....	119

5-16	Comparison of deactivation for samples of different strain states annealed for 5 minutes at 650 °C .....	120
5-17	TEM of $7 \times 10^{14}$ cm <sup>-2</sup> As implanted sample of Te doped material showing no amorphization. A schematic representation of the implant profile is shown to the right of the image. ....	121
5-18	Deactivation of Te doped samples with varying As implant doses at 700 °C with a pronounced stabilization of the Te doping. ....	122
5-19	Deactivation of Te doped samples with varying As doses at 600 °C with less stabilization of the Te doping than occurred at 700 °C. ....	123
6-1	K-point convergence test with an energy change less than 0.01 eV per atom for a 4x4x4 k-point grid. ....	134
6-2	Energy cutoff convergence test with less than 0.001 eV per atom for an energy cutoff of 600 eV. ....	134
6-3	Supercell energies for Te-Te clusters. ....	137
6-4	Supercell energies for Te-matrix point defect clusters. ....	138
6-5	Supercell energies for two Te atoms around a Ga vacancy. ....	139
6-6	Supercell energies for intrinsic point defect clusters. ....	140

## LIST OF ABBREVIATIONS

ALD	Atomic Layer Deposition
AsH <sub>3</sub>	arsine
BF	Bright Field
BOE	Buffered Oxide Etch
CVD	Chemical Vapor Deposition
DETe	diethyltelluride
DFT	Density Functional Theory
DIBL	Drain Induced Barrier Lowering
DoS	Density of States
DP	Diffraction Pattern
EDS	Energy Dispersive X-ray Spectroscopy
EELS	Electron Energy Loss Spectroscopy
FIB	Focused Ion Beam
FLOOPS	Florida Object Oriented Process Simulator
GAA	Gate All Around
HAADF-STEM	High Angle Annular Dark Field Scanning Transmission Electron Microscopy
HF	Hydrofluoric Acid
HF	High Frequency
HRETEM	High Resolution Transmission Electron Microscopy
ITRS	International Technology Roadmap for Semiconductors
LDA	Local Density Approximation
LF	Low Frequency

LPE	Liquid Phase Epitaxy
MBE	Molecular Beam Epitaxy
MF	Mixed Frequency
MOCVD	Metal Organic Chemical Vapor Deposition
PAW	Projector Augmented Wave
PECVD	Plasma Enhanced Chemical Vapor Deposition
PMD	Permanent Marker Deposition
SEM	Scanning Electron Microscopy
SIMS	Secondary Ion Mass Spectrometry
SPEG	Solid Phase Epitaxial Growth
STEM	Scanning Transmission Electron Microscopy
TEM	Transmission Electron Microscopy
TCAD	Technology Computer Aided Design
ToF	Time of Flight
TMAI	trimethylaluminum
TMGa	trimethylgallium
TMIn	trimethylindium
VASP	Vienna Ab-initio Simulation Package
XAFS	X-ray Absorption Fine Structure
XRD	X-Ray Diffraction
XRF	X-Ray Fluorescence

Abstract of Dissertation Presented to the Graduate School  
of the University of Florida in Partial Fulfillment of the  
Requirements for the Degree of Doctor of Philosophy

BEHAVIOR OF HIGHLY TE DOPED INGAAS

By

Ethan Lowell Kennon

August 2017

Chair: Kevin Jones

Major: Materials Science and Engineering

The exponential growth of semiconductor technology has allowed it to reach the prevalence that we see today. In order for growth to continue, new materials such as InGaAs will be needed, but the contact resistivity of these materials is troublesome. Te doping of InGaAs is a potential solution to this problem, but its behavior is not fully understood. This work studied the electrical deactivation of Te doping in InGaAs, systematically determining the mechanisms that could be involved. Annealing to induce deactivation yielded an activation energy of 2.6 eV for the responsible mechanism. TEM of the layer indicated that the Te was not precipitating, leading to the conclusion that point defects or small clusters were responsible. Marker layer studies, strained deactivation, and implants were used to eliminate interstitial clustering as a possibility, and lend further support to Ga Frenkel pair formation as the deactivation mechanism. DFT calculations of GaAs and InAs confirmed these experimental results, showing Te-V clusters to be the most stable defect, and that vacancy formation cannot be the limiting factor in Te deactivation.

## CHAPTER 1 INTRODUCTION AND MOTIVATION

### **Moore's Law**

As an integral part of everyday life and responsible for significant advances in business and research, computing is a critical aspect of modern society. With automated trading on Wall Street and supercomputers running simulations for all sorts of physics and medical advances, the driver for new processors is higher efficiency and speed. Performance improvements in computers have traditionally been achieved through the trend dubbed Moore's Law after the observations of Gordon Moore in 1965[1]. He noticed that in the infancy of integrated circuits, the number of transistors, or logic devices, doubled over a fixed time scale resulting in the cost per device to be cut in half. He predicted that this trend would continue until the practically useable area of a chip would be filled, with tens of thousands of devices on a single chip. Without research into shrinking the transistors, he thought that the trend would continue for about 10 years. By that time additional engineering would be needed and the growth would slow.

In this prediction, Gordon Moore was very wrong. In 10 years' time, the engineering needed to shrink the transistors had already been developed and the trend continued, if not accelerated. He had co-founded Intel and his observation had taken on the name "Moore's Law", the driving force of the newly formed computer industry. As time wore on, the end of Moore's Law has been predicted many times, citing challenges in lithography[2], dielectric breakdown[3], short channel transistor leakage[4], statistical fluctuations[4], and power consumption[5] among many others.

Yet so far each time these challenges were overcome. Figure 1-1 shows the progression of Moore's Law up until 2015 with the number of transistors per chip still growing at an exponential rate. Lithographic challenges have been overcome with immersion lithography that increased the numerical aperture of the medium through which light was focused and shrunk feature sizes without moving to smaller wavelength light[6]. Double and even quadruple patterning have become common to divide the minimum pitch of lithographic processes even further[7]. After Dennard scaling was threatened by dielectric breakdown of  $\text{SiO}_2$ , high-k dielectrics like  $\text{HfO}_2$  enabled thicker oxides to act equivalent to thinner dielectric layers[8]. Strained channels helped further by splitting the bands of silicon such that the in plane mobility increased while simultaneously increasing the density of states out of plane with the gate[8]. Leakage from Drain Induced Barrier Lowering (DIBL) threatened on-off ratios, yet was solved by gating the transistors from both sides of a vertical fin in a FinFET that improved gate control[4]. The threshold voltage adjustment needed for shrinking devices became dependent upon statistical fluctuations with extremely small transistors, but this was replaced with work function modulation by the gate material[4]. Power consumption is still a limitation under the constant voltage scaling regime as seen in Figure 1-1. Power plateaued at the limit for what can be dissipated in air, but the number of transistors has continued its growth by limiting the time that sections of the chip are on and using multiple cores on a chip. Reductions in metal and device resistances, as well as new materials and transistor designs will be needed in the future[5, 8].

## Physics of Electrical Conduction

Semiconductors are more useful than metals or insulators for designing logic devices because of their unique electronic properties. The electronic properties of a solid are borne out of the bonding orbitals of a few atoms. The electrons are not individually discernable, so as atoms are added to the system the Pauli Exclusion Principle forces the electrons to separate in energy by the smallest amount possible. The energy difference comes from a new combination of wavefunction solutions to the same orbital  $n, l, m_l, m_s$  once multiple atoms are present. As energy levels accumulate, the discrete electron energy levels broaden out into bands until reaching a point where the electron density of the material in a complete solid yields some positional differentiation between electrons and the bands are fully formed[9]. An example of band formation based on atomic spacing is demonstrated in Figure 1-2. The energy ranges of these bands and the population of electrons in the material determine its electrical properties.

One component that is important in the comparisons going forward is the Fermi energy. This defines the point to which the electron states of the material are filled at a ground state and absolute zero temperature. This means that the material intrinsically has enough electrons to completely fill the states in its orbitals or bands up to the Fermi energy and states above the Fermi energy are unfilled. However, with the addition of energy from an external source, typically from increasing the temperature or applying an electric field, electrons can be excited above the Fermi energy, leaving electron holes, or empty states, below the Fermi energy.



If the electron bands have overlapped or the Fermi energy falls within one of the bands, the material acts as a metal. There are additional unfilled states directly above the ground electron states at absolute zero. At absolute zero, there would be no possibility for electron movement because the states below the Fermi level are completely occupied, leaving no adjacent states for electrons to move into, and there are no electrons above the Fermi energy where there are an abundance of available states for an electron to move around. Because of the continuum of states surrounding the Fermi energy, at any temperature or with any applied electrical field, electrons can easily be excited up into a higher energy state where they are then unconstrained from their bonds and free to move in physical space. Similarly, the holes left by the excited electrons leave states that other electrons can use to move around. Both types of electron motion yield easy electrical conduction as is commonly associated with metals.

This distribution of electron populations and the probability of finding an electron above or below the Fermi energy is described by the Fermi-Dirac function, demonstrated in Figure 1-3. This function formalizes the process explained above, whereby energy added to the system increases the probability of finding an electron excited to above the Fermi energy[10]. This increase in turn reduces the probability of finding an electron below the Fermi energy. At low added energies, such as low temperatures, only a few electrons can be excited and the energy they obtain is relatively small. This means that the electrons excited come from very near the Fermi energy and only go slightly above it. If the electrons are thermally excited, the temperature energy distribution follows a Gaussian profile. This means that the tail of the Gaussian with energy above a certain threshold determines the energy that can be

added to an electron. Some may be excited by a large energy, but most of the excited electrons will only have a small amount of energy above their ground state. As temperature increases, the energy available increases, so both the population of excited electrons and energy away from the Fermi level at which electrons can be excited increases. Throughout all this, the Fermi energy is unchanged. It remains the energy point at which there is a 50% chance of being occupied by an electron.

In an insulating material, the bands that come from the expanded bonding orbitals of the material do not overlap. This leads to band gaps, or energies that are still forbidden from occupancy by electrons in the material. If the Fermi level falls within one of these gaps, the bottom band is entirely filled with electrons and the band above is entirely unoccupied. For an electron to move, it would have to be promoted to an energy level across the band gap. The band just below the band gap is called the valence band because it is filled with the most weakly bound valence electrons of the material. The next band is called the conduction band because any electrons excited to this band would be able to conduct as they do in a metal. However, at room temperature and reasonable voltages, there is not enough energy to expand the Fermi-Dirac distribution across the energy width of the band gap, promoting electrons to the conduction band where they can move freely. This prevents the material from conducting, making it an insulator.

A semiconductor is a special case of insulator where the band gap is small enough that the Gaussian distribution of thermal energy at room temperature is sufficient to excite some electrons from the valence band into the conduction band. With only a small population of electrons and holes, semiconductors are able to conduct

electricity, albeit with a higher resistance than typical metals. These limited number of carriers lend us the ability to manipulate the properties of a semiconductor's conductivity through the addition of relatively small concentrations of other materials. This process, called doping, will be discussed further in the next section.

Before going into the mechanics of doping, it is also important to discuss additional restrictions on the behavior of electrical carriers in semiconductors. From the quantum mechanical perspective, the accumulation of atoms into a solid creates a periodic potential for the electrons in the material. The bands are formed when new wavefunctions separate the energy of electrons in the same orbital by a small amount[10]. At the bottom of the band, the electrons are in the lowest energy state for that band, corresponding to a wavefunction that is all spin up or spin down for every atomic potential they encounter. As you increase in energy, the wavefunction increases in energy by moving to higher order solutions which contain more nodes in their distribution. The electrons occupying the states above the bottom of the band edge have multiple nodes, so the number of wavefunctions that yield either a symmetric or antisymmetric solution across the periodic potential can yield a differentiation between electrons even with the same energy[10]. This means that more than 2 electrons can occupy that energy level because they follow different wavefunctions. This process increases with more and more possible states for electrons in one given energy until approaching the top of the band, where the possible arrangements start to be limited by the need for higher energy wavefunctions. At the top of the band, there must be a node between every atomic potential and again there are only 2 solutions. This population of electron states for a given energy within the band is called the Density of States (DoS),

and increases at energies further from the band edge because there are more states for electrons to potentially occupy. Near the band edges, where most of the important conductive properties are defined for semiconductors, the DoS can be approximated with a parabola.

When an electric field is applied to a material, the free electrons within the material experience a force caused by the applied potential. Since electrons have a negative charge, they feel a force in the direction opposite the applied field. Any holes, being the absence of an electron then move in the opposite direction from the electrons moving into the holes. Without the bias present, the carriers would still move due to thermal energy in the system, scattering off of atoms and other carriers in the system. With the bias, the carriers “drift,” being accelerated by the applied bias between scattering events. The readiness with which the carriers can be accelerated by an applied electric field is called the effective mass,  $m^*$ . This is material dependent and a function of the band structure of the material. Because the periodicity of a crystalline material is not the same in all directions, it makes sense that the bands formed by the material are not spherically uniform in three dimensions. This is in fact the case, and computed  $E$  vs.  $k$  diagrams like the one shown in Figure 1-4 reflect the difference in energy for the band edges in different orientations. The directions are represented as momentum vectors,  $k$ , for the carriers travelling in the material. Many of the bands overlap, but in this case with silicon, there is a band gap separating the top of the valence band and the bottom of the conduction band. The effective mass for electrons in the conduction band is inversely proportional to the curvature of the band at its minima, and the effective mass of holes is inversely proportional to the curvature of the

valence band maxima. The direct relationship for electrons is given as an example in Equation 1-1[11].

$$m_e^* = \hbar^2 \left( \frac{d^2 E}{dk^2} \right)^{-1} \quad 1-1$$

Where  $m_e^*$  is the effective mass for electrons,  $\hbar$  is the reduced Planck constant, and  $\left( \frac{d^2 E}{dk^2} \right)$  is the second derivative of the E vs. k curve. This can be seen as the change in momentum (k-space) needed to alter a carrier's energy level at the band edge. A sharply curved band edge would need very little change in momentum to accelerate a carrier and give it a higher energy, giving the carrier a light effective mass.

While the effective mass gives the ease of acceleration of the carriers in a field, the frequency of scattering events within the material is important as well. Scattering can occur off of the crystal lattice, impurities in the material, and extended defects such as dislocations, loops, grain boundaries, and even the semiconductor surface or interfaces with other materials. The mean scattering time  $\tau$  depends upon the scattering cross section of the scattering species  $S$ , the mean thermal velocity of the carriers  $v_{th}$ , and the density of scattering sites per volume  $N_s$ , as shown in Equation 1-2.

$$\tau = \frac{1}{S * v_{th} * N_s} \quad 1-2$$

Each time the carrier scatters randomly and any drift velocity accumulated from the electric field is lost. The carrier then begins to move freely again, being accelerated by any applied bias until another scattering event occurs. The mobility of a carrier type due to a particular scattering type,  $\mu$ , shown in Equation 1-3, is calculated from the scattering time  $\tau$ , the charge of an electron  $e$ , and the effective mass of the carrier  $m^*$ .

$$\mu = \frac{e * \tau}{m^*} \quad 1-3$$

The overall mobility for a carrier in the material follows Matthiessen's rule shown in Equation 1-4, adding the mobilities in parallel, since multiple scattering mechanisms result in an overall lower mobility.

$$\frac{1}{\mu_e} = \frac{1}{\mu_l} + \frac{1}{\mu_i} + \dots \quad 1-4$$

Here,  $\mu_e$  is the overall electron mobility,  $\mu_l$  is the mobility contribution from lattice scattering,  $\mu_i$  is the mobility contribution from ionized impurity scattering, and any additional mobility contributions for other defects or scattering. In a single crystal semiconductor, the two largest contributors to mobility are the lattice or phonon scattering and the ionized impurity scattering.

Conductivity ( $\sigma$ ) then depends upon the number of carriers,  $n$  and  $p$  for electrons and holes, their charge, which is the charge of an electron,  $e$ , and their respective overall mobilities,  $\mu_n$  and  $\mu_p$  as shown in Equation 1-5.

$$\sigma = n * e * \mu_n + p * e * \mu_p \quad 1-5$$

For a typical conductor like a metal, the number of free carriers is nearly constant since the band is partially filled and there are almost always sufficient carriers for conduction. Thus they conduct easily. At elevated temperatures, the vibrations in the lattice disrupt the periodicity of the lattice and increase the phonon scattering cross section, yielding a lower conductivity. Semiconductors are unique in their dearth of carriers at low temperatures. They depend upon the excitation of additional carriers for conduction and this process actually overwhelms the loss in mobility to create a significant increase in conductivity with increased temperature. As mentioned earlier,

doping a semiconductor allows for the insertion of additional charge carriers of a specific type without increasing the temperature.

### **Physics of Doping**

Doping is the process of intentionally adding impurities to a material in order to modify its electronic properties. Using silicon as a simple example, it readily forms into a diamond cubic structure where each atom with 4 valence electrons forms 4 bonds with its neighbors. Every bond is satisfied with two electrons, one from each Si atom. There are no extra electrons and the carriers that exist are thermally excited electrons in the conduction band which leave behind a bond to move around. In the bond where the electron used to be there is now a hole in the valence band available to be filled by an electron. Either carrier can move around and result in conduction through the Si. Within 1 cubic centimeter of Si ( $5 \times 10^{22}$  atoms) at room temperature (300K), the number of excited electrons is  $1.45 \times 10^{10}$ . At higher temperatures there would be more carriers and at lower temperatures there would be fewer down to absolute zero where there would be none. These electrons and holes are at an equilibrium between being thermally excited and coulombically attracted and recombining.

But if some of the Si atoms are replaced by another element like phosphorous which has 5 valence electrons, there will be one extra electron after 4 bonds are made to the adjacent Si atoms. Since this 9<sup>th</sup> electron is not needed to satisfy the valence shell of the P atom, it is only weakly bound to the phosphorous and will readily move into the conduction band. If the extra energy is less than the 0.026eV available at room temperature, the extra carrier is considered a shallow donor. It is safe to assume that almost all of the P atoms donate an electron and the number of electrons can easily be raised by orders of magnitude. Similarly, an atom with 3 valence electrons like B

substituted for Si would be one electron deficient from satisfying the 4 adjacent bonds and would increase the number of holes.

Not all atoms act as a shallow dopant. If a dopant atom is not bonded to the host material as a substitutional atom, it is not forced into a state where it has extra or fewer electrons. Otherwise active species can end up on interstitial sites or trapped on defects in the material depending upon the method used for dopant incorporation. Other species such as Au impurities in Si, Cr in GaAs, or Fe in InP may not bond readily to the matrix and have an ionization energy greater than the 0.026eV that is typically thermally available. Dopants with high ionization energies leave their electrons in a state somewhere in the middle of the band gap. This results in a deep level trap, since other carriers that would usually contribute to conduction can use that energy state as an intermediate to recombine with a carrier of the opposite type more readily.

Species of the same valence electron configuration as the matrix are isoelectronic, like Ge in Si, where both have 4 valence electrons and there is no change in the electron population solely as a result of adding the atom. They may still alloy and form a semiconductor with intermediate properties like lattice constant and band gap that fall between the two constituents.

Doping in III-V materials is a little more complicated since there are now group III sites and group V sites that could be occupied by the dopant atom. The host material is ideally half group III atoms and half group V atoms in a zinc blende structure so they have the same tetrahedral coordination as Si in the diamond cubic structure. The difference in electrons from the group III and group V elements average out to satisfy the 4 bonds per atom. As with Si, to donate extra electron a donor atom must have a



valence with one more electron than the atom it replaces, and to accept an electron the dopant must have one less. With group VI atoms on group V sites or group II atoms on group III sites this is fairly straight forward.

Group IV atoms like C, Si, and Ge in a III-V material are more complex because they can potentially occupy either site and act as a donor or an acceptor. As it turns out, the chemical potentials drive these dopants preferentially onto one site. For example C is p-type and Si is n-type in GaAs. Only at very high doping concentrations do they occupy a significant number of both sites. There is also the possibility of antisite defects in the intrinsic semiconductor, where a group III atom resides on a group V site or vice versa. These can be electrically active, but generally both of the extra or missing electrons end up as deep level states as they do for double donors in Si[12].

Hydrogen has an unusual behavior as a dopant. It diffuses readily into most semiconductors[13–15], but with only an s orbital to fill it is easily satisfied either giving or receiving one electron. Hydrogen does not substitutionally dope the semiconductor, but passivates dangling bonds or charged species that it encounters instead[16, 17]. Passivation includes neutralizing either donor or acceptor doping in most materials[18].

As a result of successful doping, when one of the carrier populations increases, there is some recombination of the new carriers with the intrinsic carriers of the opposite type. This reduces the number of carriers of the opposite type in the semiconductor. It turns out that the recombination yields a product between electrons and holes that is constant. If the electron concentration increases by an order of magnitude, the hole concentration decreases by an order of magnitude. The reference point is the intrinsic carrier concentration squared, yielding Equation 1-6.

$$n * p = n_i^2$$

1-6

Where  $n$  is the electron concentration,  $p$  is the hole concentration, and  $n_i$  is the intrinsic carrier concentration of electrons and holes.

The shift in electron and hole concentrations can also be viewed as a shift in the Fermi energy of the semiconductor. Because the intrinsic concentration of electrons and holes was equal in undoped material, the Fermi energy was at the middle of the band gap so that the electron populations defined by the Fermi Dirac function gave an equal number of electrons and holes. Once the material is doped, for example n-type, the Fermi level shifts upwards towards the conduction band to reflect the change in electron concentration. The Fermi Dirac function is inversely symmetric about the Fermi energy, so the only way to have a higher electron concentration is to raise the overall Fermi energy of the material. This also makes sense because there are now more electrons in the higher energy states, so the midpoint of 50% probability of electron occupation rises in energy. The reverse would be true of a p-type material.

As mentioned earlier, the mobility of the material is also affected by doping. The dopants used to increase the carrier concentration are ionized in the process of donating or accepting an electron, and will disrupt a carrier that is drifting past during conduction. This is why there is a mobility contribution from the ionized impurity scattering sites, and the mobility drops when a semiconductor is doped. However, the conductivity usually still increases, because of the low intrinsic carrier concentration. The carrier concentration can be increased by 10 orders of magnitude in some cases, while the mobility generally drops by less than 2 orders except in extreme cases of heavy doping where there is a large fraction of electrically inactive dopants.

## Transistor Operation

When an n-type and p-type semiconductor come in contact with one another, they are no longer in equilibrium because of the discontinuity in their fermi levels. The higher concentration of electrons in the n-type material will diffuse down the carrier gradient into the p-type material. Similarly, holes from the p-type material will diffuse into the n-type material. The electrons can then relax into the available states left by the holes. This is called recombination, since the electron and hole have recombined to a ground state configuration. In these depleted areas near the junction, the fermi level moves back towards the intrinsic level in the middle of the band. Representations of the semiconductor just before contact is shown in Figure 1-5a and the resulting Fermi level shift from depletion of carriers from diffusion is shown in Figure 1-5b.

However, as this diffusion occurs, the ionized impurities that served as the dopants leading to the excess electron and hole populations are fixed in the lattice and left behind. This separation of charges induces a voltage in the material around the p-n junction. A voltage, whether applied externally or present internally, results in a shift in the vacuum level. If a negative voltage is applied to a material with an external positive voltage, electrons would be drawn out of the material. This ease of separating electrons from the material is represented as a lowering of the vacuum level, since the electrons are easier to remove from the material. However, the Fermi level remains constant below the vacuum level because the population of electrons in the material is the same. When there is a difference in voltage across the material, the vacuum level and thus the bands of the material bend. Figure 1-5c demonstrates the band bending from the internal voltage. The slope induced by this voltage provides a counter force to the diffusion of carriers. This is called a drift current, because acceleration of carriers by a

voltage it is often slow relative to the random movements of carriers in a material, with an average current movement trending in the direction of the voltage.

It turns out that these two processes occur simultaneously and a new equilibrium is reached where the diffusion current and drift current perfectly counter each other out. The band bending is complimentary to the change in fermi level from the depletion of the semiconductor. The Fermi level ends up flat, and the bands and vacuum level end up bent to accommodate the fermi level as seen in Figure 1-5d. This leaves the free carriers in the n-type and p-type materials separated by a depletion region with fewer free carriers.

The device described above is called a diode because as an electronic device it behaves two different ways depending upon the direction an external voltage is applied. When a positive voltage is applied to the n-type side of the device and a negative voltage to the p-type side, the charges in the junction separate further. The electrons in the n-type region are attracted towards the positive applied voltage and the holes in the p-type region are attracted to the negative voltage. This draws them away from the junction and increases the width of the depletion region. As a result, the diode does not conduct unless the applied bias is strong enough to cause a breakdown of the material. This condition is called reverse bias because no current flows through the diode.

When a positive voltage is applied to the p-type material and negative to the n-type, the charge carriers in each side of the material are pushed closer together. The externally applied bias cancels out the internal bias of the depletion region and allows more carriers to recombine. As additional electrons are supplied to the n-type material and taken away from the p-type material supplying more holes, a current is allowed to

flow across the diode. When the bias allows a current to flow easily, the diode is considered to be forward biased.

A transistor is made up of three alternating doped semiconductor regions, either n-p-n or p-n-p. The style most used in logic devices like processors are Metal Oxide Semiconductor Field Effect Transistors, or MOSFETs. The two outside ends of the device are the source and drain through which the controlled current flows. The gate which rests above and isolated from the middle region controls the current between the source and drain. A schematic of a simple MOSFET device is shown in Figure 1-6. N-p-n devices are often shortened to NMOS and p-n-p to PMOS since they conduct through negative and positive charge carriers respectively.

Because of the orientation of the semiconductor, the junctions between the n-type and p-type regions act as two opposing diodes. When a voltage is applied between the source and drain, one of the two will always be reverse biased. This is usually labeled the drain because it is where current from the device leaves the logic gate to one of the power rails. Thus by default, the device is in the “off” state. Because there are still minority carriers in the channel and interface states along the surface of the device, there is still a small leakage current, but very little of these carriers make it across without recombining or being stopped at the field built up around the reverse biased junction at the drain.

When a voltage is applied to the gate, in this case positive for an NMOS device, the metal oxide semiconductor stack acts as a capacitor. A capacitor stores charge between two plates, the metal and semiconductor here, separated by the oxide as an insulator. As the electric field increases, charges build up on the plates on either side of

the insulator. In this case the positive voltage on the gate accumulates and draws minority negative carriers out of the bulk semiconductor towards the surface of the p-region. These recombine with holes near the surface and create a depletion region. You could also consider the holes to be repelled from the positive charge on the gate and driven deeper into the semiconductor, leaving a depletion region behind. As with the formation of the depletion region in a diode, the drift and diffusion currents equilibrate, but this time, the drift current from an applied voltage is the driving force.

Once the gate voltage reaches a point where only the ionized impurities remain at the semiconductor surface next to the oxide, the bands have then bent to the point where the surface is now as n-type as it initially was p-type. This point is called the threshold voltage because the surface of the semiconductor has now inverted to n-type and bridges the source and drain. Any higher voltage on the gate increase the free electron concentration in the inversion layer and ideally increases the source drain current by the square of the additional gate voltage shown in Equation 1-7.

$$I_D = \frac{W * \mu_n * C_{ox}}{2 * L} (V_{GS} - V_T)^2 \quad 1-7$$

Where  $W$  is the width of the transistor,  $\mu_n$  is the electron mobility, assuming an n-type device,  $C_{ox}$  is the oxide capacitance,  $L$  is the transistor length,  $V_{GS}$  is the gate voltage, and  $V_T$  is the threshold voltage. For digital logic, the transistors are operated as switches, either fully on or fully off, with a minimum of time spent switching. Because NMOS devices turn on with a positive voltage on the gate (attracting negative charge carriers to the channel) and PMOS turns on with a negative gate voltage (attracting positive charge carriers to the channel), logic gates can be built using PMOS to pull up the output and NMOS to pull down the output so that the transistors act in a

complimentary fashion and do not have any static power draw. This configuration is called Complimentary MOS or CMOS.

An inverter is the most basic CMOS logic gate. With a high voltage input, the PMOS transistor is off and the NMOS transistor is on thus connecting the output to ground. With a low voltage input, the PMOS transistor is on and the NMOS transistor is off, connecting the output to the power rail. Assuming there is no leakage through the gates, there is no power drawn from the input, and since the outputs would connect to another gate there would be no static power drawn from the output. When switching some power is wasted while both gates are partially on, so fast switching is desired. Once the output has changed states, just enough power is drawn to change the voltage on the gates of subsequent logic. Ideally there is no leakage through the transistor that is turned off, but in modern devices this is unfortunately not the case.

### **Power Dissipation Challenges**

Power dissipation in logic devices comes primarily from two sources. The consumption used to charge and discharge the gates of subsequent transistors and the leakage from transistors in the off state. The dynamic power consumption is necessary to operate the devices, but static losses are of great importance because they dissipate power which is not necessary to the circuit's operation. Power dissipation is now the biggest limitations to increasing the complexity and speed of integrated circuits, so having static power waste takes away from the power that could be used for computing[5, 8]. Power consumption is why the  $I_{on}/I_{off}$  ratio is critical, as high on currents are necessary for high switching speeds, while low leakage is critical for power reduction.

When device shrinking occurs, the source, drain, channel and gate all get smaller. This results in reduced resistances from the reduction in length through which the current must travel in the transistor. It also reduces the capacitance in the gate via a reduction in area. The combination of higher drive current and lower load means that faster switching speeds are possible. However, once the transistor becomes too small, short channel effects become an issue. The gate length in current devices is limited by the ability of transistors to turn off requiring a sufficiently long channel. Otherwise charge carriers would simply tunnel across the channel. Specifically, Drain Induced Barrier Lowering (DIBL), in which the space charge region from the drain side of the transistor lowers the channel barrier that isolates the source and drain, which lowers the threshold voltage and brings the channel closer to inversion. Leakage increases and both power dissipation and switching speed are reduced. These have been mitigated by switching to Fin shaped MOSFETs, called FinFETs.

FinFETs reduced leakage currents and DIBL by isolating the channel region from the bulk semiconductor allowing the gate to better control the inversion layer in the channel. Better gate control allows shorter channels that improve  $I_{on}$  without DIBL increasing  $I_{off}$ . However, as FinFETs shrink, their ability to control the channel will diminish as well. Gate All Around (GAA) nanowires will provide a next step of improvement and further the shrinking of Si transistors, but the continued transistor improvements may necessitate the use of new materials and transistor designs.

### **Benefits of III-Vs Over Si**

In a short channel device,  $<50\text{nm}$  for Si, the source-drain voltage across the channel is sufficient that once turned on, most carriers cross the channel without experiencing a scattering event[19]. Because of this, carriers are freely accelerating



across the channel of the turned on transistor. Their transport time is then no longer dependent upon the channel mobility, but rather the injection velocity at the source-channel interface[20]. This injection velocity is still dependent upon the material mobility. Therefore the III-V materials with higher mobilities would be able to achieve higher  $I_{on}$  for similar channel lengths with acceptable  $I_{off}$  leakage[21]. Although a lot of work has been done on GaAs, the ternary alloy  $In_xGa_{1-x}As$  (often shortened as InGaAs) has an even higher mobility and a larger, more useable band gap than InAs[22, 23].  $In_{.53}Ga_{.47}As$  is a common choice because it is lattice matched to InP making growth of the InGaAs easier. Materials such as InGaAs are preferable for future devices because they could still be manufactured into the same structures as Si, with the improved  $I_{on}$  currents needed to reduce power and enable faster electronics.

Since InGaAs is also a direct band gap material, it is possible to manufacture Tunnel Field Effect Transistors (TFET). TFETs operate through tunneling rather than barrier lowering like MOSFETs, so they switch on and off much faster, as measured in mV/decade, or the gate voltage change necessary to increase the output current by an order of magnitude[24]. As a result of better switching, they have lower leakage currents, higher drive currents, and require lower voltages to run, all which reduce power consumption[25, 26].

### **Challenges to III-V Integration**

However, with these high performance devices whether MOSFETs or TFETs, the contact resistances to the source and drain can become a significant portion of the device resistance, limiting the drive current and on/off ratio of the device[27]. Although the channel may still modulate its resistance by 6 orders of magnitude, the contact

resistance may limit the on state current to such a degree that the effective current modulation is barely discernable and  $I_{on}/I_{off}$  is significantly reduced. III-V materials can meet the specifications for device channels down to the 1nm node predicted for 2027, but the International Technology Roadmap for Semiconductors (ITRS) has predicted that contact resistivities less than  $1 \times 10^{-8} \Omega \text{cm}^2$  are necessary for future devices[28].

The formation of low resistance Ohmic contacts in a classical case relies on choosing a contact metal with a work function that falls slightly below the conduction band edge of the semiconductor for an NMOS device[29]. This way there would be available electrons and states in the metal near the conduction band edge and a low barrier for electrons to move between the materials. Yet in many III-V materials, InGaAs included, metal contacts are pinned to a different energy, even when the metal work function on its own would suggest otherwise.

With a Schottky barrier at both the source and drain as a result of the fermi level pinning, there are now two more opposed rectifying junctions. Unlike the transistor, these are not modulated and one of the two will always act as a barrier to current flow. A Schottky barrier induces a depletion region in the semiconductor, but with high levels of doping, the depletion region and thus the barrier may be thin enough for electrons to tunnel through it. Contact resistance can be lowered by increasing the doping in the semiconductor just below the metal contact, increasing the number of carriers near the metal-semiconductor interface[30]. Because the contact pinning in InGaAs is so high, and the variation between metals is minimal, the reduction in contact resistance has to come from a thinning of the contact barrier rather than a lowering of the barrier. Based

on barrier height approximations by Baraskar et al. [31], carrier concentrations greater than  $6 \times 10^{19} \text{ cm}^{-3}$  are needed to achieve sufficiently low contact resistivities on InGaAs.

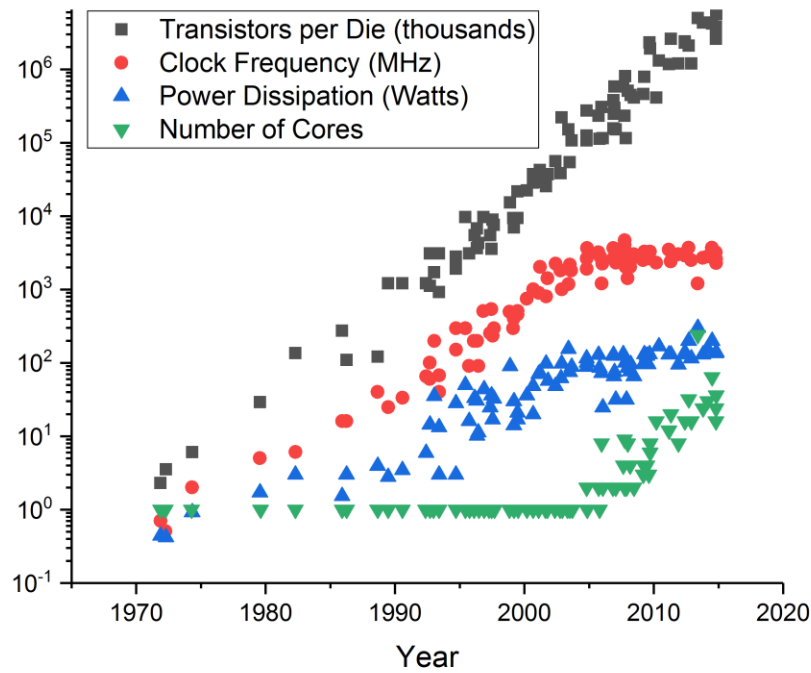


Figure 1-1. Trend showing the continuation of Moore's law into modern devices, even when pushing against fundamental limits like the ability to dissipate excess heat. Replotted data from [32].

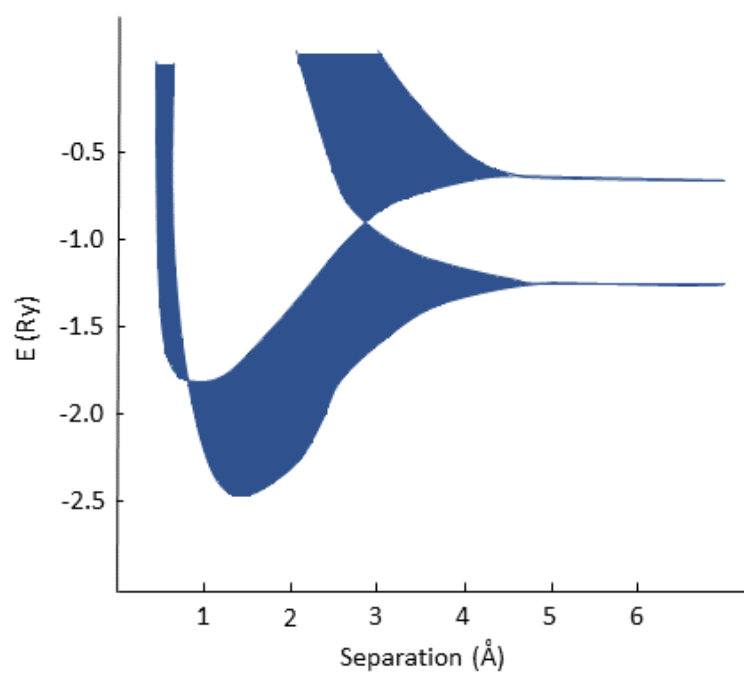


Figure 1-2. Plot of allowed electron energy levels vs atomic spacing showing the formation of bands in carbon. Replotted data from [33].

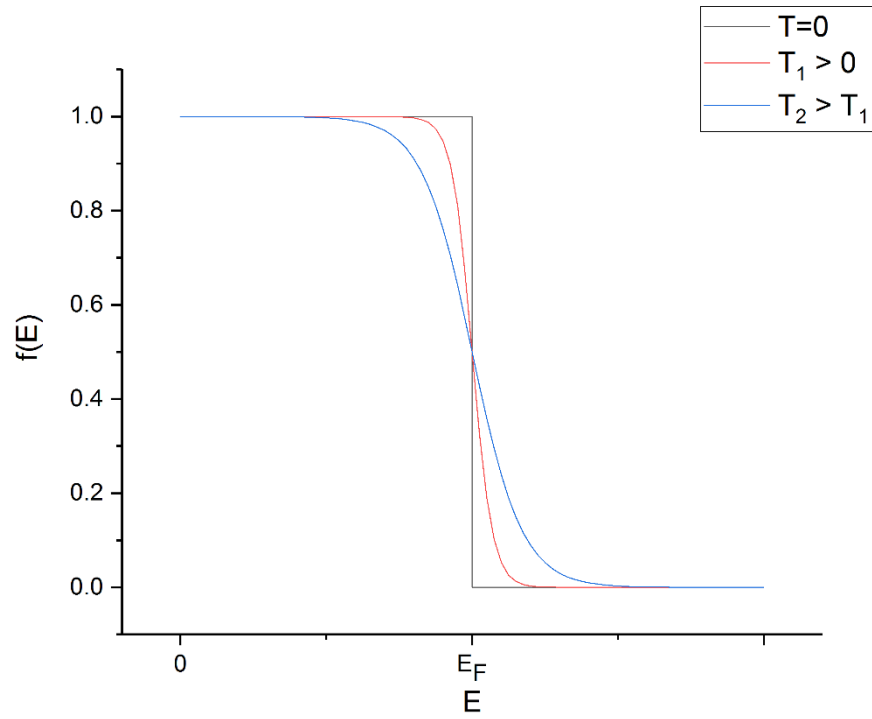


Figure 1-3. The Fermi-Dirac function showing the temperature trends of the probability of an electron energy state being occupied at different temperatures.

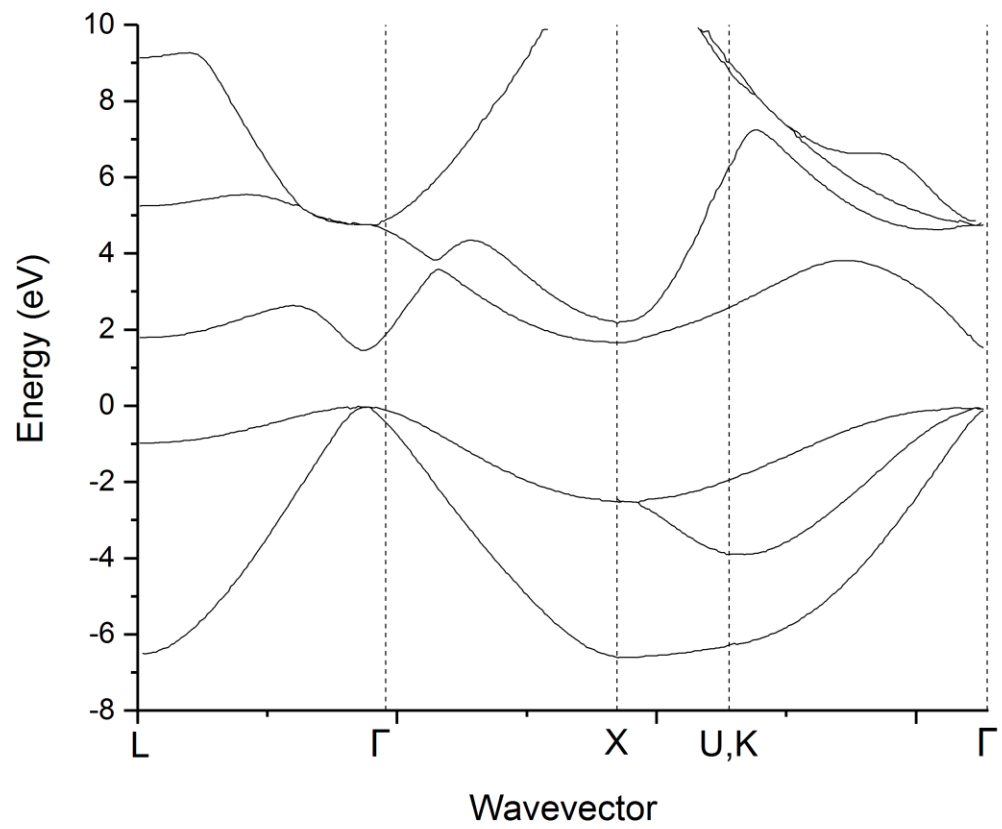


Figure 1-4. E vs. k diagram showing the band structure for GaAs. Replotted with data from [34].

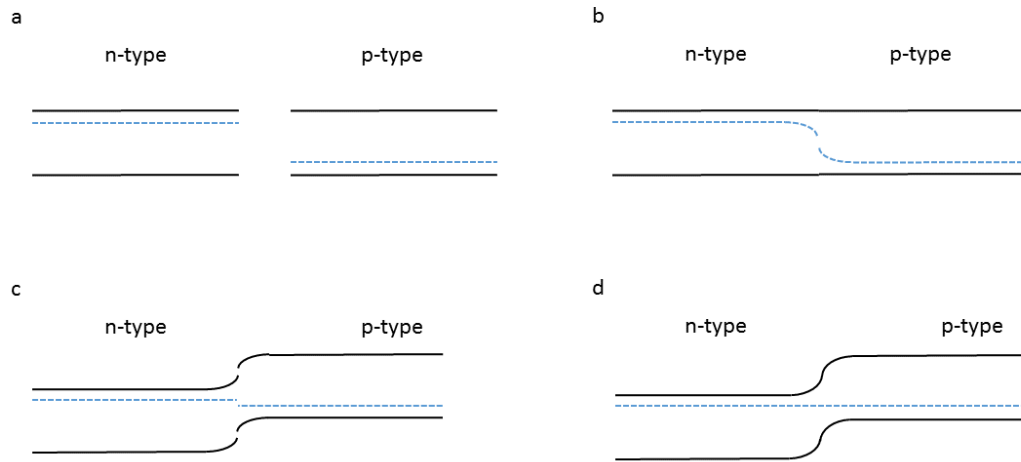


Figure 1-5. Semiconductor depletion and band bending at pn junction formation. A) P-type and n-type semiconductors prior to contact. B) Recombination of carriers upon contact, creating depletion regions. C) Band bending as a result of carrier depletion. D) Pn junction in equilibrium

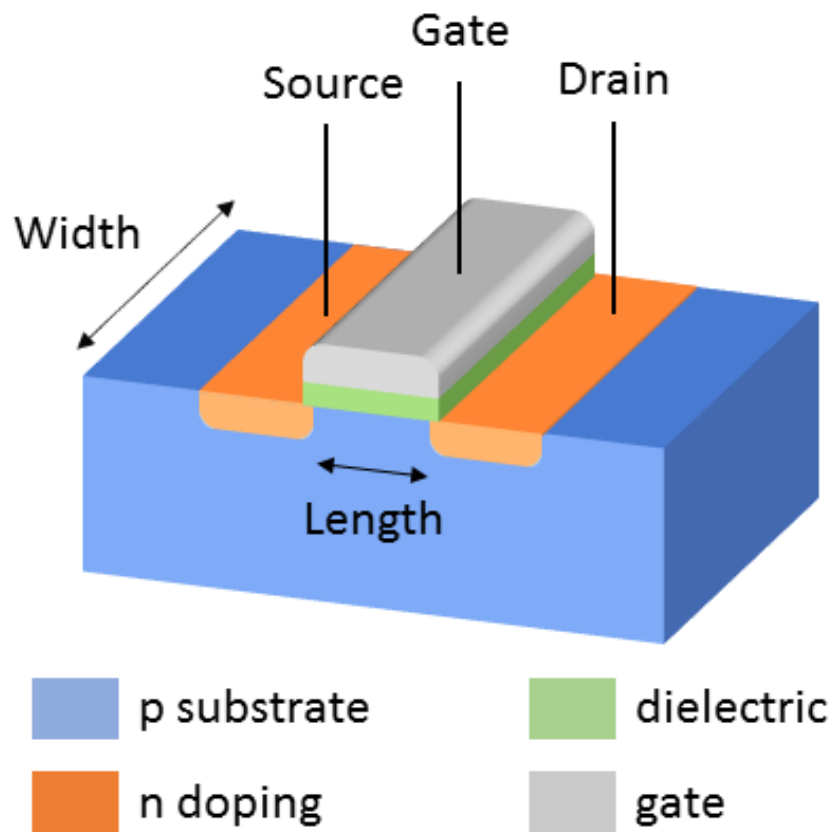


Figure 1-6. A basic planar NMOS transistor.



## CHAPTER 2

### DOPANT STABILITY AND INCORPORATION METHODS

Achieving the high doping levels necessary for low contact resistivity in future devices is not trivial. Many of the techniques that are used for doping cannot achieve the doping levels needed for contact resistivities less than  $1 \times 10^{-8} \Omega\text{cm}$ . Many of them are limited by the thermodynamic equilibrium of active dopant solubilities in the semiconductors, although methods to circumvent these limitations exist.

#### **Dopant Saturation**

Dopants can be limited in activation through a number of mechanisms. One reason could be a high ionization energy. This can be solved in most cases by choosing another dopant, so it is mostly a problem for wide band gap semiconductors[35]. Although compensating doping would generally recombine carriers and reduce the carrier concentration, in this case co-doping to partially compensate the high ionization energy dopant can draw the electrons or holes away from the dopant to get them to ionize more readily[36–38]. However in InGaAs with shallow dopants already available, counter doping the material offers no benefits[39].

The next doping limitation is the precipitation of an insoluble second phase above a certain concentration[12]. For example, the precipitation of boron in silicon is well documented to form a metastable  $\text{SiB}_3$  phase above  $10^{19}$ - $10^{20} \text{ cm}^{-3}$  concentrations depending upon the temperature[40–42]. Precipitation is easily observed in X-Ray Diffraction (XRD) and Transmission Electron Microscopy (TEM). Phase diagrams with the solubility of most dopants and semiconductor systems is readily available and predicts the equilibrium concentration of dopants before precipitation occurs. However, there are many dopants which will electrically saturate before they reach their physical

solubility limit[43–46]. This means that above a certain point, more dopants can be added without precipitating, but at equilibrium the additional dopants no longer add to the carrier concentration.

As doping levels change, point defects that intrinsically exist within the semiconductor, like vacancies and antisite defects, can act to stabilize carrier concentrations as well. The first mechanism is by taking on different charges[47, 48]. The shift in intrinsic defect charge state is a response to the changing potential within the material. As the fermi level changes, a defect like a vacancy with dangling bonds may become more likely to donate or accept an electron. Similar to the Le Chatelier principle in chemistry, the charge taken on by the defect acts to counter the fermi level change of the doped semiconductor. Through a similar mechanism, the equilibrium population of intrinsic defects can also change as the doping level increases[49]. A third possibility is the formation of defect clusters involving a dopant atom and the intrinsic point defect, similar to hydrogen passivation.

Point defect concentrations and clusters are still difficult to detect because they are too small to observe directly. Because they are not large enough to create a second phase with a drastically different composition like a precipitate, their existence must be inferred and cross checked with multiple indirect methods.

Photoluminescence[45, 50–52] and similar techniques[53] were able to identify the existence and energies of mid gap states, but the species involved could only be inferred. As a result, these levels were referred to as AX and DX centers, since the acceptor or donor atom was interacting with an unknown point defect. By changing dopants and stoichiometry to try to affect the intrinsic point defect populations, even

early works suspected a gallium vacancy was responsible for donor deactivation in GaAs[45, 54]. Intentional radiation damage was also used to generate greater concentrations of vacancies, although this was not limited to identify one specific type of vacancy[47, 55].

With the addition of additional techniques such as positron annihilation[56, 57], X-ray Absorption Fine Structure (XAFS)[58–60], and ab initio modelling[59, 61, 62] more direct observations of vacancy type and bonding environment can be measured and simulated. In GaAs it is now generally believed that Ga vacancies are responsible for deactivating n-type doping.

Amphoteric compensation is possible in materials like GaAs when extreme measures are taken to force amphoteric dopants like Si and Ge onto the As site, but as discussed in the doping section, these two dopants prefer to reside on the Ga site[43]. Point defect mechanisms seem to limit the activation of group IV dopants before site selection becomes an issue[39, 63–65].

### **Achieving Supersaturation**

In order to achieve higher doping levels than these deactivation mechanisms want to allow, we need to either shift the thermodynamic equilibrium or find a kinetic limitation that prevents deactivation. Although it is not an issue for the materials and dopants studied in this work, the shift in ionization energy for counter-doped deep level dopants is a good example of a shift in equilibrium. As a result it will remain stable even with subsequent processing.

The thermodynamic drivers of precipitation are not so easily modulated. However, the solid solubility of dopants generally increases with temperature and

sometimes dopants can be quenched in place. By introducing the dopant or annealing at a high temperature with greater solubility and quickly cooling the material to a temperature where the dopants are frozen in place, the dopants are stuck in a solid solution without sufficient energy to diffuse together into precipitates.

Contrary to the case with solid solubility, point defects and vacancies exist in greater numbers at higher temperature. The additional thermal motion and energy of the atoms leads to a higher population that are off of lattice sites at any given time. Quenching from high temperatures locks in these vacancies leaving more defects and more potential deactivating sites than would otherwise be present[66, 67]. To prevent the formation of intrinsic point defects, it is best to use dopant incorporation methods that work at low temperature where energy barrier to defect formation limits the kinetics of deactivation[35, 68]. The following doping methods discussed are evaluated on their ability and mechanisms for achieving high doping levels.

### **Returning Supersaturated Doping to Equilibrium**

In a material that is doped to a supersaturated level using kinetic limited methods, subsequent processing can bring the material back to equilibrium. Since the primary deactivation mechanism in GaAs and InGaAs is point defect mediated, the formation and diffusion of point defects is what deactivates the supersaturated doping.

The most common form of energy given to doped samples is heat treatment. Subsequent processing during microchip fabrication, including depositions and diffusion steps almost all involve heating the material. When a sample is heated, the average motion of the atoms in the material increases. Like with the excitation of carriers in a semiconductor, the energy of any one atom falls along a distribution, so some atoms will

have higher energies than others. When the energy of an atom exceeds the bond energy with neighboring atoms, this is when point defects are generated and diffusion can occur. Because of the distribution of thermal energies, a given process or mechanism will have an activation energy and rate that follows the Arrhenius relationship shown in Equation 2-1[69].

$$k = A * e^{\left(\frac{E_A}{R*T}\right)} \quad 2-1$$

Where k is the rate constant for diffusion or a reaction at a given temperature, A is a pre-exponential factor that scales the rate constant,  $E_A$  is the activation energy for the process, R is the ideal gas constant, and T is the temperature in Kelvin. With the added energy for atomic motion, this is when diffusion of supersaturated dopants that were quenched into a high concentration will start to precipitate[40, 70–72]. They were at a non-equilibrium condition in the quenched state, but without the thermal energy, they could not move to reach equilibrium. Similarly, point defects are able to form and move at elevated temperatures to cause deactivation as well[73–76]. As you would expect this equilibrium state is dependent upon the material properties and not the incorporation method and thus deactivation proceeds to the same levels[77].

Irradiation can also impart a significant amount of energy into a semiconductor by displacing atoms with impact. This may be induced by either dopants being incorporated in a method like ion implantation or by inactive species. Although not as much diffusion in the traditional sense occurs, atoms are displaced with a bias towards the direction of the radiation. Although some dopant atoms will be displaced, the greatest effect of radiation damage is by far the formation of intrinsic defects[55, 78–80]. Because the formation of point defects is more indiscriminate compared to the intrinsic

formation of defects within a non-equilibrium semiconductor, deactivation can be complete rather than settling to an equilibrium activation value[47, 81].

### **Growth From a Melt**

Czochralski growth is probably the best known semiconductor growth method and is used to create most substrates. The solidification of metal single crystals was discovered by Jan Czochralski in 1918[82], then improved upon for semiconductor use by Teal and Little at Bell Labs[83]. In the Czochralski process, a single crystal seed is dipped into a melt of the semiconductor and then slowly pulled from the melt at a rate less than the solidification velocity. The rate depends upon the undercooling of the seed crystal, but at low enough rates, the growing crystal will have time to template perfectly to the seed crystal's orientation. Rotation of the crystal and melt ensures uniformity. Dopants are added by necessity, since it is thermodynamically impossible to purify a perfect material. This doping is usually done to a low concentration such that subsequent processing can dominate the properties of the material.

These dopant elements are never perfectly matched to the solidification of the semiconductor and typically prefer to remain in the liquid solution rather than the solid solution. This results in an enhanced concentration down the length of the growing single crystal boule. Segregation coefficients can vary widely from percentages near unity down to thousandths of the concentration present in the liquid being incorporated into the solid[84]. For the growth of III-V semiconductors, the need for stoichiometry in the crystal as it grows keeps the group III and group V elements from appreciably segregating, but differences in vapor pressures above the melt can result in the loss of one component, often As or P in the arsenides and phosphides.

To overcome evaporative losses, these materials are often solidified under conditions that prevent the evaporation of these elements into the atmosphere. This could mean crystallization in a sealed tube in the Bridgman[85] or Stockbarger[86] growth methods, or an encapsulated Czochralski growth method[87, 88]. These allow for the growth of binary III-V materials, but still not ternary ones like InGaAs because the isovalent elements are then subject to the segregation coefficients and will vary across the boule.

For these compositions it is easier to grow thin films using a solution growth technique like Liquid Phase Epitaxy (LPE). Here, the semiconductor is dissolved in a lower melting temperature material like Bi or Ga[89]. This allows it to remain a liquid at a temperature well below the melting point of the semiconductor. A substrate wafer can then be submerged in the solution and the semiconductor will solidify onto the substrate wafer. Controlling the composition of the melt can compensate for any segregation coefficients and growing only thin films prevents variation within the layer.

What prevents these methods from achieving high carrier concentrations is that all of these techniques are thermodynamically limited to an equilibrium state. The growth occurs slowly and near the melting temperature of the semiconductor, meaning that there is sufficient time and energy for any compensating mechanisms to take over in instances of heavy doping concentrations. This limits the doping concentrations of most dopants and semiconductor materials to levels that are insufficient for modern technology.

## **Ion Implantation**

Ion implantation is an improvement on solid source diffusion because it allows for control of the dopant incorporation depth and concentration to a degree that is not otherwise possible. The tool operates under vacuum, but the accelerator and sample chamber can be isolated for loading and unloading and differentially pumped to increase the pressure that can be left in the sample chamber. A source of the dopant to be implanted is heated and ionized with a high strength electric field creating a beam of ionized atoms.

This beam is bent through a magnetic mass separator so that only the dopant atoms and typically only one isotope of the dopant will reach the substrate. Any other ions pulled out of the source material will hit a beam stop somewhere else in the chamber. This magnet also directs the beam towards the sample chamber. The resulting beam of atoms is accelerated to a fixed energy that will determine the depth that the dopant penetrates the substrate. Energies can range from 100s of eV to MeV and may leave dopants in the top few nanometers of the substrate to several microns deep. There is obviously a wider distribution in deeper implants as well. Since the substrate is also a single crystal, it is mounted at an angle that prevents channeling of some ions, resulting in a depth profile with a single dopant peak. A set of raster coils will scan the beam across the sample. Because all of the ions hitting the substrate are ionized, a current integrator between the sample and ground can measure the accumulated dose of ions that are incident on the sample. This sounds like a good doping method because any concentration of dopants can be forced into the semiconductor, even well above the equilibrium concentration.



Introducing the dopants as energetic ions does have its drawbacks. They create a significant amount of damage to the crystal lattice of the semiconductor. There is a dependence upon the substrate mass, dopant mass, and implant energy on how the ion is stopped in the material, but generally light ions and high energies will experience more electronic stopping and heavier ions or low energies (including ions that have travelled deeper in the sample and lost energy) experience more nuclear stopping. Nuclear stopping with direct collisions between atomic nuclei creates more damage than electronic stopping, and doping for contact regions would need high doses and low energies to keep the dopants near the surface. With heavily damaged material, it would not behave well as a semiconductor because of the disorder and loss of coordinated bonding in the material. To repair this damage, thermal annealing is necessary.

Annealing allows the semiconductor to diffuse and repair the damage caused by the implant step. Most semiconductor and dopant atoms diffuse back onto lattice sites. Because the implanted dose now exists as excess atoms present in the crystal, it is possible for high concentration implants to generate extrinsic loops. These will not be exclusively the dopant atoms, since the substrate elements were also displaced off of lattice sites.

The majority of dopants are able to get onto lattice sites and active, but again the activation is limited by the thermodynamics at the anneal temperature. The high number of defects after implantation potentially eases the formation of compensating defects at high doping concentrations. With extreme levels of damage, such as extremely high dose implants or implants done at cryogenic temperatures where dynamic damage recovery is unable to occur, the semiconductor can be made

completely amorphous. For some materials like silicon, this can be advantageous. Once amorphized, silicon will regrow through Solid Phase Epitaxial Growth (SPEG) templating to the underlying single crystal material very rapidly at a temperature much below its typical melting temperature[90]. This regrowth puts all of the atoms in the material onto lattice sites and can achieve supersaturated doping above the equilibrium concentration[72, 91, 92].

Unfortunately in III-V materials, SPEG is not as clean as it is in elemental semiconductors[93, 94]. The group III and group V elements need to get onto the proper sublattices, yet SPEG occurs fast enough that there is insufficient time for this redistribution. The speed of SPEG results in a heavily defective regrown layer with a large number of twin boundaries and stacking faults[93, 95]. These excess defects reduce the dopant activation even when compared to implants of the same dose at higher temperatures[96–99]. Planar defects have a detrimental effect on the mobilities of the material in addition to the lower activation.

Electrical activation of implanted species is limited to an equilibrium value at the temperature of the activating anneal and is lower in concentration than is useful for desired contact resistivities[100–102]. Other growth methods can achieve the desired doping concentrations without the limitations or issues of ion implantation.

### **Molecular Beam Epitaxy**

Molecular Beam Epitaxy (MBE) is the growth method that gets the highest electrically active doping concentrations. MBE condenses a beam of evaporated elements onto a substrate under high vacuum. High purity samples of the elements needed for the semiconductor and dopant being used are heated. A baffled holder

called a Knudsen effusion cell generates an equilibrium pressure of evaporated atoms. These are allowed to escape through a small orifice which makes the flux of evaporated atoms coming off of the source more uniform and collimated[103]. The growth rate and composition can be controlled by adjusting the temperatures of the different sources and thus the flux of atoms leaving the cell. The adsorption and desorption of atoms from the surface determines the growth rate. The beam equivalent pressures, or flux of atoms, for each element can be adjusted to the proper ratio by experimentally compensating for the sticking coefficients of the atoms on the substrate. It is thus easy to incorporate almost any concentration of dopants into the growing material.

However the atoms incident on the substrate still need to form into a crystal structure if they are going to become functional semiconductor materials. With a single crystal substrate of the same material or similar in lattice constant to the material being deposited, the growing material will template to the substrate fairly readily. This is because of a relatively high surface mobility of the adsorbed atoms on the surface[104]. The substrate may be heated to facilitate the motion of atoms on the surface, but rarely more than a few hundred degrees Celsius.

The energetics of atoms on the surface determines the morphology of the growth. Depending upon the “wetting” properties of the free atoms at the surface, they can evolve into several morphologies. If the adsorbed atoms of the material being grown prefer to agglomerate, it will form islands as part of the Volmer-Weber growth mechanism. Under other conditions where the material being grown prefers to template to the substrate, the growth will start layer by layer and can either continue growing layer by layer as Frank-van der Merwe growth or transition to island, Stranski-Krastanov

growth. Frank-van der Merwe growth is sometimes called layer by layer growth because the lowest energy position for an adatom on the surface is a step edge. With sufficient surface mobility, adsorbed atoms will preferentially finish a monolayer of growth before starting another layer. The transition in Stranski-Krastanov growth is the result of a changing surface energy that can come from relaxation in a strained layer or a change in surface energy where adatoms that prefer to grow layer by layer on an initial heteroepitaxial substrate prefer to agglomerate during homoepitaxy.

The growth mode is also mediated by the Ehrlich-Schwoebel barrier. Atoms that adsorb below a step edge on a growing surface tend to stay on the lower step[105]. Similar to how an adatoms come to rest at step edges because the higher coordination puts them into a lower energy state, an adatom trying to climb the step would have to pass over a region where it has lower coordination than it does elsewhere on the surface[106, 107]. Through this mechanism, the growth mode during MBE can be controlled to a certain extent. By growing at lower substrate temperatures, adatoms have less surface mobility and cannot climb step edges as easily. This promotes Frank-van der Merwe growth over Stranski-Krastanov or Vollmer-Weber growth[108]. The use of surface segregating atoms during the growth can also alter the surface energies of the system and force the growing material into layer by layer growth without significantly incorporating into the final product[109].

Doping during growth by MBE is only a matter of incorporating the dopant atoms in the flux of atoms incident on the surface. As with the need for growth, doping requires more dopant atoms incident and adsorbed on surface than desorbing[110]. Lower temperatures both increase the sticking coefficients of the dopants and reduce

the energy for defect formation[111]. Adsorbed dopant atoms prefer to maintain high coordination on the surface just like other adsorbates and can be forced onto lattice sites once they are grown over. However, some dopants act as surfactants and prefer to segregate to surface rather than incorporate into the bulk material. These dopants may have to build up a surface concentration before reaching their peak incorporation rate into the bulk[112, 113].

Silicon is a common dopant in InGaAs, and layers with sufficient carrier concentrations have been grown by MBE to achieve low contact resistances[31, 114–119]. However, because of the high vacuum needed, loading and changing substrates is slow, and replacing sources when they are depleted may take over a week for the tool to pump down and become operational. This down time is impractical for industrial use due to the need for high throughput equipment.

### **Metal Organic Chemical Vapor Deposition**

Metal Organic Chemical Vapor Deposition (MOCVD), also known as Organo-Metallic Chemical Vapor Deposition is another growth method that has found widespread use in industry. MOCVD consists of a growth chamber with a heated and rotated susceptor for the substrate to sit on, a vacuum pump for low pressure MOCVD, and a showerhead to introduce precursor gasses uniformly over the substrate surface. MOCVD operates by introducing organometallic precursors where the “metal” is the element to be deposited. The organic molecules attached help keep the atom of interest in the gaseous phase on its way to the substrate. These compounds are often a solid or liquid at room temperature. They are maintained at a constant temperature to have a specific vapor pressure so that the flux of precursors can be closely controlled.

A carrier gas like hydrogen is used to bring in several organometallic precursors at once to the MOCVD chamber. The substrate is heated so that the organic molecule decomposes on the surface, usually being reduced with the surrounding hydrogen or reacting with parts of the precursor from the other organometallics present. This leaves the metal atom on the surface.

The temperature of the chamber and incoming gasses must be controlled to prevent either condensation of the reactants in the source lines or gas phase reactions which are detrimental to growth quality[120]. Depending upon the substrate temperature, growth can occur in several regimes[121]. At low temperatures, deposition is entirely dependent upon the reaction of the precursors at the surface. Some precursors may not break down at all and the deposition is relatively uncontrolled. At intermediate temperatures, the decomposition reactions all happen readily at the substrate surface and the growth is transport limited by the concentrations of reactant gasses introduced in the system. In the transport limited regime, the fluxes of the precursors determine the stoichiometry of the growth similar to MBE. Almost all MOCVD occurs within the transport limited regime. At temperatures that are too high, the precursors may react prematurely in the boundary layer gas phase above the substrate, resulting in the deposition of particles rather than a smooth film[122, 123].

Reducing the pressure during the growth can allow for wider temperature ranges while still maintaining control of the growth with the partial pressures of the reactants[22]. Lower temperatures can be used because of the ease of pyrolysis under reduced pressure, and higher temperatures because the lower number of gas-gas molecule interactions reduces the risk of premature reactions. For these reasons

almost all modern MOCVD is performed at reduced pressures. Even at reduced pressures, MOCVD is not as low as the high vacuum of MBE. This means that substrates can be swapped out more quickly and chamber maintenance does not require long shutdowns of the tool. Furthermore, replacement of precursors does not require venting and reconditioning of the chamber, since the precursors are sourced remotely.

Maintaining stoichiometry during growth of III-V materials relies on the low sticking coefficient of group V atoms to a group V terminated surface. Using an overpressure of the group V precursor prevents off stoichiometric growth and a large number of anti-site defects from forming[124]. Even under transport limited conditions, group V atoms that react on the surface will eventually desorb if they cannot find adjacent group III atoms to bond with. For this reason, the ratio of the group V flux to the group III flux, or V/III ratio is usually in the tens to hundreds. The excess of group V atoms also means that the growth rate is dependent only on the group III flux in a transport limited regime[125]. As a result, mixing group III elements in ternary compounds like InGaAs is relatively straightforward compared to mixing group V elements[126].

As with MBE, there is significant motion of surface atoms once they have adsorbed and the remaining organics have pyrolyzed. This leads to the same Vollmer-Weber, Stranski-Krastanov, and Frank-van der Merwe growth modes as experienced in MBE. There are also remaining organic molecules and hydrogen that adsorb on the surface and there is usually some carbon and hydrogen incorporated during MOCVD growth as a result.

Doping by MOCVD involves introducing a precursor carrying the dopant in addition to the precursors used for growing the semiconductor. However the pyrolysis reactions are affected by the introduction of dopants and may react more or less readily depending upon the species[121, 127, 128]. Some dopants may pyrolyze more readily than others, even for the same dopant. For example, silane does not decompose well at low temperatures, so disilane may be preferred to get silicon doping under low temperature conditions[129, 130]. High fluxes of dopants may be used to compensate for poor reaction kinetics, but this is expensive because of the inefficient use of high purity precursors.

Another similarity with MBE is that low temperatures are desired to limit the formation of compensating point defects. Because of the need to dissociate the organic molecules in order to get deposition, even under low pressure operation, growth by MOCVD must take place at a higher temperature than MBE. This brings MOCVD closer to an equilibrium process than MBE, meaning that the non-equilibrium, supersaturated doping concentrations possible with MBE are not typically possible with MOCVD[31, 131, 132]. It is easily possible that increasing the incorporation of dopants in MOCVD at high concentrations will result in increasing compensating defects with stagnant electrical activation[133].

### **Opportunity for Study of Te**

A recent result studying Tellurium doping in InGaAs grown by MOCVD was found to have a high carrier concentration of  $8 \times 10^{19} \text{ cm}^{-3}$  compatible with contact region doping for future technology nodes[131]. Doping by MOCVD is promising for widespread industry adoption, but the lower equilibrium doping levels of Te from



methods like ion implantation call in to question the stability of this highly active doping[134, 135].

A preliminary set of anneals on the material from Orzali et al.[131] were performed to determine if this high electrical activation was stable. Figure 2-1 shows the preliminary electron concentrations for samples as received and annealed at increasing temperatures for 10 minutes. These Hall Effect measurements show a starting electron concentration of  $6 \times 10^{19} \text{ cm}^{-3}$  rather than the  $8 \times 10^{19} \text{ cm}^{-3}$  reported, but more importantly with increasing temperature anneals, the electron concentration drops to  $7 \times 10^{18} \text{ cm}^{-3}$ . This deactivation of the electron concentration by almost an order of magnitude confirmed that the grown in Te was supersaturated and warranted further study of Te behavior in InGaAs, since its promise as a potential contact region dopant in III-V transistors would be dependent upon its stability through subsequent processing. The following work seeks to understand Te doping in InGaAs by studying the deactivation of supersaturated Te.

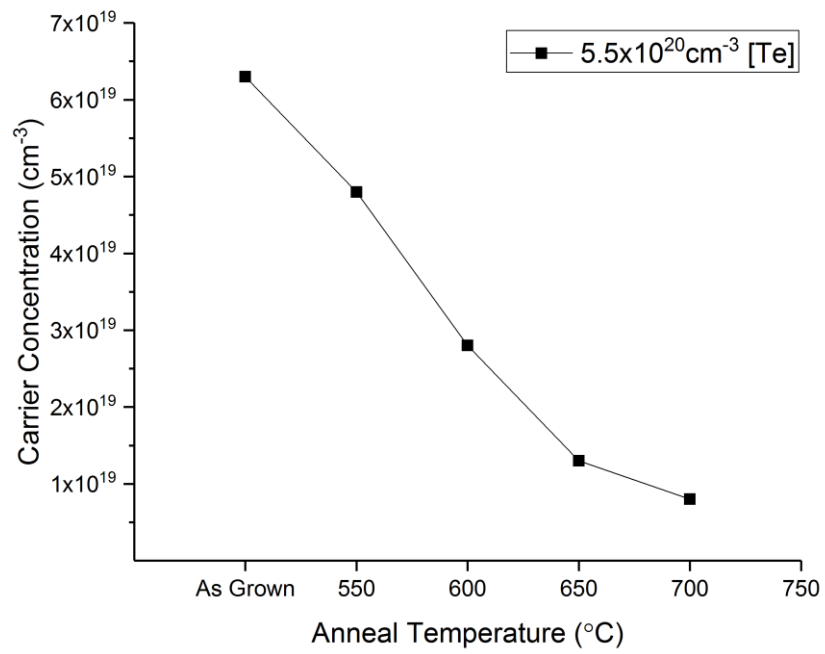


Figure 2-1. Deactivation of heavily Te doped InGaAs after 10 minute anneals at varying temperature.

## CHAPTER 3 ANALYSIS TECHNIQUES

### Hall Effect

Hall Effect is a method of measuring the resistivity, carrier type, and density of a thin film sample. It relies on the principle of the Lorentz force, or “right hand rule” that describes the forces on a charged particle moving through a magnetic field[136]. A fixed current applied across the face of a thin sample, and a known magnetic field applied through the faces of the sample, the charge carriers in the material will feel a force perpendicular to the magnetic field and their direction of travel, or along the other axis of the sample. This force creates a measurable voltage along that remaining axis of the sample[137]. By following the contact placement guidelines and equations derived by van der Pauw, the resistivity, majority carrier type, carrier concentration, and carrier mobility can be determined[138].

For a square sample with contacts labeled 1-4 sequentially at each of the corners, the sheet resistance can be measured as follows[139]. A small DC current is applied across two adjacent contacts e.g. 1 to 2. The voltage is measured between contacts 4 and 3, going in the same direction as the current, but from the other side of the sample. A characteristic resistance for this measurement  $R_{12,43}$  is calculated by Ohm’s Law in Equation 3-1.

$$R_{12,43} = \frac{V_{43}}{I_{12}} \quad 3-1$$

$R_{12,43}$  is the resistance measurement in this orientation,  $V_{43}$  is the voltage across probes 4 (positive) and 3 (negative), and  $I_{12}$  is the current applied going from probe 1 to 2. This measurement is repeated in the reverse direction and in the other 6

orientations, essentially rotating the sample 90° and repeating these two measurements three more times. The 4 measurements along each axis should all match within a few percent, otherwise this is indicative of an irregularity of the sample or non-Ohmic contact. These can be averaged together into two resistances  $R_A$  and  $R_B$ . The sheet resistance  $R_S$  can be calculated by taking those two resistances and solving Equation 3-2 for  $R_S$ .

$$e^{(-\pi^* R_A / R_S)} + e^{(-\pi^* R_B / R_S)} = 1 \quad 3-2$$

A magnetic field is then applied through the sample and Hall measurements are taken. This involves applying a current diagonally across the sample (e.g. 1 to 3) and measuring the voltage on the perpendicular contacts 2 and 4. With a positive field (in this case  $I_{13} \times B = V_{24}$ ) the voltage measurement can be denoted  $V_{24P}$ . The reversed current from contact 3 to 1 will yield  $V_{42P}$ . The measurements with the reversed magnetic field are  $V_{24N}$  and  $V_{42N}$ . Like with the resistance measurements, these 4 measurements are then repeated at 90° yielding  $V_{13P}$ ,  $V_{13N}$ ,  $V_{31P}$ , and  $V_{31N}$ . These 8 Hall measurements are reduced into 4 values according to Equation 3-3.

$$V_{ab} = V_{abP} - V_{abN} \quad 3-3$$

Where the subscripts ab are the orientation of the particular measurements 13, 31, 24, and 42. Since the carrier deflection and thus Hall voltage is reversed when the magnetic field is reversed, subtracting  $V_{abN}$  from  $V_{abP}$  removes any error from the contacts being offset or the sample not being perfectly square, leaving 2 times the Hall voltage as the resulting  $V_{ab}$ . The sheet carrier density is then calculated using equation 3-4.

$$c_s = 8 * 10^{-8} * \frac{I * B}{e(V_{13} + V_{31} + V_{24} + V_{42})} \quad 3-4$$

Where  $c_s$  is the sheet number, with a positive result indicating holes and a negative result indicating electrons.  $I$  is the applied current in Amps,  $B$  is the applied field in Gauss,  $e$  is the charge of an electron,  $1.6 \times 10^{-19}$  Coulombs, and the reduced Hall voltages come from the previous calculation. If the carriers are evenly distributed through the depth of a film, the carrier density can be calculated by dividing the sheet number by the thickness. Hall mobility  $\mu$  can then be calculated from the sheet number  $c_s$  and sheet resistance  $R_s$  according to Equation 3-5.

$$\mu = \frac{1}{e * c_s * R_s} \quad 3-5$$

For accuracy of the measurements, the contacts should be made as small as possible and in the absolute corners of the sample[139]. The equipment supplying the current and magnetic fields need to be stable and have no variation while measurements are being taken. The samples also need to be isolated from any sources of current leakage so that the applied currents are limited to the layer under test[140]. As mentioned above, the buffer structure used in this experiment ended with an undoped InAlAs layer immediately before the InGaAs layer growth. The InAlAs has a wider band gap than the InGaAs and being undoped acts as a semi-insulating barrier layer to the rest of the buffer structure.

### **Transmission Electron Microscopy**

Electron microscopy is advantageous because the wavelengths of high energy electrons is significantly smaller than easily produced electromagnetic radiation such as visible light or x-rays. In Transmission Electron Microscopy (TEM), electrons are

accelerated at a thin sample (on the order of 100nm) that the electrons can pass through. The electrons can be collected on the other side of the sample after interaction with the material to generate an image of the sample[141, 142].

The TEM achieves this by accelerating electrons from a thermionic emission or field emission source under high vacuum. Thermionic sources are typically a tungsten filament or LaB<sub>6</sub> crystal that is heated to excite electrons off of the surface. Field emission sources usually rely on a sharpened tungsten point from which electrons are stripped by an applied field near the tip. Thermionic sources have a higher total current yielding brighter images, but field emission guns have a narrower energy range for electrons that are extracted from the gun, yielding higher resolution.

The electron beam leaving the gun is accelerated using a high potential of usually 100kV to 500kV. Higher energies yield smaller wavelengths for the electrons and better resolution, but these energetic electrons also deposit energy into the sample when they experience inelastic scattering. For this reason, the study of most electronic materials is limited to 200keV. These electrons are then formed into a beam and directed at the sample using magnetic lenses and deflection coils. The best resolution is achieved with a balance between wanting a high numerical aperture, and limiting the spherical aberration of the lenses.

Bright Field (BF) imaging includes contrast from the sample mass, thickness, and diffraction off of planes within the sample. This means that it is important to have a sample of relatively uniform thickness and free of bends that may affect diffraction. Only unscattered electrons from the direct spot of the Diffraction Pattern (DP) are

included in the image. The strain around defects causes them to diffract more strongly and appear dark in images.

High Resolution TEM (HRTEM) includes more beams from the DP, which allows for interference between the elastically scattered electrons to generate phase contrast. This allows for lattice imaging, where a reconstruction that mimics the projection of the crystal structure is captured. HRTEM is good for obtaining more useful information about crystal and interfacial quality. This is especially important for studying the epitaxial layers in this work.

Scanning TEM (STEM) uses a converged beam unlike BF and HRTEM in which a parallel electron beam is incident on the sample. The converged beam is rastered across an area of the sample and the image is formed by detecting the intensity of the transmitted beam. The probe formed for imaging can be made smaller than the ultimate resolution of traditional TEM or HRTEM. The form of STEM used in this work is High Angle Annular Dark Field (HAADF) STEM. This means that an annular detector is placed under the sample and only the electrons that are highly displaced by elastic scattering are collected. HAADF-STEM gives contrast that is proportional to the square of the atomic number ( $Z$ ) of the atom off of which the electron scattered. This gives images of the columns of atoms along the zone axis, with intensities proportional to  $Z^2$  for the atoms within that column and is sometimes called  $Z$  contrast for that reason.

### **Focused Ion Beam Milling**

In order to prepare electron transparent samples for analysis in the TEM, a section of the sample needs to be thinned to around 100nm while introducing minimal damage. A Focused Ion Beam (FIB) system is useful in obtaining samples that meet this requirement. As the name implies, a FIB operates by using magnetic lenses to

focus an accelerated beam of gallium ions into a collimated spot on the sample.

Gallium is most frequently used because of its low melting temperature and low vapor pressure, resulting in a consistent, yet long lasting source[143]. The accelerating voltage is 30 keV or less with a current of the ion beam is in the pico Amp to nano Amp range, focused on an area around 10nm. This high current density and low energy result in mostly nuclear stopping and yield a high sputter rate with an efficiency usually between 0.1 and 100 sputtered atoms per incident ion. The beam can then be rastered over an area of the sample in order to mill away material from a defined area, and more importantly, leaving a specified region behind.

FIBs like the two used in this work, the FEI Strata DB235 and FEI Helios NanoLab 600, combine a FIB with a Scanning Electron Microscope (SEM). An SEM uses a focused beam of electrons similar to a TEM in STEM mode, but looks for secondary electrons ejected from the sample surface. This is a non-destructive way to select an area of interest and observe the sample during milling. In the case of these tools, the two systems are set 52° offset with concentric focus on the sample.

The preparation process starts with a carbon coating to protect the surface during milling. The carbon can be deposited from a heated carbon rod under vacuum, which gives the broadest and most uniform coverage, or by applying a robust organic layer with Permanent Marker Deposition (PMD)[144]. Once mounted and aligned within the FIB, a platinum strap is deposited using a platinum metalorganic precursor flowed over the area of interest and the energy of the rastering ion beam to deposit metallic platinum. Site selection is not critical here, since the samples are blanket growth, but the orientation does need to be aligned with a crystallographic axis for zone axis



alignment in the TEM. The platinum further protects the area of interest during milling and final thinning. Samples in this work were cut out using the in situ liftout technique[145]. Trenches are cut around the area of interest, then undercut so that the sample is mostly free from the substrate. An Omniprobe® micromanipulator is then welded to the sample before it is completely removed from the substrate. With the micromanipulator, the sample can be posted onto a copper TEM grid with another Pt weld, and cut free from the micromanipulator for final thinning.

The thinning process used was a simplified version of the procedure described by Schaffer et al[146]. Ion milling takes place at glancing angles on alternate sides of the sample, reducing the current, energy, and angle of the ion beam as the sample gets thinner. Because such an extremely thin sample as reported by Schaffer et al. is not necessary for most TEM imaging, thinning can stop at an earlier step than in their paper. The damage left by the gallium ions is greater, but over a thicker sample good quality samples are still achievable[147]. The end result is a 50-100nm thick sample with damage layers on either side of less than 3nm.

### **X-Ray Diffraction**

X-Ray Diffraction or XRD is one of the prominent ways to study the crystallography of materials. An XRD system consists of an x-ray source, a goniometer, some collimating optics, and a detector[148]. The x-ray source accelerates a high voltage electron beam at a metal source. The x-rays emitted are a mixture of the bremsstrahlung radiation from the sudden deceleration of the electrons and characteristic x-rays from energy transitions within the source material. By using either another material with an absorption edge just above the brightest characteristic peak or

diffraction off of a single crystal, the x-rays going onto the system can be filtered such that they are nearly monochromatic. These x-rays are then incident on the sample. These x-rays scatter off of the atoms within the sample, and due to the crystalline structure of the sample, they will diffract strongly off of any planes inclined to the incident beam. Constructive interference of the x-rays will occur when Bragg's law is satisfied as explained by Equation 3-6.

$$n * \lambda = 2 * d * \sin\theta \quad 3-6$$

Here  $\lambda$  is the wavelength of the x-rays,  $d$  is the interatomic spacing of the planes where diffraction is occurring,  $\theta$  is the angle of inclination between the x-rays and the plane of diffraction, and  $n$  is an integer. When the x-rays diffracting off of parallel planes with spacing  $d$ , those that have traveled an integer number of wavelengths will remain in phase with the reflections from the other planes. The integer term  $n$  is included because constructive interference would occur between multiple wavelength shifts of the x-rays. Since the x-rays have a wavelength similar to the interatomic spacing, diffraction orders greater than 1 generally only occur at shallow angles. Thus,  $n$  is assumed to be 1 and all possible  $h,k,l$  reflections are considered for their planar spacings  $d$ .

The goniometer controls the angles of the source and detector such that both are at equal angles to the planes being studied. Because Bragg's law relies on the reflection of x-rays, the source and detector must have the exact same angle to the plane of reflection in order to pick up that reflection. The detector is responsible for getting the intensity of reflection at every angle along a sweep of the source and

detector. The angles with high intensities will correspond to the planar spacing of the material when calculated back through Bragg's law.

### **Secondary Ion Mass Spectrometry**

To get accurate concentration and depth profiles in a material, Secondary Ion Mass Spectrometry (SIMS) is one of the few methods that is sensitive to the concentration used in electronics. Even when dealing with doping concentrations in the  $10^{20} \text{ cm}^{-3}$  range, this is still around or below 1% of the composition of the semiconductor. By most other methods like Energy Dispersive x-ray Spectroscopy (EDS), Electron Energy Loss Spectroscopy (EELS), or X-Ray Fluorescence (XRF), percentage level concentrations are the minimum detectable limit. With the right conditions, SIMS can be sensitive to impurity concentrations in the parts per billion which leaves a wide range of use that is necessary for studying semiconductors.

A SIMS source operates somewhat similarly to a FIB source which is described in Chapter 3. The beam acceleration, focusing and rastering all operate in the same way. The source is usually argon, oxygen, or cesium. As the name implies, SIMS uses secondary ions to determine the elements present in the sample, and reactive sources are useful because they have a higher probability of ionizing the sputtered atoms[149].

The sample sits in a vacuum chamber and the sputter beam is rastered over the sample to mill an area with a uniform depth. In dynamic SIMS, which is used here, the beam continuously rasters and elemental concentrations will be monitored throughout the whole process. To keep the concentrations accurate as the depth increases, the detector will only be on for a small portion of the area being milled. This prevents contributions from the sidewalls of the crater, which would have components of any

previous layers that were milled through. To exclude these ions, a focusing lens excludes ion not incident from the center of the raster area, and an electronic gate blocks ions from entering the detector while the beam is milling the edges of the crater[150]. Because the detector is positioned right above the sample, primary beam is incident to the sample at an angle and the flat area in the crater may be relatively small.

For the detector, an extraction voltage draws ionized atoms and clusters into the detector. A positive or negative secondary detection may be desirable depending upon the ionization potential of the elements being studied, and although multiple mass/charge ratios can be mapped in a single run, the extraction potential cannot switch fast enough to detect both at the same time. The three most common types of detectors are quadrupole, magnetic analyzer, and Time of Flight (ToF). A quadrupole mass analyzer uses 4 rods and an RF frequency to cause all but the desired mass/charge ratio to collide with the sides of the apparatus. The ions that reach the other end are counted. A quadrupole analyzer has a fairly low transmission which limits the minimum detection limit, but it has reasonable mass detection ranges and can be changed quickly allowing for multiple elements to be profiled essentially simultaneously. A magnetic analyzer bends the beam of ions through a strong magnet, with a slit at the end blocking all but a certain range of ions from reaching the detector. Magnets have better transmission giving them better low concentration sensitivity, have good mass selectivity and range, but cannot be changed quickly, limiting the number of elements that can be profiled at once. ToF detectors need no optics or ion manipulation because they pulse the primary ion beam and then measure the travel time of the ions accelerated by the extraction voltage. Heavier ions will travel more slowly and take

longer to reach the detector. These have the highest ion transmission and can detect a wide range of masses simultaneously for each pulse, but end up being very slow because each run of the detector requires a discrete pulse from the source rather than a continuous raster.

The resulting data is a plot of counts vs. time for the mass to charge ratios selected for the run. For initial runs it is beneficial to choose a large number of mass to charge ratios for the dopants, clusters of dopants and matrix atoms, etc. to make sure that they behave the same and are thus not affected by any unexpected clusters or contaminants of the same mass. Once these have been determined, just the mass/charge ratios with the strongest reliable signal can be selected for an actual run. With the detector switching between fewer mass/charge ratios, it will be able to get better depth resolution. However the depth still needs to be determined from the time. For a uniform sample where the sputter rate is constant, a profilometer scan of the crater after the run is adequate to scale the times and depths linearly.

Calibrating the concentrations requires a similar sample with a known concentration of the impurity being studied. In addition to the atoms being studied, ion yields are dependent upon the matrix and not necessarily linearly dependent on the composition of a multi-component matrix. As a result, the calibration sample needs to be the same matrix material as the sample being studied. For semiconductors it is easiest to get a sample ion implanted with the species being studied. The dose of the implant is precisely known. By performing SIMS on this control sample and correcting for the depth, the integrated profile counts in SIMS can be scaled to match the known dose. The same scale factor is then used on the profile of the test sample.

## **Atomic Force Microscopy**

Atomic Force Microscopy or AFM is a technique used to study the surfaces of materials and with the right setting can even image the arrangement of atoms on a clean surface. AFM uses a probe, usually etched out of silicon leaving a tetrahedron with a nearly atomically sharp tip, to interact with the surface of the material. Any attractive or repulsive forces from the sample deflect the tip, and a laser reflected off of the back of the tip measures this deflection. Rough movements of the probe height and sample are done with a motorized stage, although the scanning of the tip during measurement is done with piezo actuators integrated into the tip holder.

To operate an AFM, the tip and cantilever with a small silicon chip for handling are mounted on the probe holder and clipped into place with a spring. The probe holder is then mounted on the laser module and the sample placed on the stage. Small adjustment screws are used to align the laser onto the back of the probe cantilever, over the back of the tip. Another set of adjustment screws are used to align the detector so that the reflected laser hits its center. The quadrant detector measures voltage differences in the 4 bins, indicating how much laser light strikes each one. If the cantilever is deflected, the detectors will see a difference in the laser position. The scanning operation depends upon the mode being used.

In tapping mode, the resonant frequency of the probe and cantilever is tuned in free air. When scanning, non-contact interaction between the tip and sample shift the resonant frequency and amplitude of the oscillations. These changes are detected and the piezo stage is raised or lowered accordingly. A PID control loop and a set point for the degree of sample interaction to be maintained is used to translate the changes in tip interaction from the laser into movements of the stage. These need to be set such that

the stage responds quickly to changes in sample height, but does not oscillate, giving false data.

In contact mode, the tip is driven into the sample and dragged across. A set of PID controls are used again to set the probe to a desired level of deflection, and the fastest response possible from the piezo stage. A variation of contact mode is “ScanAsyst” which measures a force curve at each point of the scan rather than continuously dragging the tip. In this mode, the piezo stage drives the tip into the sample and the tip deflection is measured by the detector. In the previous modes, the surface height is determined by the position of the piezo stage, and the detector is used to input a new setpoint up or down into the PID control. In ScanAsyst, the surface height is determined as the onset of the cantilever deflection from contacting the surface. This method is faster since it does not require tuning a PID loop, and there is less tip wear than regular contact mode measurements.

## CHAPTER 4 ELECTRICAL DEACTIVATION OF SUPERSATURATED TE DOPING IN INGAAS

### **Deactivation of Heavily Te Doped Material**

The deactivation of heavily Te doped material has been reported in the past for GaAs and InP, so it is well established that supersaturated electrical activation of Te is possible. Early papers concluded that deactivation was the result of Te cluster formation because more deactivation was observed at higher doping levels, and the formation and diffusion of other defects such as vacancies was believed to be low[70, 151]. Later papers claimed to observe Te precipitation into dislocation loops, but disagreed on whether the loops were extrinsic[152–154] or intrinsic[155]. These studies used long anneals and inadequate surface protection, so they were most likely seeing effects of the GaAs degradation. More recent papers have determined that Te does not cluster in GaAs[156], and others with a more systematic approach have at least considered the possibility of vacancy formation[66], or even explored the mechanisms of defect formation as a function of temperature[157]. However, none of these papers ventured into Te behavior in InGaAs, leaving a technologically relevant hole in the literature.

### **Growth Parameters**

The samples in this experiment were grown at SEMATECH using the same growth conditions that resulted in the highest Te doping concentration from the previous paper by Orzali et al.[131]. An AIX-TRON CRIUS-R 300 mm MOCVD system was used to grow on 300 mm Si wafers. A buffer structure of approximately 350 nm of GaAs, 800 nm of InP and 300 nm of InAlAs were deposited. The InAlAs served as a semi-insulating barrier layer to enable accurate Hall effect measurements while remaining



lattice matched to InP. The structure of the  $\text{In}_{0.53}\text{Ga}_{0.47}\text{As}$  layers to be studied are outlined in Figure 4-1. The first sample consisted of 300 nm of InGaAs, a 50 nm layer of approximately  $1 \times 10^{18} \text{ cm}^{-3}$  Si doped InGaAs, and 150 nm of additional undoped InGaAs all grown at 600 °C. The temperature was dropped to 500 °C and 100 nm of heavily Te doped InGaAs was grown. The pressure during growth was 100 mbar with fluxes of trimethylgallium (TMGa), trimethylindium (TMIn), and arsine ( $\text{AsH}_3$ ) that were 275, 113, and 8530  $\mu\text{mol/min}$ , respectively. Diethyltelluride (DETe) at a flux of 0.13  $\mu\text{mol/min}$  was added in the Te doped layer. This yielded a growth rate of 2.2  $\mu\text{m/hr}$ , so the Te doped layer was only exposed to 2.7 minutes at 500 °C during growth. The InGaAs layer on the second sample had the same initial 300 nm of undoped InGaAs, 50 nm of  $1 \times 10^{18} \text{ cm}^{-3}$  Si doped InGaAs, but followed with 250 nm of undoped InGaAs to serve as a control sample. The use of and results from the Si marker layer will be discussed in Chapter 5.

### **Sample Surface Protection**

One of the challenges with annealing InGaAs, as discussed earlier, is the fact that the elements making up the semiconductor have different bonding potentials and different partial pressures when heated. This is a problem for many III-V materials, especially the Arsenides and Phosphides which are fairly common. It is well established that the partial pressures of arsenic and phosphorous are greater than gallium and indium when a III-V compound is heated[158, 159]. Furthermore, there is direct evidence that this leads to incongruent evaporation and a loss of the group V element under annealing conditions[160, 161]. This loss leaves group V vacancies that affect electrical properties as discussed in chapter 2. In extreme cases, so much of the

group V element may be lost such that the remaining group III element is left as metallic droplets on the surface of the wafer.

There are several approaches to avoiding surface degradation of the semiconductor. The first is to use a sealed tube with the samples to be annealed under which there is an overpressure of the group V element or a precursor of the group V element so that it is in equilibrium with the atmosphere at the annealing temperature and does not evaporate[162]. This can be time consuming and expensive, since for every anneal the samples need to be sealed in an ampoule that cannot be reused. The next approach is to create the overpressure locally by annealing the sample face to face with another sample of the same material or one with even greater evaporation so that the degradation of the second sample's degradation can protect the sample of interest[163, 164]. The final method is so far the most effective at protecting the surface. The samples are encapsulated in a dielectric so that there is a physical barrier to prevent evaporation[165].

An ideal encapsulant would be as conformal as possible in protecting the III-V material while otherwise not reacting with the III-V material, would not induce any strain into the material that could induce a change in dopant or point defect diffusion, and would be easy to deposit and remove without damaging the semiconductor.  $\text{SiO}_2$  was one of the earliest encapsulants, but Ga tends to diffuse into the  $\text{SiO}_2$  layer causing the problem of group III loss in place of group V loss[166].  $\text{SiN}_x$  was another readily available capping material, and its properties as a diffusion barrier were much better than  $\text{SiO}_2$ [165]. However, silicon nitride has a drastically different coefficient of thermal expansion than most semiconductors and generates significant stresses either as

deposited or under annealing conditions. One material that has come forward as a good capping material is  $\text{Al}_2\text{O}_3$ , since it does not exhibit the problems of  $\text{SiO}_2$  or  $\text{SiN}_x$ [167]. It can still be easily deposited and removed by hydrofluoric acid (HF).

Deposition methods include Chemical Vapor Deposition (CVD), Plasma Enhanced CVD (PECVD), and Atomic Layer Deposition (ALD). All three operate somewhat similarly to MOCVD. In CVD, the precursors are may be halides instead of exclusively organometallics. PECVD reduces the necessary deposition temperatures by creating a plasma above the sample to create radicals of the precursors. ALD relies on reactants that are self-limiting and alternates having just one precursor in the chamber at a time so that only on monolayer at a time is deposited. Depositing via ALD yields the best conformity of the layer and allows for thinner layers to be used.

For sample protection in this experiment, ALD deposited  $\text{Al}_2\text{O}_3$  layers were used.  $\text{Al}_2\text{O}_3$  deposition is actually close to the ideal ALD process because of the behavior of the trimethylaluminum (TMAI) precursor that is used[168]. Samples were loaded into an evacuated chamber on a platen. The chamber was pumped to  $10^{-2}$  torr and the platen was heated to  $250^\circ\text{C}$  for exposure mode deposition. A pulse of TMAI is introduced into the chamber with  $\text{H}_2$  as the carrier gas and allowed to saturate the surface of the samples for 30 seconds. This time allows the TMAI to chemisorb on the surfaces of the InGaAs as  $\text{Al}(\text{Me})_2$ [168, 169]. Once the surfaces are saturated, there are no more surface reactive sites for additional TMAI to chemisorb and physisorption is easily reversible leaving only a monolayer. The chamber is then purged with nitrogen and a pulse of water vapor is introduced in the chamber for another 30 seconds. The oxygen from the water reacts with the aluminum and the hydrogen completes the methyl groups

which leave as methane. Once all of the TMAI has been reacted with water, the additional water vapor is inactive on the  $\text{Al}_2\text{O}_3$  layer and it does not adsorb on the surface because the sample is at  $250^\circ\text{C}$  and the chamber sidewalls at  $150^\circ\text{C}$ , all well above the boiling point of water at the chamber pressure. The chamber is flushed with nitrogen again and this constitutes one cycle. This process grows  $1.15\text{\AA}$  of  $\text{Al}_2\text{O}_3$  per cycle. To grow an adequately protective layer of  $15\text{nm}$ , this required 136 cycles. The samples were then removed from the chamber and annealed as needed. After annealing and before measurements were taken, the ALD caps were stripped using a 6:1 Buffered Oxide Etch (BOE) solution for 10 minutes.

### **Hall Effect Results**

Indium metal contacts of approximately  $0.5\text{mm}$  diameter were pressed onto the corners of the  $10\text{mm}$  square samples. Copper wires were pressed on top of the indium contacts and the sample was placed in the holder of a MMR Technologies H-20 Hall and van der Pauw Measurement System. A tap off of the BNC connectors allows for easy testing for Ohmic contacts. A switch on the tap allows every combination of two contacts can be connected to a curve tracer which sweeps positive and negative voltages across the contacts selected to look for linear behavior. Once good contacts have been confirmed, the connection to the curve tracer is removed and the run is started. It measures the resistances across any two contacts and automatically chooses a current that keeps the total power through the sample below  $0.5\text{mW}$ . Currents and measurements are automatically rotated across the different orientations of the contacts, and all calculations are done automatically. A magnetic field of  $\pm 3500\text{ G}$  was applied via an external electromagnet and its strength confirmed with a calibrated commercial Hall Effect sensor.

The first anneals on this material were performed at 700 °C by RTA in an AG Associates HeatPulse 4100. The heavily Te doped samples were annealed side by side with the undoped samples in order to confirm that there was no variation in measured sheet carrier concentration as a result of temperature variations or any other means not caused by the deactivation of the Te layer. Post anneal, the Al<sub>2</sub>O<sub>3</sub> cap was removed by a buffered oxide etch (BOE) for 5 minutes at room temperature. Hall Effect of samples as grown and after being capped with ALD and stripped with BOE were nearly identical, showing that the capping and stripping processes did not alter the activation of the InGaAs layers.

Figure 4-2 shows the progression of electrical activation with time for a series of anneals at 700°C. The initial active electron sheet number decays exponentially to a stable level of about  $8 \times 10^{13} \text{ cm}^{-2}$ . The control samples had a sheet number of approximately  $4\text{-}6 \times 10^{12} \text{ cm}^{-2}$ , which did not change significantly with anneal indicating that the Si marker layer was contributing less than 1% to the initial measurement and still less than 10% to the fully deactivated, stable Te carrier concentration.

To study the energetics of the deactivation, additional anneals were performed across a range of temperatures, from 550 °C to 650 °C at times appropriate to capture the deactivation of the heavily doped Te layer. Anneals at 550-600 °C were 5 minutes or greater and carried out entirely in the furnace. Anneals at 625 °C – 650 °C crossed through both RTA and furnace time scales, so an overlap of one point at 5 minutes with both anneal methods was used to confirm that they achieved similar results. SIMS profiles of the Te performed in Chapter 5 indicate that there is no diffusion during the amount of time necessary for deactivation, so the electron concentrations are

normalized to the 100nm thick Te doped layer. The results of all of these anneals are shown in Figure 4-3.

The mobility of the samples during deactivation is plotted in Figure 4-4. As expected, there is an increase in mobility as the material deactivates, since there is less ionized impurity scattering as fewer Te atoms donate an electron. For comparison, the mobilities of the control samples are plotted in Figure 4-5. These samples have smaller relative changes, likely due to slight variations in extended defects across the wafer. The standard deviation of the control samples was used to generate the error bars used in Figure 4-4. Comparing the mobility to the carrier concentrations during the deactivating anneals, as shown in Figure 4-6, the inversely proportional relationship between the carrier concentration and mobility is consistent across deactivation at different temperatures. The variation in mobility across temperatures is within the margins of error for most data points, suggesting that the deactivation mechanism is the same across all temperatures.

By using the control samples as a baseline mobility for the InGaAs and any extended defects, the contribution of ionized impurity scattering in the Te doped samples can be extracted using Matthiessen's rule. Extracting the ionized impurity mobility contribution from several samples at different temperatures before and after deactivation yields approximately  $2100 \text{ cm}^2\text{V}^{-1}\text{s}^{-1}$  for the starting material and  $3400 \text{ cm}^2\text{V}^{-1}\text{s}^{-1}$  after deactivation.

Since the charge and effective mass of an electron are not changing, the change in mobility is directly proportional to a change in the time between scattering events. However, for a fivefold decrease in electron concentration, the scattering time only

increased to 1.6 times its starting value. Since all of the Hall Effect measurements were taken at room temperature, the thermal velocity of the electrons was the same, leaving the density of scattering sites and their scattering cross section as potential factors influencing the change in scattering time. Making the assumption that the remaining ionized impurities have the same scattering cross section before and after deactivation, the limited change in mobility must come from the presence of a new defect. This is consistent with prior studies that reported reduced mobilities as a result of defect scattering in highly doped, inactive material[35, 44]. However, without knowing more about the inactive Te defect, the concentration and scattering cross section cannot be determined from mobility alone.

### **Arrhenius Relation**

Fitting exponential curves like the one in Figure 4-2 to all of the curves in Figure 4-3, a decay constant for each of the anneal temperatures can be extracted. By plotting the log of these decay constants against the inverse temperature in Figure 4-7, the thermally activated behavior becomes apparent. Fitting a line to this curve yields an activation energy of 2.6 eV. This correlates to the activation energy of the deactivation mechanism for Te. Since there are no kinks in the fit for activation energy, the rate limiting step in deactivation does not change over the temperature range studied.

### **Consistent Equilibrium Activation**

Curiously, the deactivation progresses to  $7-8 \times 10^{18} \text{ cm}^{-3}$  for all temperatures. Generally dopants would deactivate to different equilibria at different temperatures based on the energetics of the dopant at that temperature[44, 134]. These samples were not quenched from their anneal temperature, but with the amount of time it takes for deactivation at some of the lower temperatures, they are not spending sufficient time

at those temperatures to reach a low temperature equilibrium on the ramp down after anneal. With an activation energy that fits across the whole temperature range, whatever mechanism is deactivating the Te seems to be thermodynamically temperature independent.

These equilibrium solubility levels after deactivation are also significantly lower than stable activation levels for other dopants in InGaAs, such as Si[77] which deactivates to  $1.5 \times 10^{19} \text{ cm}^{-3}$ . Therefore despite having a more promising as grown n-type electrical activation than Si in InGaAs, the final deactivated concentration is half of the Si value so it will be even more important to limit the post growth thermal processing for Te doped InGaAs.

### **No Clustering Visible**

BF and HRTEM was performed on a JEOL JEM-2010F operated at 200keV to get the best resolution possible while minimizing knock on damage from the electrons. HRTEM was performed using 13 beams from the InGaAs DP. Cross sectional TEM of the structure in Figure 4-8a shows the final Te doped layer is 100 nm, and the total InGaAs layer thickness is about 600 nm. This image was taken after a 700 °C 2 minute RTA to deactivate the Te doping, but the samples look the same as grown and after anneal. An interface is visible where the Te doping begins because of the break between the bulk InGaAs growth at 600 °C and the Te doped layer grown at 500 °C. HAADF-STEM on an aberration corrected JEOL JEM-ARM 200cF TEM in Figure 4-8b does not show any macroscopic precipitates or incoherent phases in the Te doped surface layer after deactivation of the Te doping to an equilibrium level as indicated by Hall Effect. Any pure Te phase and most alloys of Te with Ga, In, or As are hexagonal



or monoclinic and should appear in HAADF-STEM if they consist of more than a few atoms[170].

However, the atomic number difference between Te and In in the matrix is fairly small, so it is difficult to discern any clusters of Te in the InGaAs matrix. Small clusters of only a few Te atoms or complexes of a Te atom with another point defect could be responsible for deactivation without being visible by TEM. For this reason, we must look to the diffusion of Te to rule out Te clustering.

Using the diffusivity of Te at 700 °C, the characteristic diffusion length at 30 seconds (the first point at which the Te is deactivated to an equilibrium value) is 0.66nm. For our material with a peak Te concentration of  $6.3 \times 10^{19} \text{ cm}^{-3}$  and assuming a uniform distribution, the average distance between Te atoms in the InGaAs is 2.5nm. This means that in the time scale where deactivation is occurring, two Te atoms are unlikely to diffuse far enough meet, and certainly not enough would do so for electrical activation to drop by a factor of 5.

### **Summary**

The deactivation of heavily doped, electrically supersaturated Te doping in InGaAs was studied for a range of temperatures from 550 °C to 700 °C. The Te doping is found to deactivate from  $4.4 \times 10^{19} \text{ cm}^{-3}$  to  $6\text{-}7 \times 10^{18} \text{ cm}^{-3}$  for all temperatures studied. The rate of deactivation was measured and from this an activation energy of 2.6 eV was determined for the rate limiting step of the deactivation process. HAADF-STEM and other TEM studies did not show any macroscopic precipitate formation suggesting that submicroscopic clusters or point defect complex formation may be responsible for the deactivation.

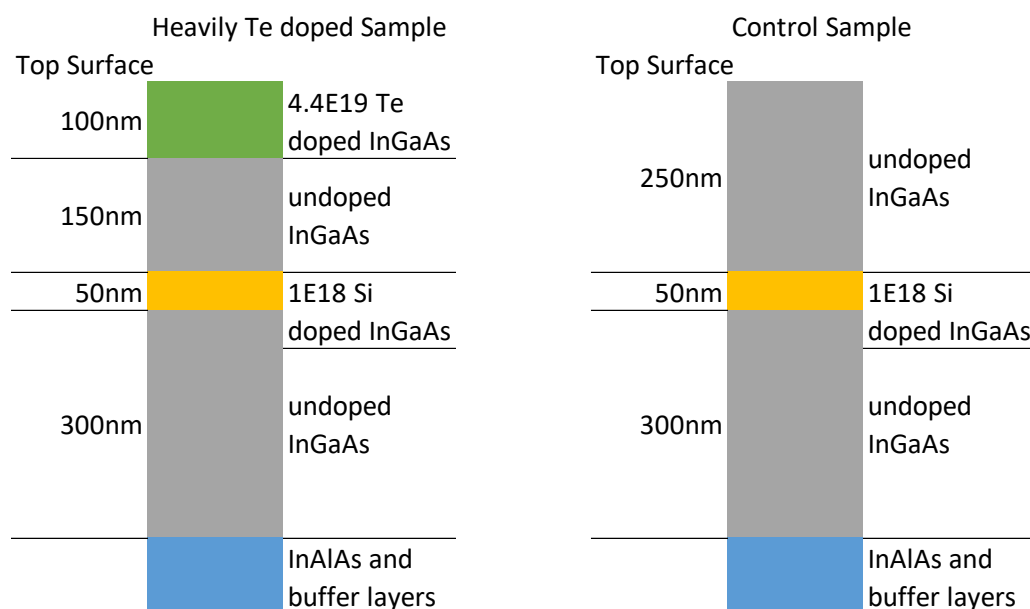


Figure 4-1. Final InGaAs structures for heavily Te doped and control samples with 50nm Si marker layer buried 150 nm below the Te layer.

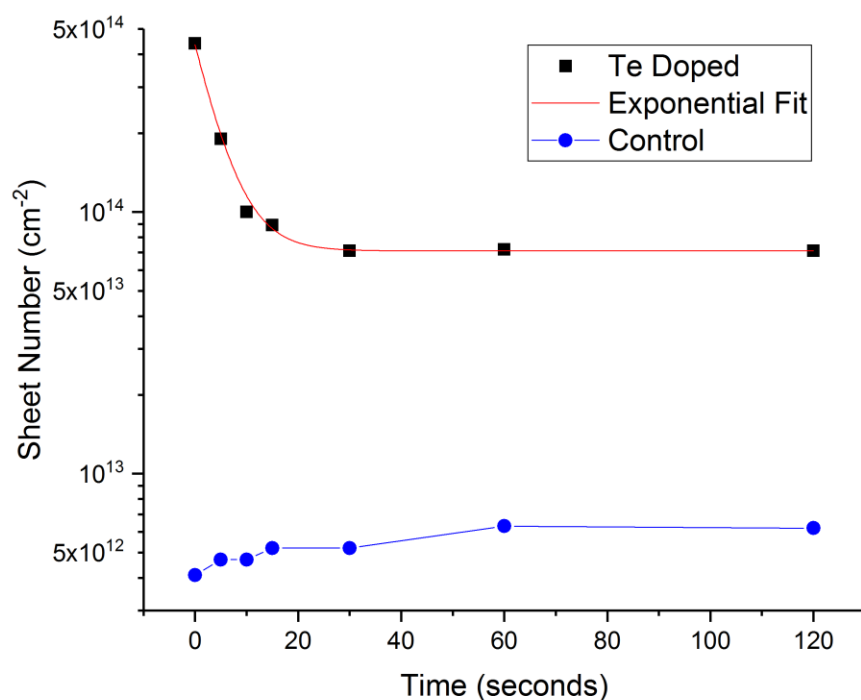


Figure 4-2. Hall Effect data for a time series of anneals at 700°C showing the minimal change in the control sample and deactivation of Te from  $4.4 \times 10^{14} \text{ cm}^{-2}$  to

$7 \times 10^{13} \text{ cm}^{-2}$ . The smooth line represents an exponential fit of the data to extract a deactivation rate

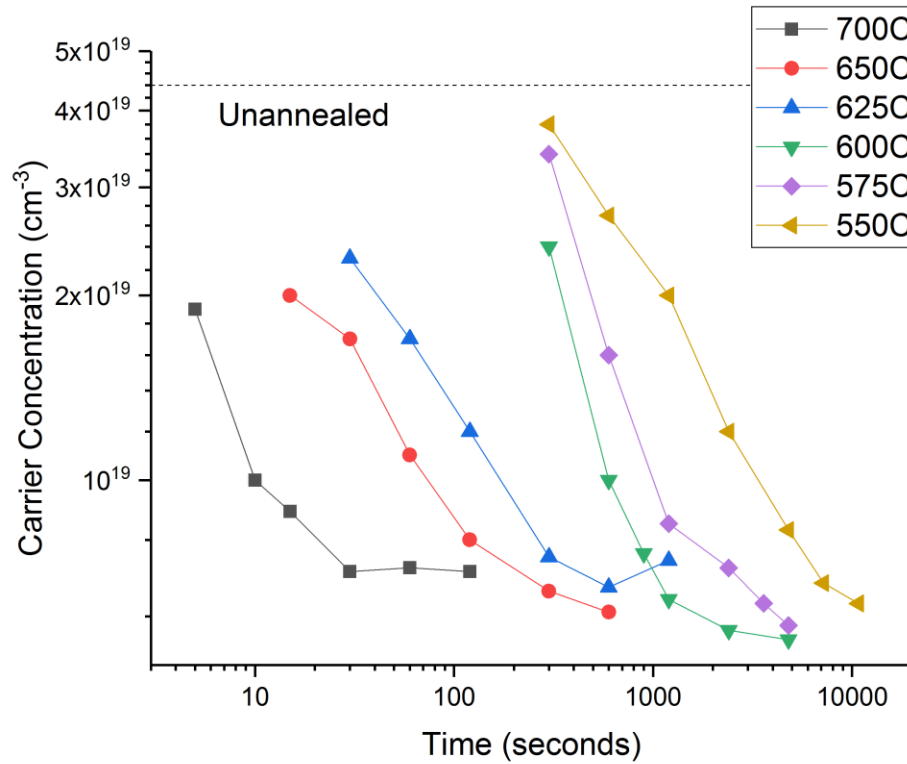


Figure 4-3. Deactivation curves for all anneal temperatures on a log time plot with all anneal temperatures deactivating to a similar value of  $7\text{-}8 \times 10^{19} \text{ cm}^{-3}$ . The dotted line represents the starting carrier concentration for all samples.

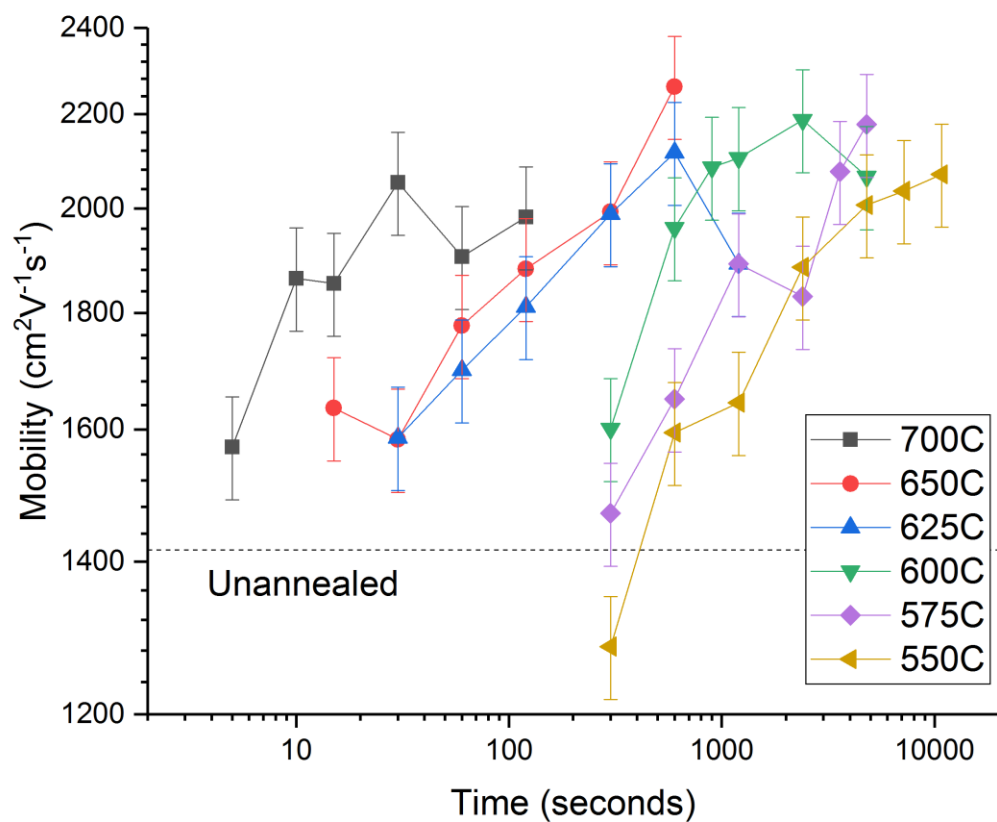


Figure 4-4. Mobility changes in the Te doped samples during deactivation. Mobility increases, but not nearly to the level of the undoped material, meaning that there is still some defect scattering lowering the electron mobility.

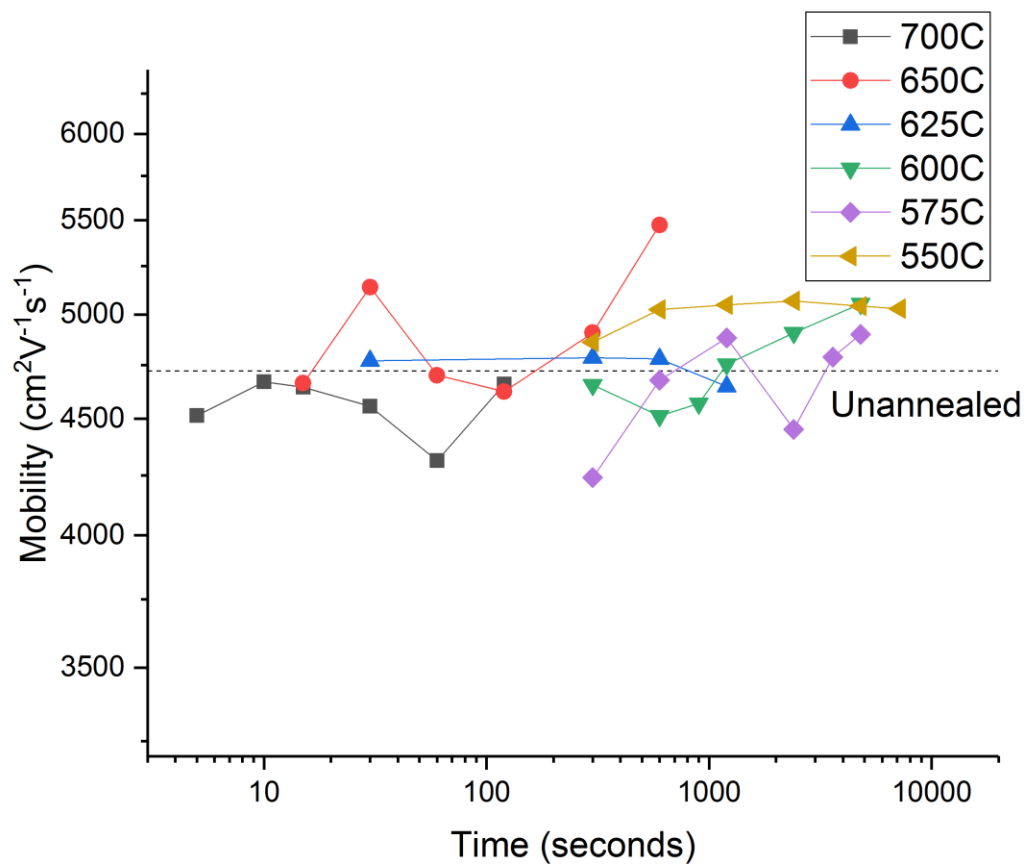


Figure 4-5. Mobility changes in the undoped samples during the same anneals as the deactivating Te doped samples.

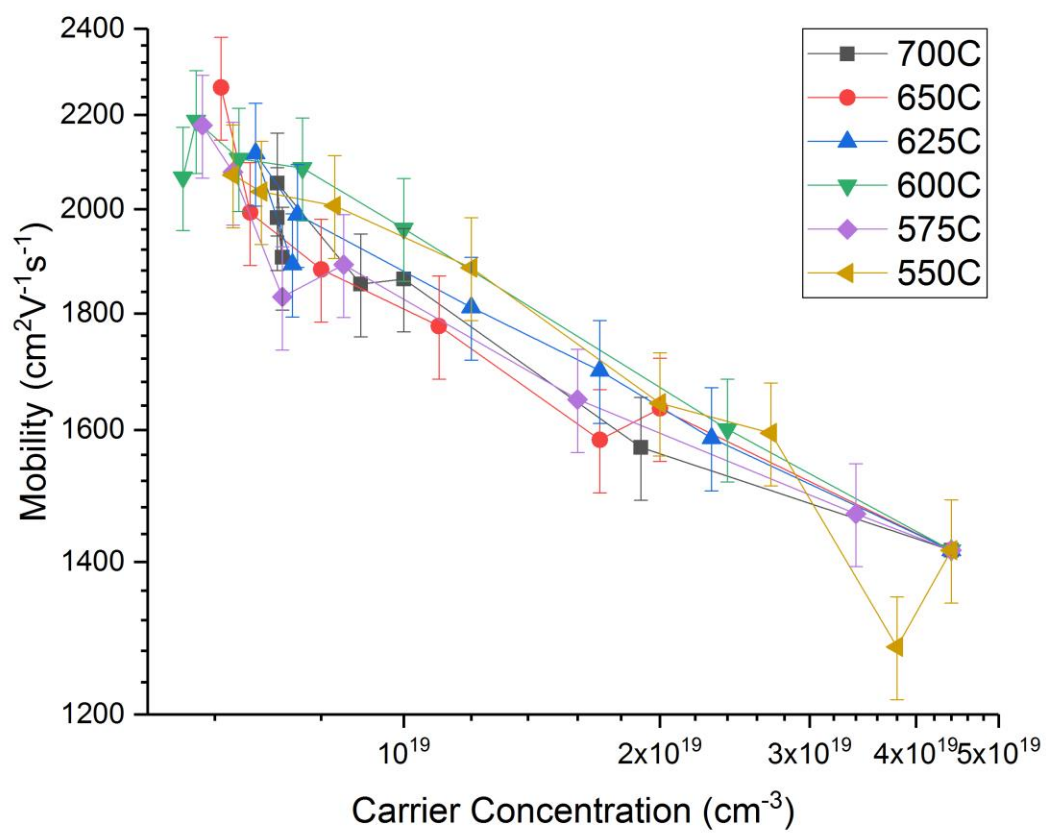


Figure 4-6. Comparison of mobility and carrier concentration during deactivation.

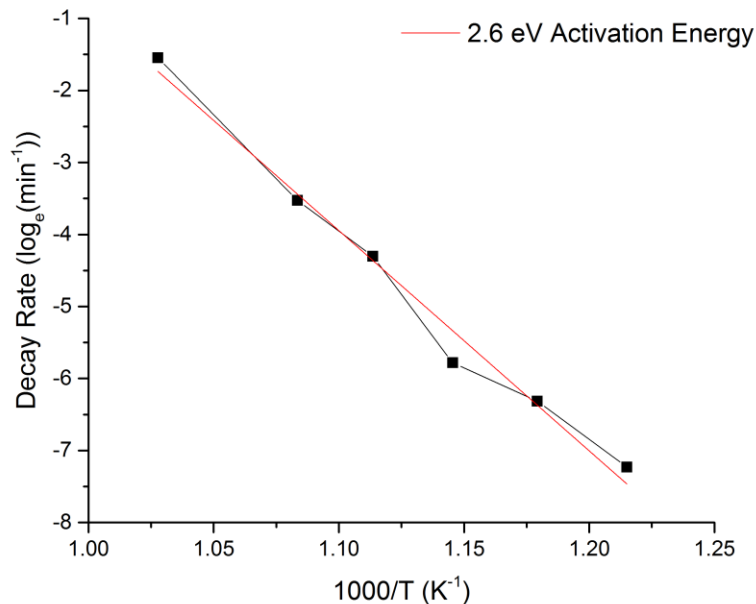


Figure 4-7. Arrhenius plot of electrical deactivation time constants over all anneal temperatures, showing an activation energy for the deactivation mechanism of 2.6 eV

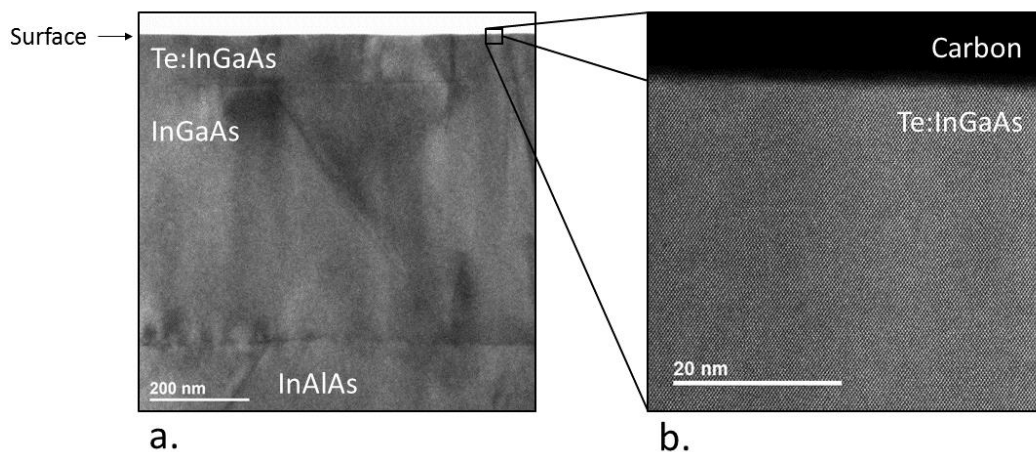


Figure 4-8. TEM of the MOCVD grown InGaAs structure after a 700 °C 30 second anneal. A) XTEM of InGaAs structure a after 700°C 2 minute anneal showing 100nm of Te:InGaAs on top, 500nm of additional InGaAs, and the InAlAs layer at the end of the buffer structure on bottom. The clarity of the interfaces is the same as the appearance as grown. B) HAADF-STEM of the same sample on an aberration corrected TEM looking at the Te doped layer, where no large precipitates of Te are visible

## CHAPTER 5 EXPERIMENTAL INVESTIGATION OF POINT DEFECTS AND TE DOPING

### **Strain of Te**

When doping GaAs, InAs, or InGaAs with Te, the lattice constant is expected to expand because the Te is substituting for an As atom, while having a larger atomic bonding radius than As would in the same position. Early studies of highly Te doped GaAs saw a superdilation of the lattice constant above concentrations of about  $3 \times 10^{18} \text{ cm}^{-3}$  [171, 172]. This was a dilation of the lattice constant sometimes as much as 15 times the expansion expected by Vegard's law when substituting a Te atom on an As site. However, they assumed that the physical Te concentration was reflected by the carrier concentration of the material. More recent studies have been able to show that when growing in Te doping in GaAs or InAs, the achievement of above activation electron concentrations often comes with a large inactive fraction of Te incorporated in the material as well [43, 44, 173]. Furthermore, when strain measurements are correlated with the actual concentrations of Te in the material, the lattice dilation is found to be less than predicted by Vegard's law, and they proposed that it was the result of compensating vacancies that contracted the lattice [173]. Since a Te vacancy complex is one of the proposed mechanisms for the deactivation of the material in this study under anneal, and a strain change due to vacancies may be observable by XRD, the lattice parameter of the Te doped material could be useful to determine if vacancies are involved in Te deactivation. If group III vacancies form to deactivate the high Te doping concentration, a greater number of vacancies after deactivation might be apparent as a contraction in lattice constant.



## X-Ray Diffraction Results

In order to study the evolution of strain in the Te doped samples, XRD was used to measure the lattice constants of the material. The same Te doped samples from the deactivation experiment were used, consisting of a Si wafer with 350nm of GaAs, 800nm of InP, 300nm of InAlAs, 300 nm of undoped InGaAs, a 50 nm layer of approximately  $1 \times 10^{18} \text{ cm}^{-3}$  Si doped InGaAs, 150 nm of additional undoped InGaAs, and the 100nm layer of  $6.3 \times 10^{19} \text{ cm}^{-3}$  Te doped InGaAs. The electrically active portion of Te as grown is  $4.4 \times 10^{19} \text{ cm}^{-3}$ , so there are likely some vacancies already present if a Te-V<sub>III</sub> cluster is the true deactivation mechanism.

The XRD in this work was performed on a Panalytical XPert MRD using Cu K $\alpha$  x-rays with a wavelength of 1.542Å. The (004) reflection was studied, since these planes are the ones parallel to the polished surface of the wafer, allowing for the measurement of lattice spacing orthogonal to the surface. The scans are shown in Figure 5-1. On the far right is the Si peak from the substrate, in the middle is the peak from the GaAs in the buffer layer structure and superimposed on the left are the peaks from the InP, InAlAs, and InGaAs. This superposition of multiple materials which may not be perfectly lattice matched, along with the likely high defect density from relaxation of the heteroepitaxial layers unfortunately makes the last peak fairly broad[174]. A HRXRD scan of just the InP, InAlAs, and InGaAs peak is shown in Figure 5-2. The two lines plotted are the control sample with no Te doping and the sample with the Te doped layer.

Unfortunately there is little difference between the two, so it would likely be difficult to see any reduction in the lattice constant of the Te layer from the formation of additional

vacancies. In fact, the variation across the wafer in just the control sample was similar to the difference seen between these two samples.

The material that these samples were based on, grown by Orzali et al. had been measured by XRD and found significant lattice dilation[131]. However, their measurements were taken on a separate sample with fewer buffer layers to reduce the interference that was observed here. Also, despite having only a slightly higher electrical activation at  $6.3 \times 10^{19} \text{ cm}^{-3}$  by measurements on our Hall Effect system, compared to the material in this study with a  $4.4 \times 10^{19} \text{ cm}^{-3}$  carrier concentration, the physical Te concentration needed to achieve that difference was almost an order of magnitude higher at  $5.5 \times 10^{20} \text{ cm}^{-3}$  compared to our samples with  $6.3 \times 10^{19} \text{ cm}^{-3}$ . The methods used to determine the chemical concentration of Te in these samples is explained in the next section.

### **Early SIMS Results**

The SIMS runs throughout this experiment were taken on a PHI Adept 1010 dynamic SIMS system. The primary beam was 20nA 3keV  $\text{Cs}^+$  while the quadrupole detector was set to pick up negative secondaries with a 10% detection area on a 500 $\mu\text{m}$  square raster. The first goal was to confirm that there was no substantial diffusion of Te during the deactivating anneals. Confirming the lack of diffusion was necessary for calculating carrier concentrations from hall effect in Chapter 3. A second Te doped InGaAs layer with a Te concentration of  $7.8 \times 10^{19} \text{ cm}^{-3}$  was used for calibration. This first SIMS run, shown in Figure 5-3, shows the resulting profiles. It appears that in the first 30 seconds of annealing at 700°C there is a low concentration tail diffusing at a much faster rate than the majority of the Te. After 4 hours, the Te diffusion from the

layer seems to have overtaken the low concentration diffusion without any additional tail diffusion. This was surprising, since there are no reports of transient Te diffusion in InGaAs or similar III-Vs like GaAs or InAs.

To study this more systematically, additional anneal times from 5 seconds to 1 minute were added to look for the progression of this diffusion tail. Unfortunately, the diffusion tail was not well behaved. There were apparent variations across the wafer when comparing other 2 minute 700°C anneals, and some shorter times showed more diffusion than later times. This tail was clearly an artifact from another source. By scanning through mass/charge ratios, significant fluorine signals were apparent in some particles or pits on the surface. The Te background measurements tracked with the F signal, indicating that the fluorine's presence was artificially creating the Te tails. This can be seen in Figure 5-4 since the F and Te profiles decay at the same rate. Since the ALD caps were removed using HF, it seemed that this was the most likely source of the contamination.

### **Polishing of ALD Caps**

Since TEM cross sections showed a smooth surface before and after Al<sub>2</sub>O<sub>3</sub> deposition and removal, polishing the caps off seemed like the best alternative. Polishing is risky, because the protective cap is likely harder than the underlying InGaAs, and the Te doped layer of interest is only 100nm thick. Polishing was performed with a levelled hand chuck on felt pads using a syton final polish suspension. Ellipsometry was used to confirm the removal of the Al<sub>2</sub>O<sub>3</sub> layer and measure the remaining InGaAs layer thicknesses. The results from SIMS run on one of the polished samples is shown in Figure 5-5. The Te profile is narrowed since some of the layer has

been removed, but the layer now appears so blurred that any tail or artifacts would be impossible to discern. It looked like the polishing had roughened the surface. With a rough surface, the primary ion beam will transmit the topography down into the sample as it mills, and any abrupt interfaces will appear blurred because the surface being sputtered will intersect with this interface at varying times throughout the milling process. As a result, it was necessary to look at the surfaces of the InGaAs before running SIMS.

### **AFM Results**

AFM was used to evaluate the surface roughness of the samples before and after capping, annealing, and HF stripping the protective cap. In this work, a Bruker Dimension 3100 SPM/AFM was used in tapping mode, and a Bruker Dimension Icon AFM was used in ScanAsyst mode. Images of the InGaAs surfaces obtained by AFM are shown in Figure 5-6. A pristine sample of the Te doped InGaAs as grown is shown in 5-6a. There is some roughness to the sample, most likely from the relaxation of the buffer layers during growth. The difference in scale between the x-y axes and the color mapped z axis should be noted. Although it appears rough, these are actually variations of 30nm over 5 $\mu$ m laterally. Although some variation is visible in TEM images, those samples are much smaller and the magnification needed to see the vertical topographical variations in cross section limits the width that can be viewed. Image 5-6b shows a sample that has been capped with Al<sub>2</sub>O<sub>3</sub>. As expected from ALD the layer is conformal to the growth surface and maintains the same texture. A scan of the InGaAs surface with the cap removed is shown in 5-6c. This sample shows a large degree of roughness and appears to have two differentiated layers. Either the Al<sub>2</sub>O<sub>3</sub>

cap is not etching uniformly from the sample or the HF is attacking the InGaAs once it gets through the  $\text{Al}_2\text{O}_3$  and causing roughening of the layer of interest. The fourth image in part 5-6d was the polished sample. This sample is the flattest of the four, and flatter than the as grown material. It is apparent that the polishing was not damaging the surface, but rather flattening it.

Some papers have reported roughening of Te doped GaAs at low temperatures[175], but since the sample was rough to start and SIMS on as grown samples show abrupt interfaces, it appears that the roughness in these samples started before the Te doped layer was grown. This means that the growth was transferring the roughness from the buffer layers up through the Te layer during growth and SIMS was transferring the topography down during milling. By polishing the sample before performing SIMS, the SIMS interface was then flat and it encountered the rough Te doped/undoped InGaAs interface gradually. Although polishing was theoretically making the surface flatter, it is not a viable option for SIMS preparation.

### **Revisiting Atomic Layer Deposition**

Based on the non-uniformity of HF etching that was apparent in Figure 5-6c, there was some worry that the  $\text{Al}_2\text{O}_3$  cap was not adequately protecting the semiconductor surface. Although the 15nm exposure ALD deposited cap had worked previously on other InGaAs samples, there are also reports of trapped hydrogen forming blisters in  $\text{Al}_2\text{O}_3$  protective caps during anneal[176, 177]. These stem from the water vapor used to oxidize the TMAI precursor during deposition. This blistering delaminates the  $\text{Al}_2\text{O}_3$  from the semiconductor and leaves an unprotected region. The unprotected

regions are then subject to degradation and As evaporation. Although HF is highly selective to oxides, the degraded regions may be more susceptible to etching.

Upon inspection of capped samples after anneal but before the HF strip, blisters were observed under optical microscopy. A sample image of one of these blisters is shown in Figure 5-7a. Figure 5-7b shows an AFM scan of one of the blisters with the dome shaped roof apparent.  $\text{Al}_2\text{O}_3$  layers can be deposited by ALD with an  $\text{O}_2$  plasma instead of using  $\text{H}_2\text{O}$  as the oxidizing species. These layers had previously been avoided because they have a higher prevalence of pinholes and during the first few layers of deposition there is a risk of oxidizing the semiconductor. This is because the surface coverage of TMAI on the semiconductor surface is not as uniform as it is on  $\text{Al}_2\text{O}_3$ . The exposure mode with each precursor spending a long time to saturate the surface helps to get a uniform nucleation layer.

As a result, a hybrid recipe was developed which deposits 5 layers of exposure mode  $\text{Al}_2\text{O}_3$ , followed by the remaining portion of the 15nm layer in plasma mode. The first few layers act as a nucleation layer for the  $\text{Al}_2\text{O}_3$  and protect the InGaAs from being damaged or oxidized by the  $\text{O}_2$  plasma. These few layers do not contain enough H to accumulate into voids or blisters, and the subsequent  $\text{Al}_2\text{O}_3$  is able to protect the surface of the InGaAs.

After annealing, these hybrid recipe capped samples did not have any blistering visible under an optical microscope. However, after a HF strip to remove the  $\text{Al}_2\text{O}_3$  AFM still showed a non-uniform surface similar to the one in Figure 5-6c. Because there was no reliable way to remove the cap and maintain the original surface of the InGaAs, it was decided to run SIMS on the samples with the  $\text{Al}_2\text{O}_3$  cap still on the sample. Oxides

have much higher ion yields and lower sputter rates than most semiconductors, which means that the  $\text{Al}_2\text{O}_3$  layer will not appear the proper depth without a separate calibration. However, since no profiling of dopants in the oxide is necessary, the sample depth can be calibrated for the InGaAs only. The surface will be at the end of the oxide layer and although the Te is diffusing, the depth can be adjusted to center the marker layer depth at the same position as the unannealed samples.

### **Te Diffusion**

SIMS runs with the  $\text{Al}_2\text{O}_3$  layer intact yielded the Te profiles seen in Figure 5-8. These profiles are shifted so that the interface between the  $\text{Al}_2\text{O}_3$  layer and the InGaAs is centered at a depth of 0. Because the  $\text{Al}_2\text{O}_3$  and InGaAs mill at different rates, using a single depth from a profilometer would yield a thickness for the  $\text{Al}_2\text{O}_3$  layer that is about 6 times thicker than the 15nm it is known to be. As a result, the profiles are scaled according to the depth of the Si marker layer. It also showed some diffusion during the anneals, but a more detailed explanation of the marker layer is in the following section. The Te profiles show a slow progression of diffusion outward from the starting box like profile. Since the scale of profiles spans 5 hours with only a few nanometers of diffusion, it is clear that the diffusion of Te in InGaAs at 700°C is slow. In order to determine an actual diffusivity for the Te, some empirical modelling is necessary.

### **Diffusion Modelling**

The simulation software used to model the Te diffusion was the Florida Object-Oriented Process Simulator (FLOOPS). This is a form of Technology Computer Aided Design (TCAD) software that is used to reproduce and predict semiconductor structured from physics based empirical models. For process development, a mesh grid is

generated to simulate the semiconductor and processing steps such as growth, oxidation, etching, implantation, and diffusion can all be modeled. The concentrations of dopants, defects and other properties are transmitted from point to point in the mesh through differential equations just like finite element analysis in mechanical simulations.

For the Te diffusion, a simple Fickian diffusion model was used to determine the diffusivity according to Fick's second law as shown in Equation 5-1. The one dimensional case is used because the blanket layer of Te makes the concentrations uniform in all other directions[178].

$$\frac{\partial C}{\partial t} = D * \frac{\partial^2 C}{\partial x^2} \quad 5-1$$

Here C indicates the concentration of a dopant at any point and time, t is time, D is the diffusion coefficient, and x is the position within the material. This shows that in any place where there is a changing concentration gradient, a flux of material will increase or decrease the concentration at that point over time at a rate dependent upon the diffusivity.

By loading SIMS plots of the starting Te profile and running simulations on that profile with different diffusivities, a diffusivity can be determined that matches the SIMS profile of the annealed sample after the same amount of time. The fitting of diffusivities to the SIMS data is shown in Figure 5-9. Because the diffusion is so slow and near the depth resolution limits of SIMS, the errors associated with fitting are large and in some cases extend into what would be a contraction of the profile or a negative diffusivity. Nonsensical data was ignored when determining the overall diffusivity of Te. The average of the diffusivities extracted from FLOOPS for Te in InGaAs was  $3.6 \times 10^{-17} \text{ cm}^2\text{s}^{-1}$ . This falls between the literature values at 700°C for Te diffusivity in GaAs at



$1.1 \times 10^{-19} \text{ cm}^2\text{s}^{-1}$  and InAs with  $8.0 \times 10^{-12} \text{ cm}^2\text{s}^{-1}$ [179–181]. The comparison of where these values lie is shown in Figure 5-10. Since InGaAs an alloy of the two materials, it is expected that the diffusion properties would fall in between the two materials, and including error, the diffusivity measured here follows Vegard's law.

### **Marker Layer**

Because of the preference for GaAs to form Ga vacancies when heavily n-type doped and the energetic favorability for their formation from Frenkel pairs[47, 49], the deactivation process would create a flux of interstitials that are free to diffuse out of the deactivating layer while the vacancies remain in the layer to deactivate the doping. Since InGaAs is similar to GaAs, it was suspected that the deactivation of Te would likely follow a similar mechanism. The use of marker layer diffusion is a common way to monitor the flux of point defects. The marker layer is chosen to be a dopant known to diffuse through either a vacancy or interstitial mechanism almost exclusively. Two samples are grown, one with only the marker layer to get a baseline diffusivity, and the second with the marker layer and the potential source of point defects under study. If the diffusivity of the marker layer increases or decreases, it is then known that there were more or fewer of the point defects of the type that the marker layer uses to diffuse.

Since it is easier to see an enhancement in diffusion, rather than retardation, the ideal marker layer dopants for this study are Be or Zn because they are known to be group III interstitial diffusers[182]. Unfortunately neither of these dopants were not available from the MOCVD growers at SEMATECH. Si doping was available, and it diffuses through a vacancy mechanism on the group III sublattice[183–185]. If the deactivation process injects interstitials into the InGaAs, it would likely slow the Si

diffusion by recombining with the native vacancy population in the material. If Frenkel pair formation was the sole mechanism for deactivation and each vacancy took on three negative charges, The deactivation of Te from  $4.4 \times 10^{12} \text{ cm}^{-2}$  to  $8 \times 10^{11} \text{ cm}^{-2}$  would generate  $1.2 \times 10^{12} \text{ cm}^{-2}$  excess interstitials in the Te doped layer. At  $700^\circ\text{C}$  the equilibrium concentration of vacancies in GaAs is below  $10^{14} \text{ cm}^{-3}$ [49], so even with significant diffusion and loss to the surface, there should be more than enough interstitials to annihilate vacancies in the InGaAs.

Because Si is also an n-type dopant, one important factor is to keep the Si concentration below a concentration where it starts to be deactivated, since this would then generate vacancies in the marker layer region and swamp out any injection from the Te deactivation[186, 187]. The maximum concentration before this occurs seems to be  $3 \times 10^{19} \text{ cm}^{-3}$  for Si, so a marker layer concentration of  $1 \times 10^{18} \text{ cm}^{-3}$  was chosen[188]. The marker layer was placed 150nm from the Te layer so that the profiles would not run into one another when diffused. The diffusivity of Ga vacancies and interstitials is faster than that of Si, so there is no worry about the point defects reaching the Si marker layer[189].

SIMS of the Si profiles was performed simultaneously during the runs that resulted in Figure 5-8 mentioned above. The sputter rates and conditions were the same, although a  $5 \times 10^{14} \text{ cm}^{-2}$  10 keV Si implant into InGaAs was used as the calibration sample. The Si profiles for the control sample are shown in Figure 5-11. By importing these into FLOOPS and matching the profiles over time, the diffusivities shown in Figure 5-12 were extracted. An overall diffusivity of  $6 \times 10^{-17} \text{ cm}^2\text{s}^{-1}$  was determined for the baseline Si diffusivity in InGaAs. Figure 5-13 shows the Si profiles for samples with the

Te doped cap. The diffusion of these layers looks almost identical to the control samples, with differences that are within the margins of error. Fitting diffusivities to these samples in Figure 5-14 yields  $6 \times 10^{-17} \text{ cm}^2\text{s}^{-1}$ , the same as the control sample. Superimposing the profiles of the two samples as shown in Figure 5-15 indicates that they are essentially identical as grown in 5-15a, and not far off from one another after 4 hours in plot 5-15b.

The similarity of the results could be from the already slow diffusion of the Si, making slowed diffusion difficult to detect. Although this experiment was unable to confirm the deactivation through a Frenkel pair formation mechanism, it conclusively rules out any deactivation that would inject group III vacancies. It is still possible that Frenkel pairs were created, but the interstitials may have diffused to the surface and combined into additional semiconductor material rather than moving down into the bulk.

### **Modifying Deactivation Kinetics**

To further explore the stability of Te doping in InGaAs, the subsequent experiments were designed to alter the point defect populations in the material with the hope of thus altering the formation energies of compensating defects.

#### **Strain**

The first method was the use of strain. Since vacancies leave empty space within the lattice, the atoms surrounding the vacancy relax into this empty space leaving a small amount of tensile strain in the surrounding area. Similarly, interstitials occupy space within the lattice and force the surrounding atoms closer together in a state of compressive strain. Intentionally applying a compressive or tensile strain to the material will favor the formation of defects which relieve that strain and relax the material back towards its natural lattice constant. The use of strain to modify point defect populations

has been shown to affect diffusion coefficients, and has been confirmed to work for point defect formation in InGaAs so strain may be useful here for modifying point defect formation and slowing or enhancing the Te deactivation[190–193].

Although hydrostatic pressure is the easiest type of strain to model, studies using strained films to apply strain to the sample have been successful as well[194, 195].

Silicon nitride is well known as one of the films that can impart a significant amount of strain on a wafer[196–198]. This comes in part from its coefficient of thermal expansion, which is  $3.2 \times 10^{-6} \text{ }^{\circ}\text{C}^{-1}$  compared to  $2.6 \times 10^{-6} \text{ }^{\circ}\text{C}^{-1}$  for silicon.  $\text{SiN}_x$  films are frequently deposited by Plasma Enhanced Chemical Vapor Deposition (PECVD), using gaseous precursors like silane and either ammonia or nitrogen. The samples are heated on a platen and the gasses introduced in the chamber. An RF plasma is used to react the precursors and deposit  $\text{SiN}_x$  on the samples.

The strain depends partially on the deposition temperature. However, the strain state can be further tuned depending upon the frequency of the plasma used[197, 199]. This is because the precursors in the plasma are ionized. At high frequencies, only electrons can respond to the RF signal and the ions are relatively free to diffuse and react as an ionized gas. At lower frequencies, the ions are accelerated by the electric field and actually implanted into the  $\text{SiN}_x$  layer as it is growing. These extra ions implanted into the layer act to enhance the compressive strain of the film.

Samples of the heavily Te doped material were mounted and polished from the back side to a total thickness of about 55  $\mu\text{m}$  on an Allied Multiprep polishing wheel. This was necessary because the strain from the  $\text{SiN}_x$  film needs to be transferred to the Te doped InGaAs layer in order for the InGaAs to be affected. With 725  $\mu\text{m}$  of Si on the

back of the sample, the Si would essentially clamp the strain from being transferred to the InGaAs. With 55  $\mu\text{m}$  thick samples, the strain from the  $\text{SiN}_x$  is able to bend the sample and the curvature forces the InGaAs into a strained state.

$\text{SiN}_x$  deposition was performed on a STS 310PC PECVD system at 300 °C. Three recipes were used on three different samples, one using a High Frequency (HF) plasma at 13.56 MHz, a Low Frequency (LF) at 187.5 kHz, and a Mixed Frequency (MF) recipe that alternates between the two plasma frequencies to yield a neutral strain[200]. The samples had already been capped with 15 nm of  $\text{Al}_2\text{O}_3$ , and the target  $\text{SiN}_x$  thickness for all samples was 500 nm, since layers greater than 1  $\mu\text{m}$  can induce enough strain to exceed their bond with the substrate and delaminate. Ellipsometry was used to check the  $\text{SiN}_x$  layer thicknesses, which showed 540 nm on the HF sample, 750 nm on the LF sample and 460 nm on the MF sample.

At room temperature, the surface of the HF sample was bent concave, indicating that the tensile strained  $\text{SiN}_x$  was inducing compressive strain in the InGaAs layer, which should stabilize vacancies and increase the deactivation rate. The MF sample also was slightly concave, indicating a little compressive strain in the InGaAs. The LF sample surface was convex indicating a tensile strain in the InGaAs and interstitial formation should be enhanced.

The deactivating anneals were carried out at 650 °C for 5 minutes, a time at which the previous study had observed only partial deactivation. This way if one sample was deactivating faster or slower than the others, it should be apparent. It is important to also note that with the higher coefficient of thermal expansion, all three

samples would potentially become more tensile strained during the anneal, but the difference between samples should remain apparent.

The results of the strained anneals are shown in Figure 5-16. There is no systematic shift in the activation when compared to strain state. The differences fall within the typical error for Hall Effect measurement. Because there was no difference in electrical deactivation, a more nuanced experiment with more times, temperatures, and exact strain measurements was not performed. However, this may be further evidence that deactivation occurs from Frenkel pair formation since the creation of both a vacancy and an interstitial would be relatively strain neutral compared to the formation of vacancies at the surface. In this case the marker layer may have just not been sensitive enough to an excess of interstitials.

### **Ion Implantation**

The second method of point defect population manipulation was ion implantation. A large degree of damage is imparted in semiconductors when ion implanted[201, 202]. Although the displaced atoms leave many vacancies and interstitials within the material, there are also the implanted impurities which have been added to the system. With annealing, the vacancies and interstitials recombine, but there is now a surplus of interstitials equal to the implanted dose of atoms. This is called the plus one model, and unless the matrix is amorphized or damaged so heavily that it recrystallizes, the implant dose introduces an equal number of interstitials.

Doing an implant into the heavily Te doped InGaAs would initially deactivate the damaged region of the semiconductor, but when annealed the excess interstitials should quickly diffuse throughout the layer and begin recombining with any vacancies

that form. Since Frenkel pair formation should react in equilibrium with the recombination of vacancies and interstitials, having excess interstitials should reduce the number of vacancies that form to deactivate the Te.

A Ga or In implant would introduce group III atoms and drive the Frenkel pair formation in reverse to slow the formation of group III vacancies. A second proposed reaction, although not as favorable as Frenkel pair formation, is Ga antisite defects with an As interstitial[47]. For this second reaction, excess As interstitials would slow the formation of group III vacancies. Indium is an unlikely candidate for implantation because of its large mass, which would cause more damage in the semiconductor. If Ga or As was implanted, the interstitials will not all be the dopant atoms, otherwise ion implantation would never result in any electrical activation, but with an excess of one type of interstitials, most of the interstitials remaining in the layer after recombination will be of that type.

In this experiment, Ga was unavailable, so As was implanted into the heavily Te doped and control samples at 3 keV to doses of  $2 \times 10^{14} \text{ cm}^{-2}$  and  $7 \times 10^{14} \text{ cm}^{-2}$ . The implants were performed at 100 °C so that dynamic annealing could take place to minimize damage to the InGaAs. HRTEM of the surface of an implanted sample is shown in Figure 5-17 to confirm that the samples are not amorphized. This implant energy constrained the implant to the top 20 nm of the Te doped layer, so that 80% of the layer would remain electrically active.

The results of anneals of varying time at 700 °C are shown in figure 5-18. When fit with exponential decay curves, the implanted samples had a time constant about 3.1 times as long as the unimplanted samples. This means that the excess interstitials

were able to combine with vacancies and slow the deactivation of the Te. Interestingly, the two implants seemed to have a similar effect, probably because of the high doses used and one being only 3.5 times higher dose than the other. Neither implant was able to affect the final activation values in a meaningful way, stabilizing at a dose of  $9 \times 10^{13} \text{cm}^{-2}$  rather than  $7 \times 10^{13} \text{cm}^{-2}$ . This could be a result of the excess interstitials diffusing out of the Te doped layer where they are needed.

Compared to the 2.6eV activation energy of the deactivation mechanism, the activation energy of As interstitial diffusion in InGaAs is 1.2eV[203]. This difference in activation energy means that at a lower temperature, the deactivation is occurring drastically slower, while the diffusion of excess interstitials is only slightly slower in comparison. With the relative change in speed, the deactivation of the implanted samples at lower temperature should not be as affected if the out diffusion of interstitials is really the limiting factor. Figure 5-19 shows the deactivation curves for implanted and unimplanted Te doped samples at 600°C. At this temperature, the deactivation progresses only 1.6 times slower in the implanted samples. The reduced enhancement of Te stability shows that the excess interstitials are indeed responsible for the stabilization, and losing the interstitials earlier in the deactivation process reduces the amount of stabilization.

### **Summary**

The experiments in this chapter have been focused on exploring the point defects involved in the deactivation of Te doping in InGaAs. Marker layer studies have confirmed that vacancies are not injected by the deactivation process. Strained anneal experiments showed that neither vacancies nor interstitials were drawn from the surface



to assist in deactivation. Finally, implants to introduce excess interstitials confirmed that vacancies are responsible for deactivation by slowing the deactivation process.

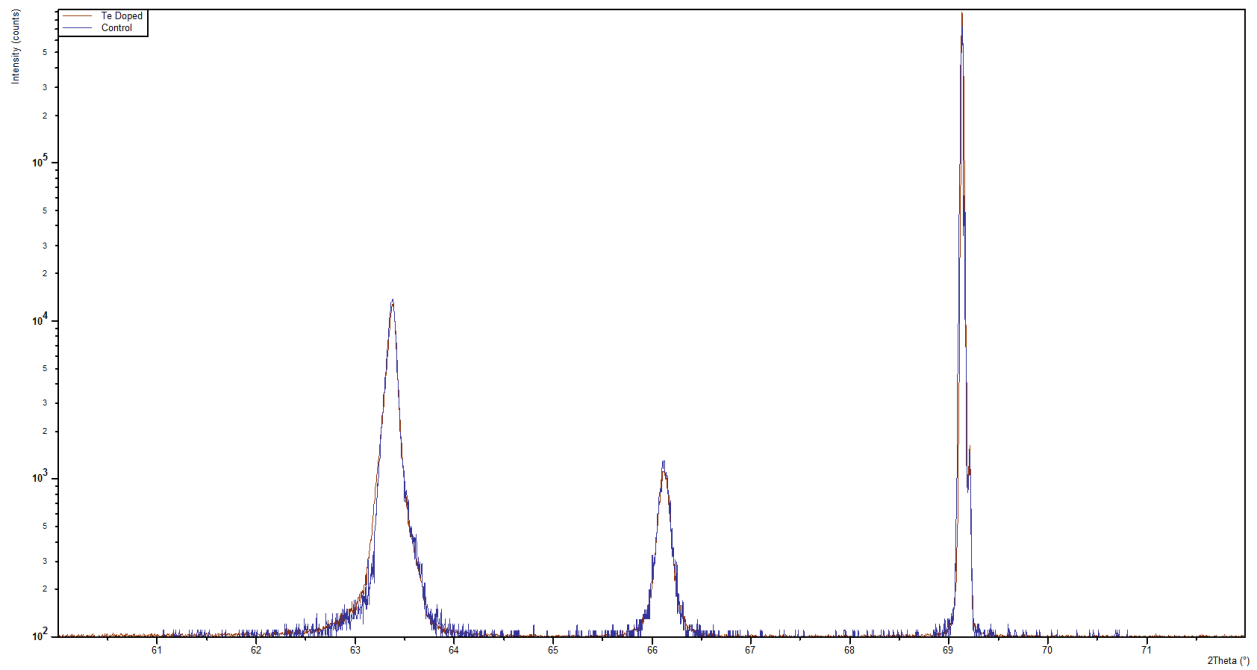


Figure 5-1. XRD scans off of the 400 plane showing a sharp Si peak on the right, GaAs peak in the center, and broad InP, InAlAs, and InGaAs peaks superimposed on the left.

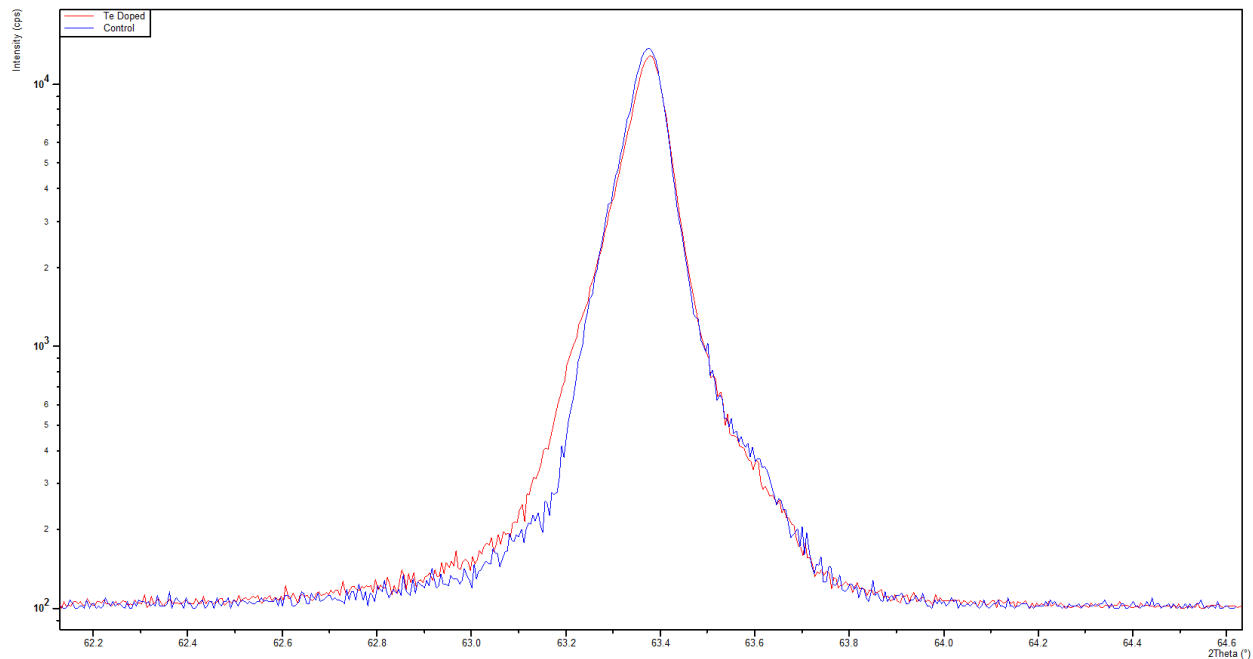


Figure 5-2. HRXRD scan around the peak for InGaAs, InAlAs, and InP. There is minimal difference between the sample with the heavily Te doped layer (red) and the control sample (blue).

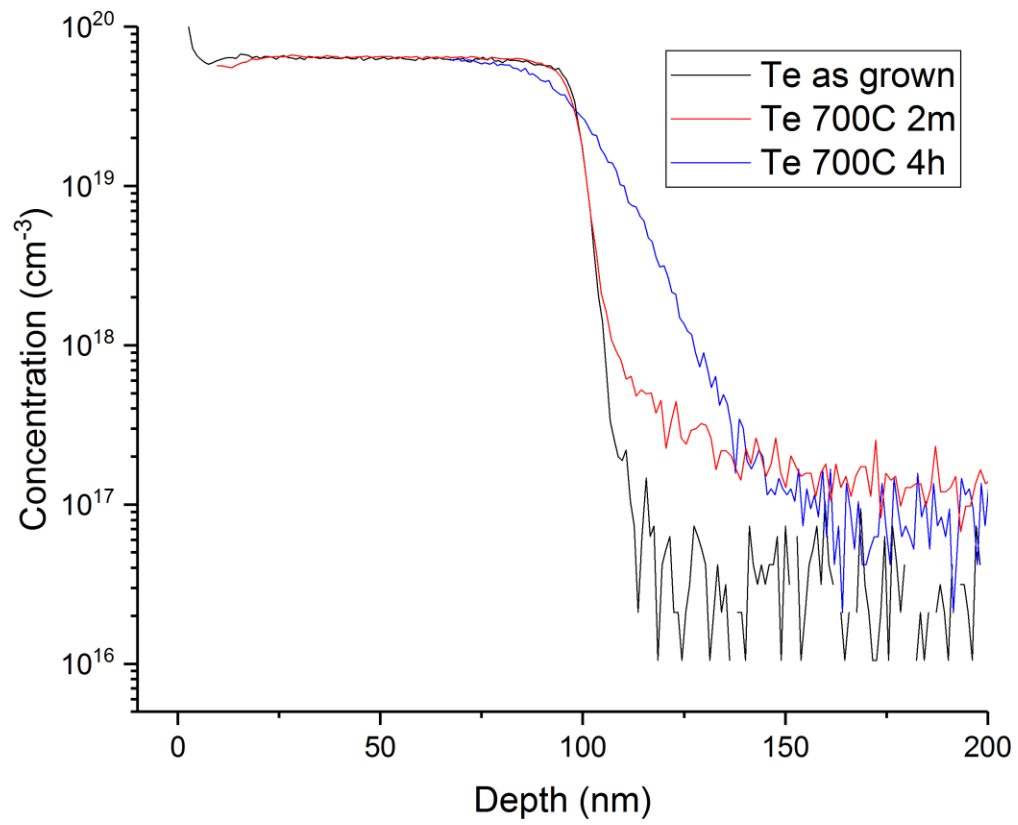


Figure 5-3. Te SIMS profiles as grown, with apparent enhanced tail diffusion after 30 seconds at 700 °C, and with Fickian diffusion after 4 hours.

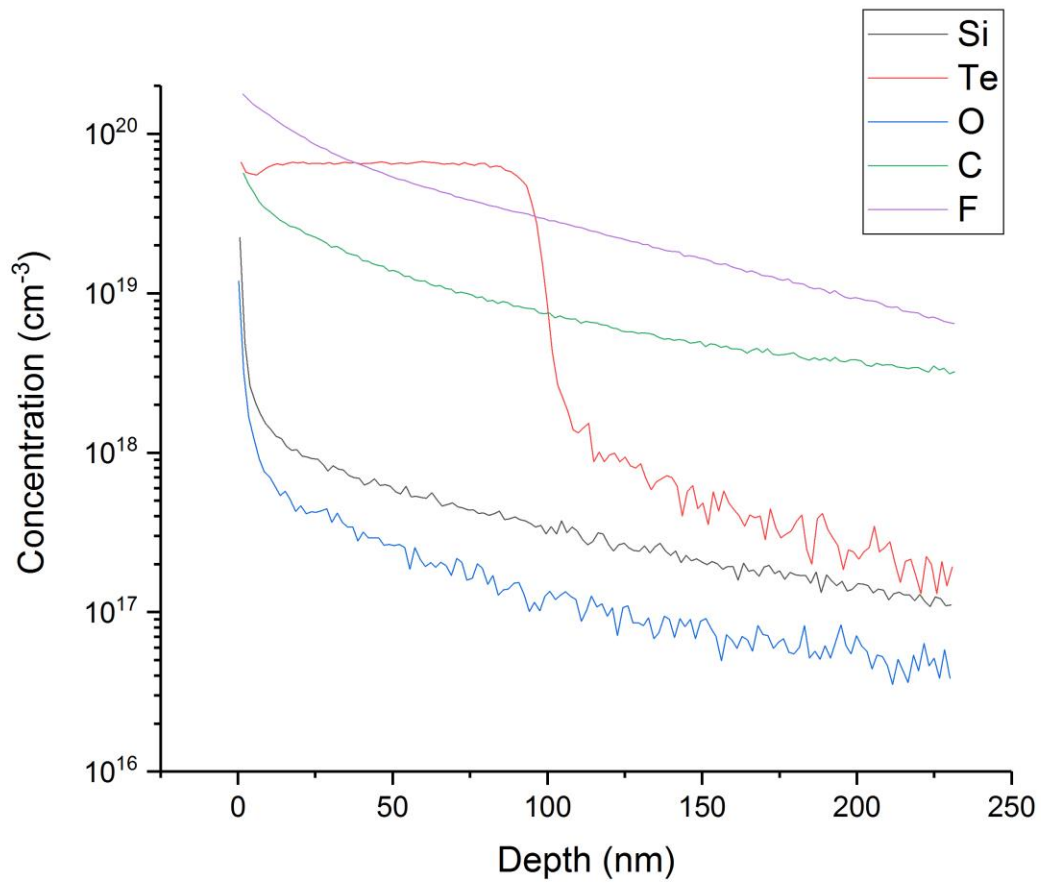


Figure 5-4. SIMS showing Te background concentration tracking fluorine contamination in the sample, while Si background tracks oxygen and carbon contamination.

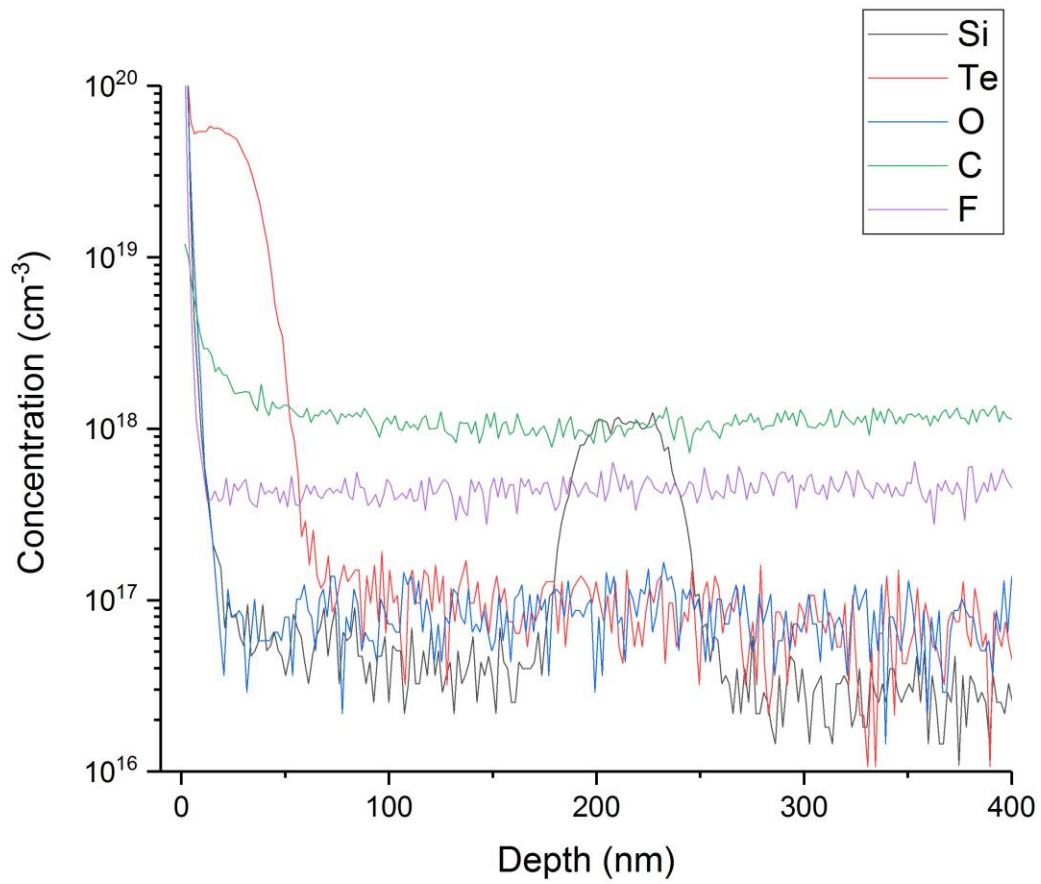


Figure 5-5. SIMS of a sample with a polished off cap showing no carbon, oxygen, or fluorine contamination, but also having very non-abrupt interfaces.

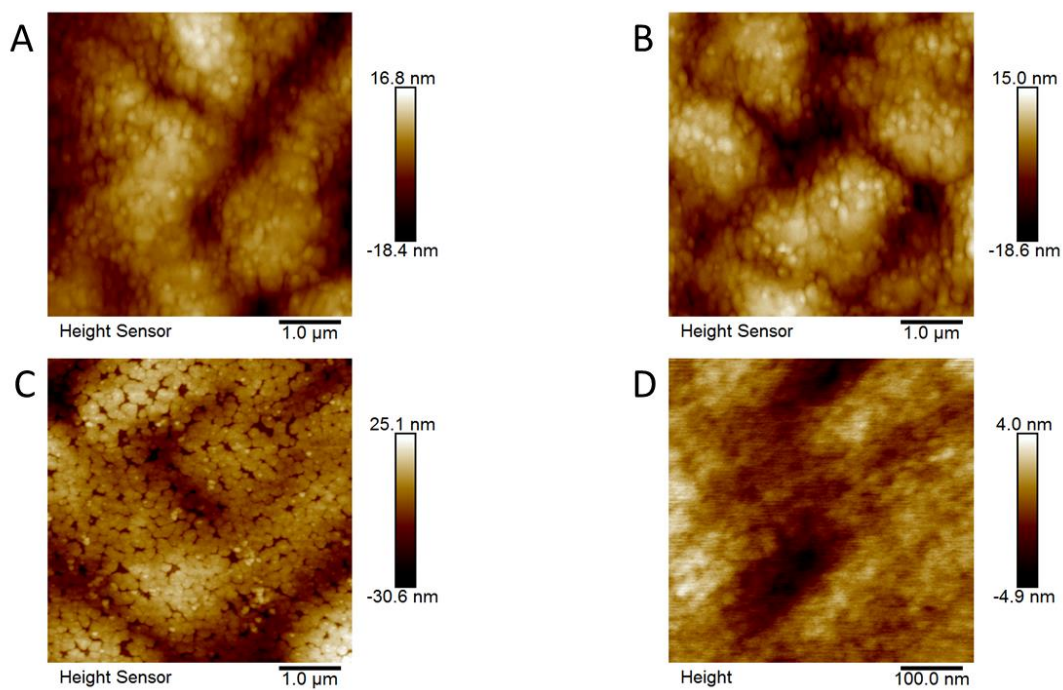


Figure 5-6. AFM images of the sample surface after various stages of capping. A) The as grown layer. B) The layer with an ALD deposited cap of 15nm  $\text{Al}_2\text{O}_3$ . C) A sample after the cap is removed with HF. D) Sample with the cap removed by polishing.

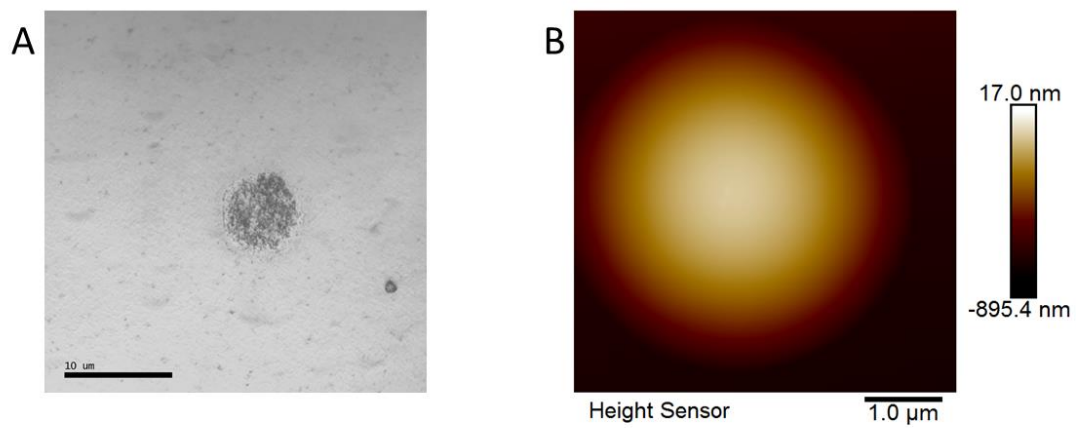


Figure 5-7. A hydrogen blister in exposure ALD deposited  $\text{Al}_2\text{O}_3$ . A) Under an optical microscope. B) Scanned by AFM.

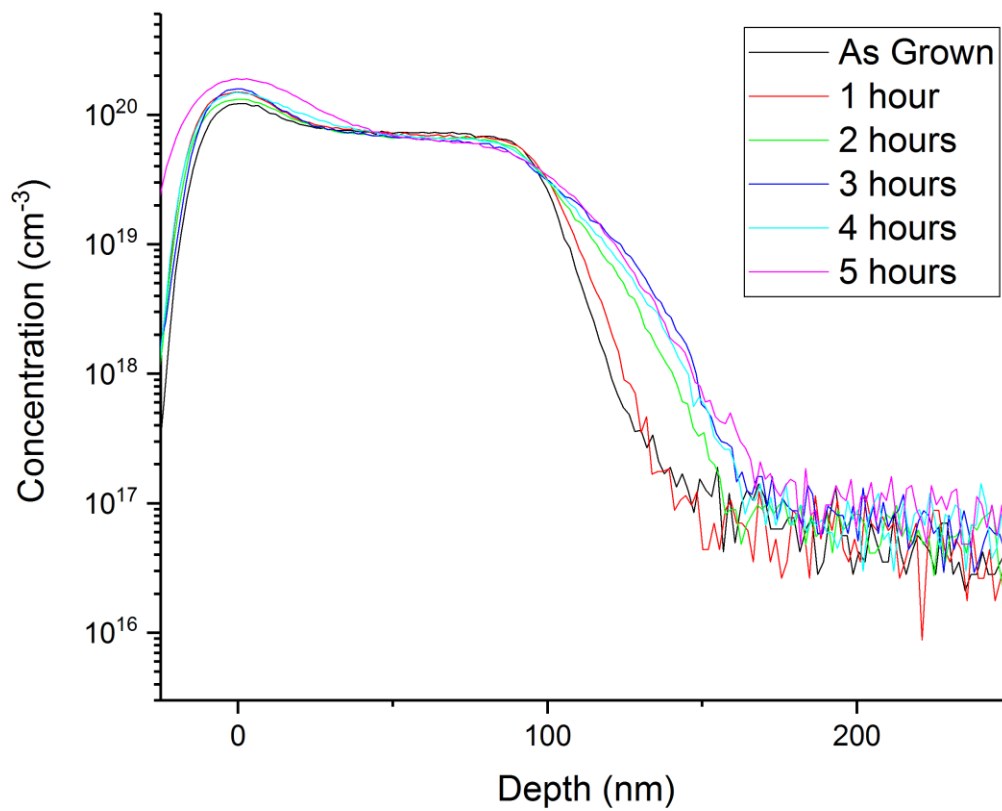


Figure 5-8. SIMS profiles of the Te layer diffusion at 700 °C showing an average diffusivity of  $3.6 \times 10^{-17} \text{ cm}^2 \text{ s}^{-1}$



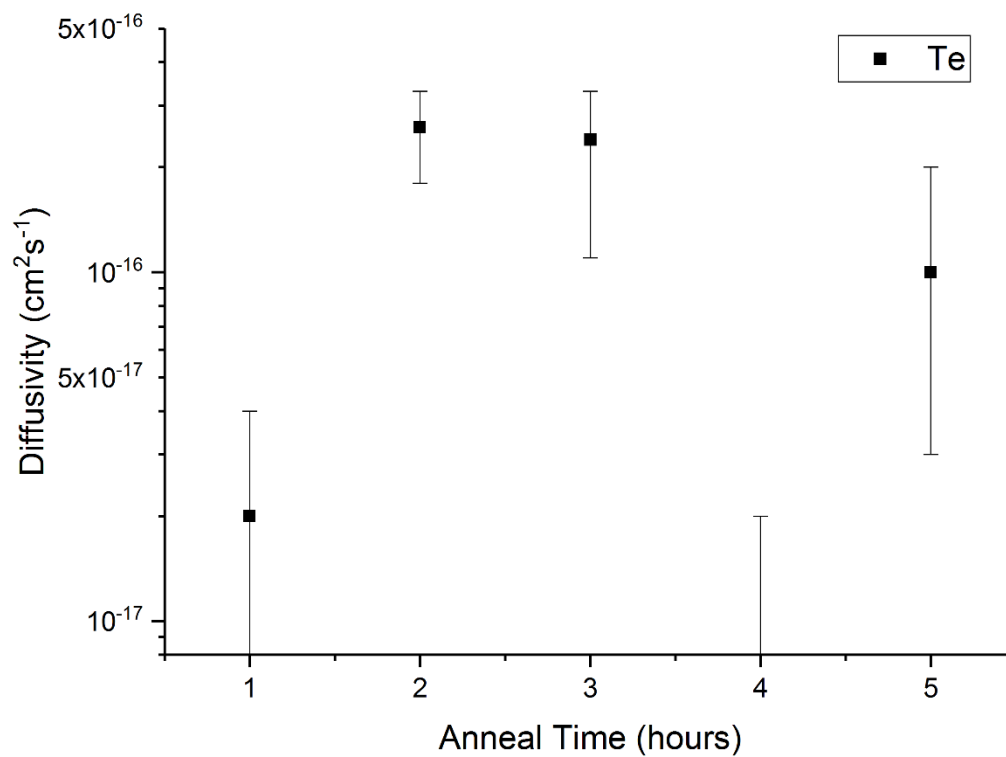


Figure 5-9. Diffusivities of Te in InGaAs extracted using FLOOPS from the SIMS profiles for 700 °C anneals.

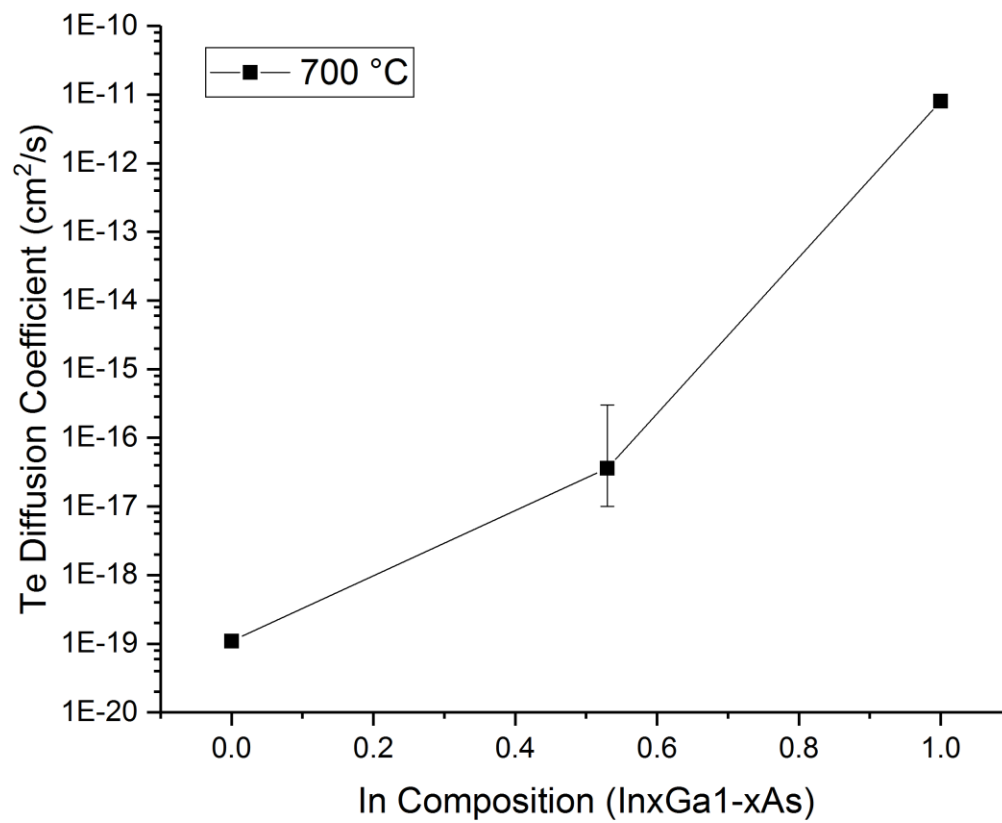


Figure 5-10. Comparison of Te diffusivity in InGaAs to values found in literature for Te diffusion in GaAs and InAs.

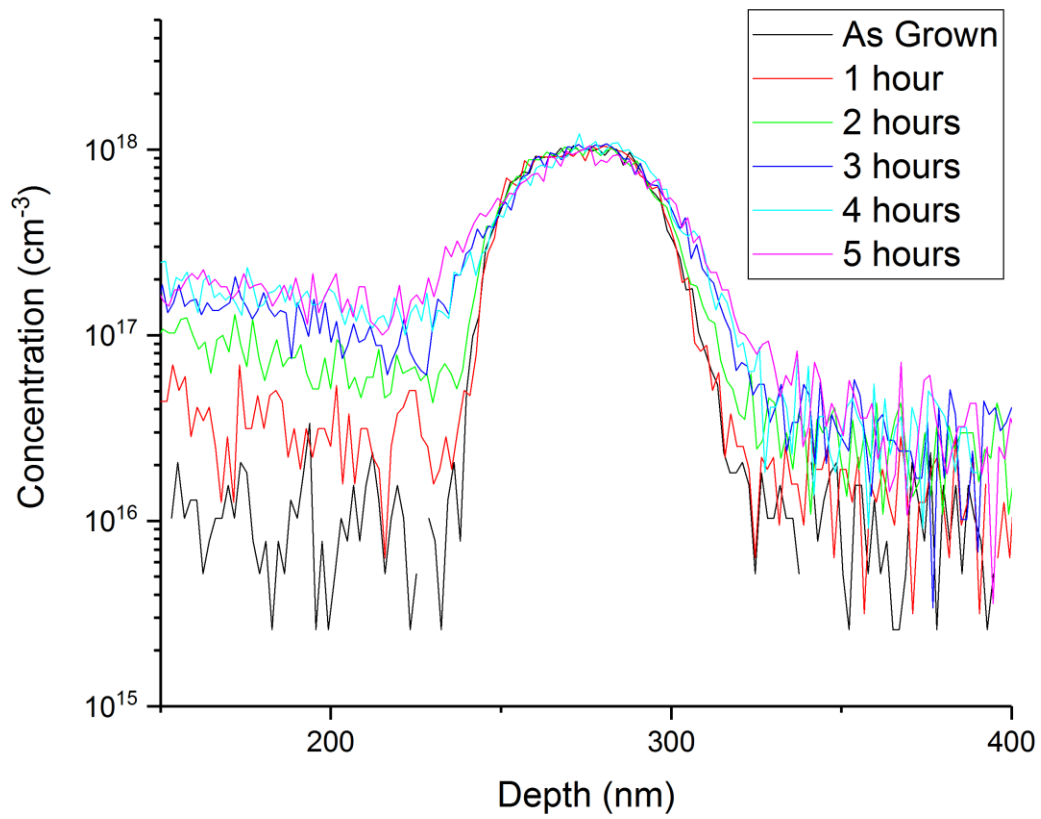


Figure 5-11. Diffusion profiles of the Si marker layer in the control sample with a diffusivity of  $6 \times 10^{-17} \text{ cm}^2 \text{ s}^{-1}$  at 700 °C.

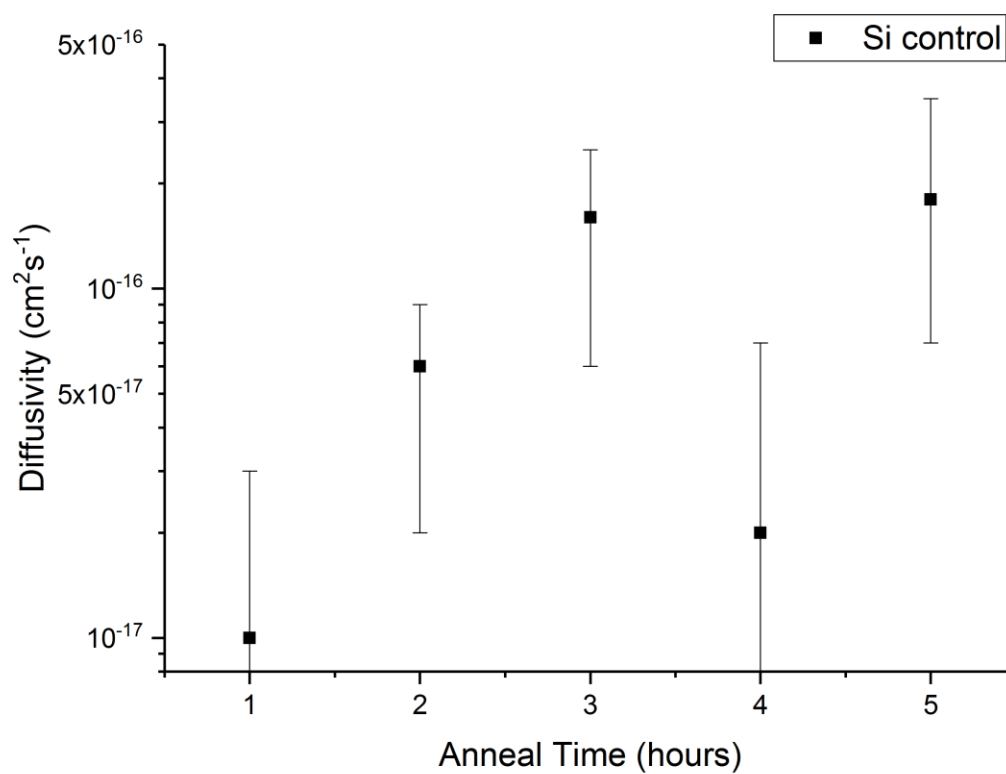


Figure 5-12. Extracted diffusivities for the Si marker layer control sample.

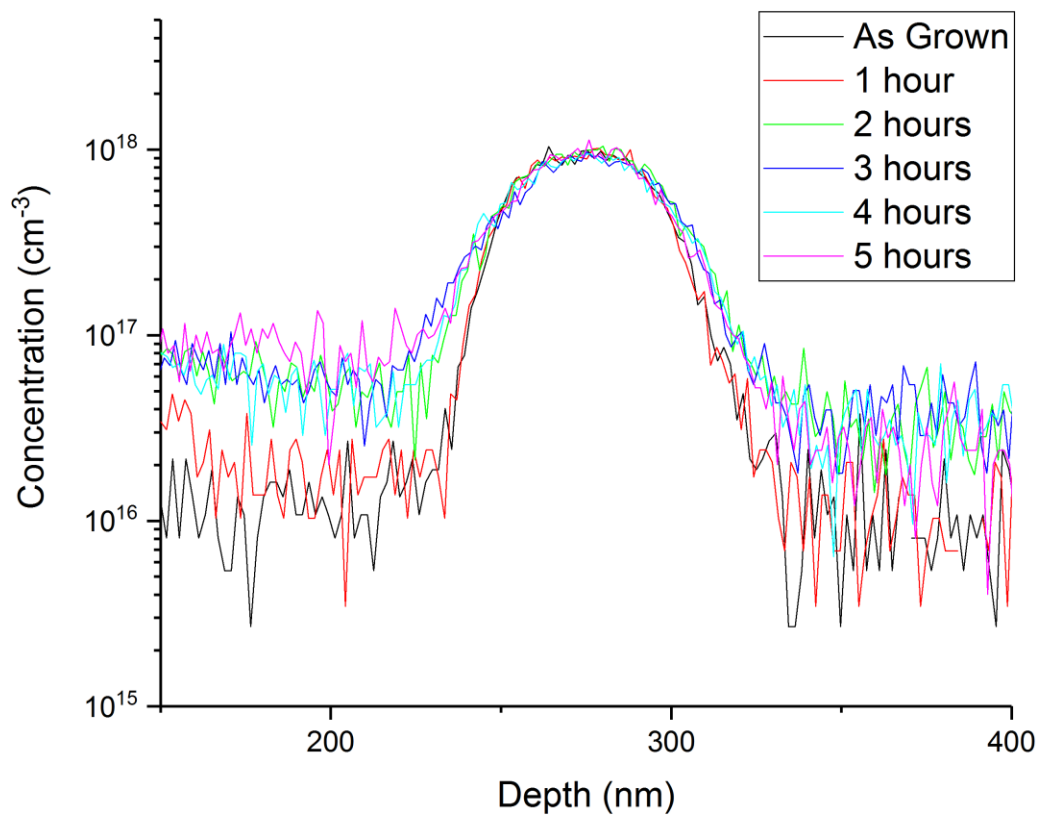


Figure 5-13. Diffusion profiles of the Si marker layer in the sample with Te exhibiting the same diffusivity as the control sample.

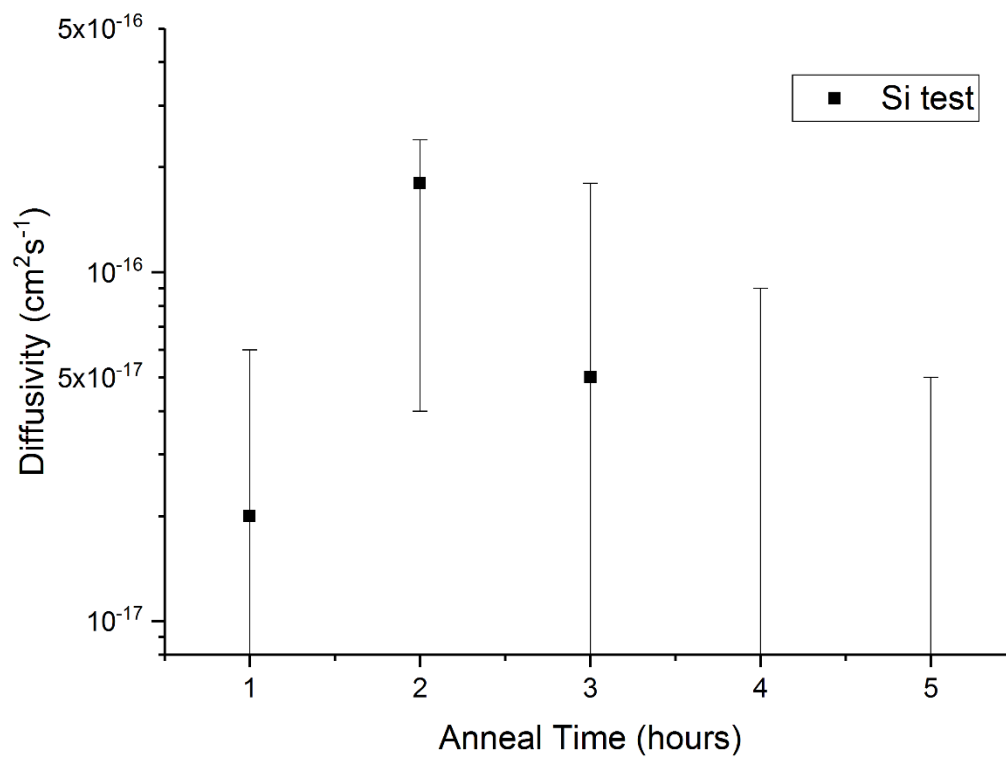


Figure 5-14. Extracted diffusivities of Si in the Te doped sample in the same range as Si diffusivities in the undoped sample.

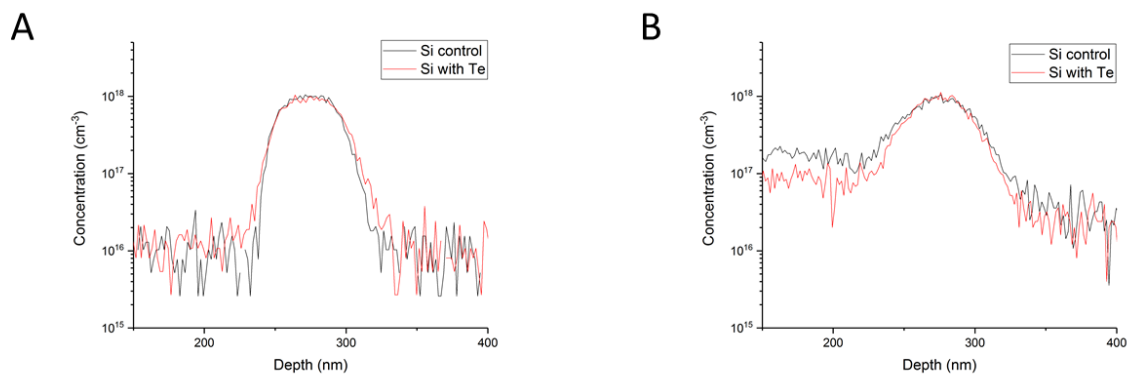


Figure 5-15. Superimposed profiles of the Si marker layers in the control (black line) and Te doped (red line) samples. A) As grown. B) After a 700 °C 5 hour anneal.

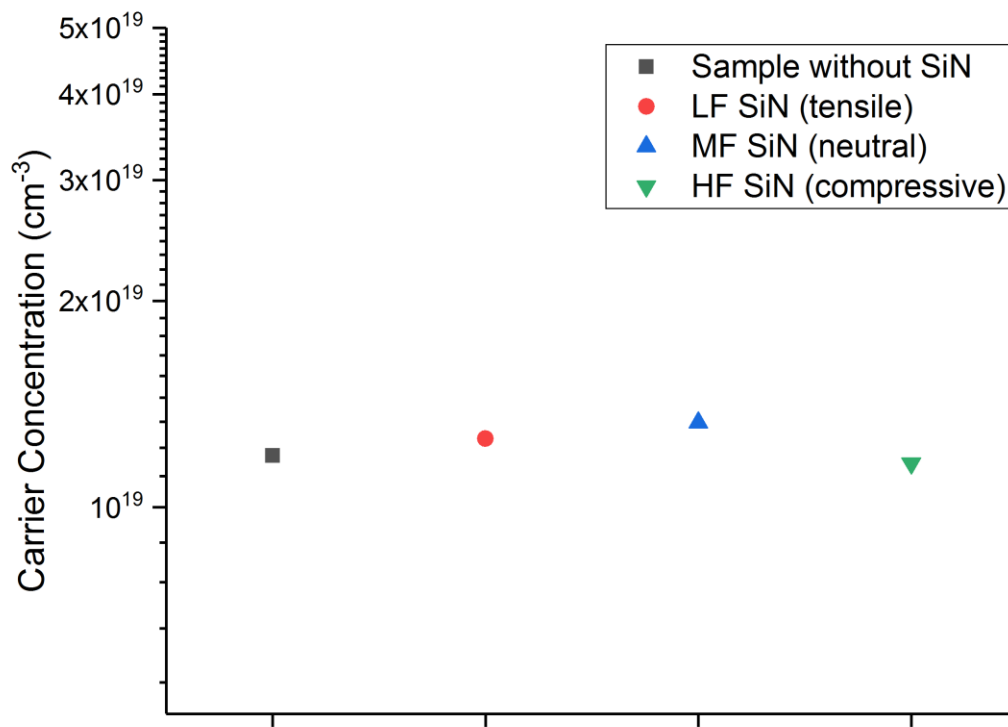


Figure 5-16. Comparison of deactivation for samples of different strain states annealed for 5 minutes at 650 °C



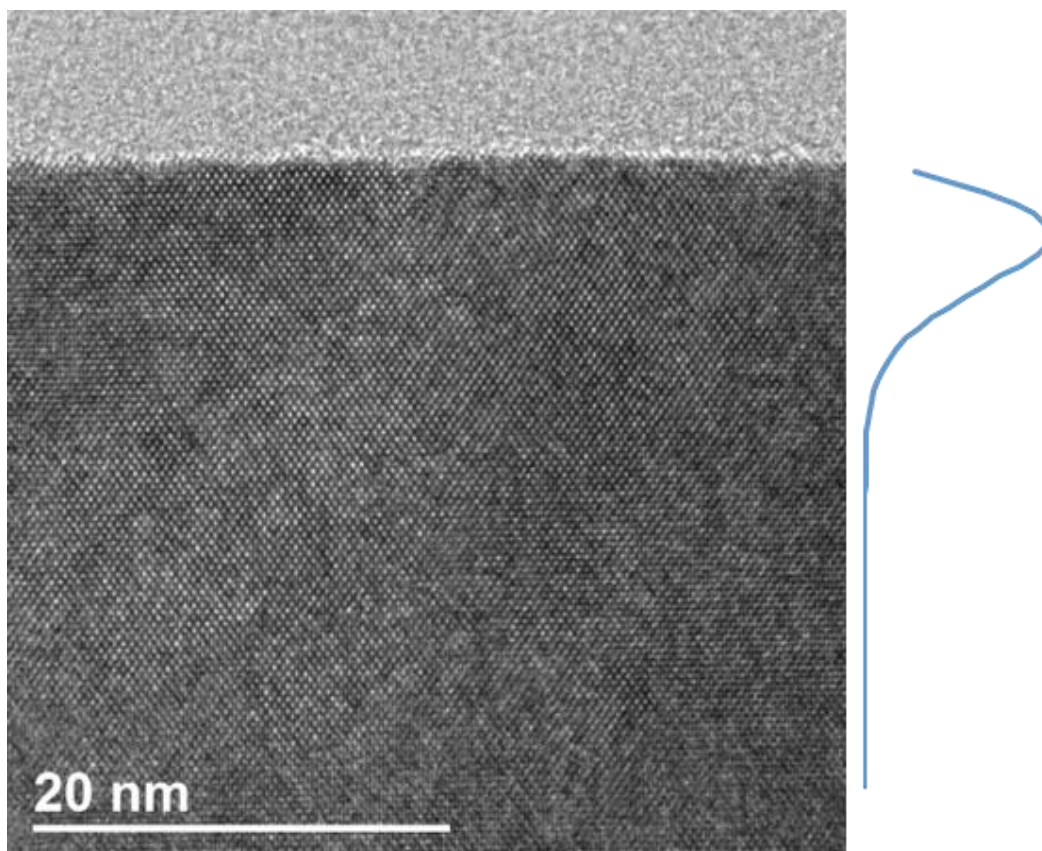


Figure 5-17. TEM of  $7 \times 10^{14} \text{ cm}^{-2}$  As implanted sample of Te doped material showing no amorphization. A schematic representation of the implant profile is shown to the right of the image.

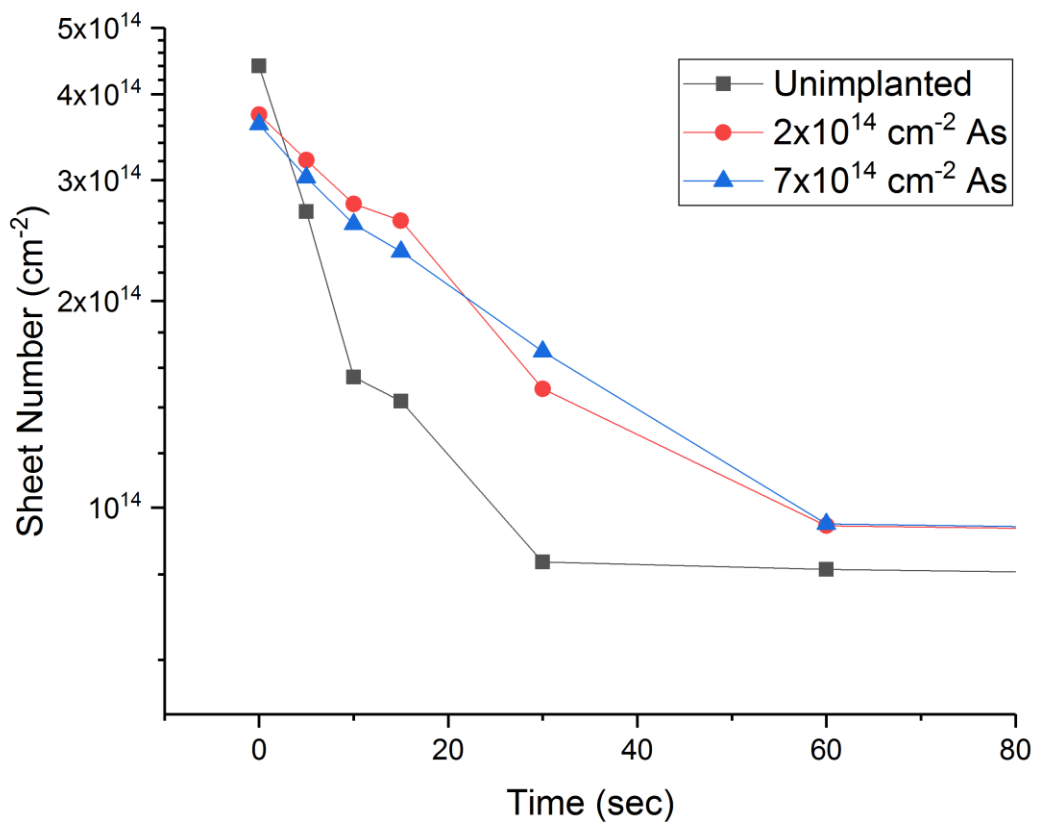


Figure 5-18. Deactivation of Te doped samples with varying As implant doses at 700 °C with a pronounced stabilization of the Te doping.

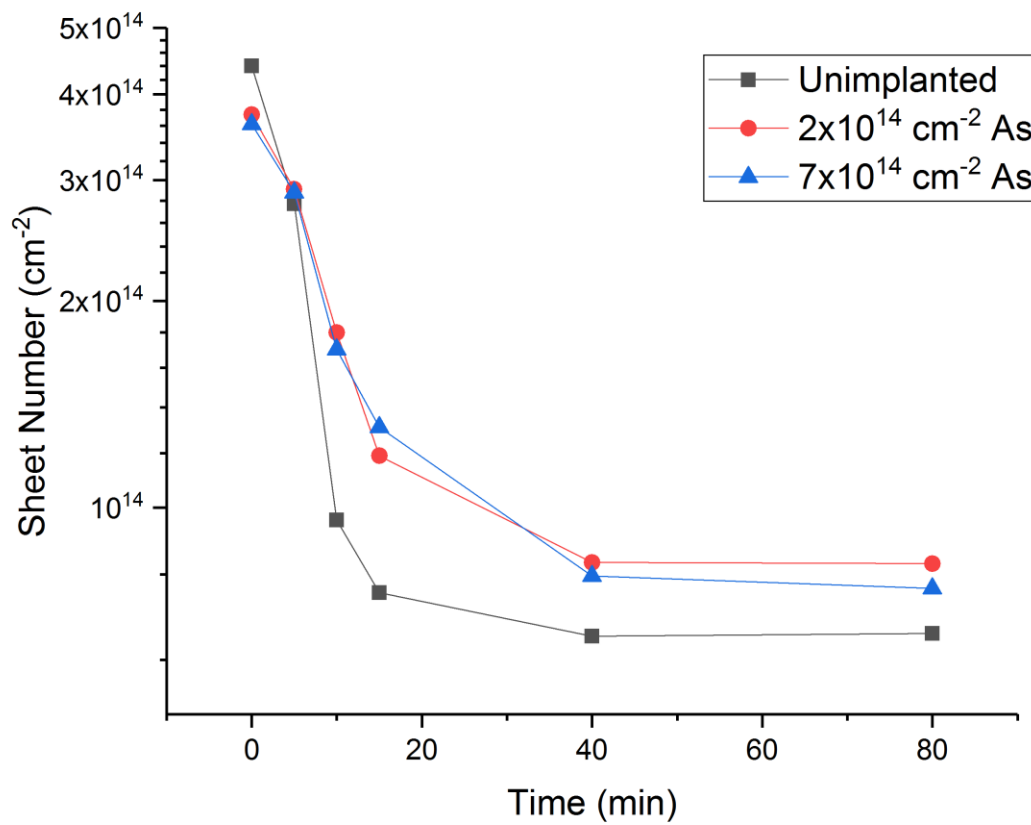


Figure 5-19. Deactivation of Te doped samples with varying As doses at 600 °C with less stabilization of the Te doping than occurred at 700 °C.

## CHAPTER 6

### AB INITIO MODELLING

Ab initio means “from the beginning” in latin, and ab initio modelling is the simulation of an atomic structure coming purely from physics. The use for this kind of modelling is usually to determine the structure or properties of a crystal that cannot otherwise be determined. This comes from a minimization of energy, with the end result being the ground state energy of a system with a certain structure, or the optimization of a structure to continue to minimize its energy[204].

These energy calculations come from electron energies within the system being modelled. This means the energies are solutions to the Schrodinger equation. For a single electron, the Schrodinger equation can be exactly solved, but in a solid material with many atoms and electrons, the interactions are too complex to mathematically solve. Several assumptions are needed to get to a solvable system.

#### **Basis of DFT**

The first of these assumptions is the Born-Oppenheimer approximation. It states that because electrons have so much less momentum than the nuclei of atoms, or ions since they are separated from their electrons, the ions are essentially stationary while solving for an electron’s wavefunction. As a result, any movement of the nuclei can be treated classically rather than quantum mechanically, greatly simplifying the equations by removing the ion-ion interactions from the equation. There are still ion-electron interactions, but being stationary and oppositely charged from the electrons, the ions can be treated as potential wells in space.

The next is a theorem by Hohenberg and Kohn which states that the ground state energy as determined by Schrodinger’s equation is equal to a unique functional of

the electron density[205]. Here a functional is the numerical answer to the bounded integral over some function that represents the electron density. A second theorem by Kohn and Sham expands upon the first by adding that the electron density which minimizes the energy of the functional is the electron density that corresponds to the solution of the Schrodinger equation[206]. These two theorems are a large part of the basis for Density Functional Theory (DFT) modelling. However, the exact function for the energy of the functional to be minimized is not exactly known.

The terms of the functional are known. There are components for the ion-ion interactions, which are just treated classically, the electron ion interactions, which can be solved treating the ions as stationary potential wells, and the electron-electron interactions, or exchange correlation energy, which does not have an exact solution and usually needs approximation.

The most basic approximation of the exchange correlation energy, and one of the most prevalent, is the Local Density Approximation (LDA). The LDA models the electron-electron interactions with the interactions of a homogeneous electron gas[207]. This can lead to systematic overbinding errors where lattice constants are too small, elastic moduli are too stiff, or bond strengths are too high, however these errors are systematic. LDA is used frequently in semiconductors, despite underestimating band gaps, because the systematic error yields good results for defect energies where the results are comparative[208, 209]. Other exchange correlations may get closer values to certain experimental techniques, but the errors in other methods cannot necessarily be predicted.

The second portion of the functional, the ion-electron interactions, the wavefunctions of the electrons are solved for the interaction with the potential wells. Core electrons fall within the well and have simple solutions, but for valence electrons the drop in potential near the core of the ion leads to excessive oscillations in the wavefunction, which takes more work to compute. To save computation time, the bottom of the potential well can be smoothed, yielding a pseudopotential for valence electrons. Because a valence electron is rarely found near the atom's core, the solutions are still accurate.

As explained further below, the exact wavefunction is not solved, but rather a superposition of plane waves combined with the periodicity of the crystal. These plane waves can be augmented with atom like orbitals to simplify the amount of computation if the core electrons need to be solved as well. In this work, the Projector Augmented Wave (PAW) method was used, which is a combination of both methods which yields higher accuracy while still only considering valence electrons[210, 211].

### **Bloch's Theorem**

To help solve the wavefunctions involved in the ion-electron interactions, Bloch's theorem states that for electrons in a perfect crystal, a set of wavefunctions can be derived so that each wavefunction is equivalent to the product of a plane wave and the periodicity of the crystal. The sum of all of these wavefunctions yields the overall wavefunction and thus the overall energy of the system. However, there are an infinite number of plane waves and symmetries that can be drawn through a crystal. Mathematically, Bloch's theorem serves to split the wavefunction being solved into a

Fourier series. The infinite series converges to the exact solution, but shortening the number of terms to something that can be computed can still yield reasonable accuracy.

## **K-points**

Half of the solution to Bloch's theorem involves the periodicity of the crystal. To calculate the points that will be used, it is easiest to work in the reciprocal space of the crystal. The first Brillouin zone is the primitive cell in reciprocal space. Because reciprocal space operates in inverse length, all of the potential periodicities of the crystal larger than the interatomic spacing fall within the Brillouin zone.

Rather than integrating over the entire Brillouin zone to get the electron density, the Bloch theorem allows for a discrete number of k-points within it to be used instead. Choosing a distribution of k-points yields a reciprocal space mesh that goes into the Fourier series to solve the wavefunction. Using more k-points or a finer reciprocal space mesh yields a more accurate electron density and thus energy for the system. Finding the k-points is done by using a perfect crystal supercell to generate the points that represent the periodicities of the system. More k-points will yield a higher accuracy to the resulting energy of the system, but takes longer to calculate. The number of k-points is increased by increasing the size of the supercell.

The increase in accuracy with increasing the number of k-points eventually offers diminishing returns, and the computation time increases with additional k-points, so it is desirable to find the minimum number of k-points that can be used to obtain an accurate result. For this work, a supercell of 4x4x4 yielded k-points that converged to less than 0.01 eV as shown in Figure 6-1. Once the k-points have been determined, the supercell used during simulations does not need to be as large as the one used to find the k-points and the symmetry beyond the supercell can be taken for granted.

## Plane Waves

The other component of solving for the wavefunctions using the Bloch theorem are the plane waves modelling the energy transport of the electrons. Similar to how the k-points for larger periodicities have small contributions to the wavefunction and can be ignored, waves with short wavelengths also have diminishing returns on the accuracy of the solution because they interfere with more atoms and have less constructive interference than the longer wavelengths. As a result a similar test for the energy cutoff, or maximum energy allowed for plane waves in the solution is used to reduce the number of plane waves in the solution and save computation time. As demonstrated in Figure 6-2, the computations reported here converged to an energy cutoff of 600 eV with a variation of less than 0.001 eV per atom.

The software package used for both the above setup and the actual DFT defect simulations that follow was the Vienna Ab initio Simulation Package (VASP)[212]. The energy determination follows a loop that starts with a 2x2x2 supercell of GaAs in a zinc blende structure with any applicable defects inserted. The initial guess of electron densities starts with the superposition of the individual atomic charge densities. The functional for this electron density distribution is solved, then a new electron density is computed using the wavefunctions that were just produced. This output electron density is then used as the input density for the next iteration. When the difference in energy between the output and input falls below a certain threshold, the system is considered to have converged and the result is given as the final output energy. The accuracy used for simulations in this work was  $10^{-4}$  eV per supercell.



## **GaAs Results**

The first simulations were for a perfect GaAs cell, then isolated defects in all of their possible configurations. Point defect positions were considered in addition to insertion, since different interstitial sites have potentially different energies associated with them. The results for the bulk elements, perfect cell and single defects is shown in Table 6-1. Lower energies correspond to more favorable atomic arrangements.

### **Single Defects**

From here, defect formation can be determined as favorable or unfavorable by adding and subtracting the supercell energies, making sure to account for all atoms on both sides of the equation. A defect formation reaction would take the energy of the resulting defects and any excess atoms removed from the cell as part of that reaction, and subtract the energy of the pure GaAs cell and any atoms that were added to the cell as part of the reaction. The formation energies of individual point defects are calculated in Table 6-2. These reactions have an energy of eV/atom instead of eV/supercell, because the majority of the supercell is not changing, and the energy difference is the result of a single atom change in the cell. Most of the defect reactions have positive energies, meaning that the reactions are unfavorable and in fact, the reverse reaction for defect dissolution would be preferred. A noticeable exception is the formation of the GaAs crystal from solid Ga and As atoms.

Energy differences of only fractions of an eV are essentially negligible, so comparing the formation energy of a Ga vacancy and an As vacancy, both are essentially equally likely to form. An excellent example of a comparison that shows substantial difference is the insertion of a Te atom. Insertion of Te on a Ga site and either interstitial sites adjacent to Ga atoms or As atoms, all have energies around 3.4

eV. However, insertion of Te on an As site, which is expected due to its doping behavior, takes only 0.91 eV. This difference is significant enough that Te can generally be assumed to sit on an As site and donate an electron the majority of the time.

With the Te insertion onto lattice sites, the first example of different energetics depending upon the reaction used to create the defect. The replacement reaction, where Te is swapped for a Ga or As atom is higher in energy than inserting the Te into a pre-existing vacancy. This is because the vacancy formation is unfavorable, so the system is starting at a higher energy before the insertion of Te. Of the sites that Te could occupy, it is apparent that  $\text{Te}_{\text{As}}$  is the preferred location, with interstitial sites and Ga sites similarly unfavorable.

### **Defect Clusters**

The methodology used to determine the clustering probability of different defects was to model two defects in the same cell with different separations. As the defects are brought closer together, different supercell energies result. The lowest of these energies indicates the preferred distance between the defects within the range of distances modeled, although all of them may be unfavorable relative to the individual defects. The first batch of defects considered were Te-Te clusters, which could involve 2 interstitial Te atoms, 1 interstitial and 1 substitutional atom, or two substitutional Te atoms resulting supercell energies are shown in Figure 6-3. The energies are plotted against defect separation, which comes from the distance between the different lattice or interstitial sites occupied. The calculated reaction energies follow in Table 6-3. Only the lowest energy defect separation was used in the calculations, in order to reduce the amount of unimportant data in the table.

The interactions of Te doping with vacancies and interstitials of the matrix species were considered next and are shown in Figure 6-4. What is interesting is that the energy is similar for  $\text{Te}_{\text{As}}\text{-V}_{\text{Ga}}$  and  $\text{Te}_{\text{Ga}}\text{-V}_{\text{As}}$ . This is in spite of Te having a strong preference for As sites when not coupled with a vacancy. This suggests that the Te atom is relaxing into the space between the Ga and As sites and not sitting on either. This would also probably prevent its extra electrons from acting as shallow donors when it is in this state. Since the  $\text{Te}_{\text{Ga}}\text{-V}_{\text{As}}$  cluster is less stable than the  $\text{Te}_{\text{As}}\text{-V}_{\text{Ga}}$  defect at larger separations, it is reasonable to say that the  $\text{Te}_{\text{Ga}}\text{-V}_{\text{As}}$  cluster has effectively relaxed into  $\text{Te}_{\text{As}}\text{-V}_{\text{Ga}}$  cluster when the Te and vacancy are adjacent. As a result, the next lowest energy for  $\text{Te}_{\text{Ga}}\text{-V}_{\text{As}}$  was used instead. Using the lowest energy separations in all other reactions, the calculated reaction energies showing Te-point defect clusters are shown in Table 6-4.

In addition to the differences in reference energy when comparing different pre-existing defects, there are some reactions that require the removal of multiple atoms. Depending upon how these reactions are calculated, such as rejecting a Ga and As atom separately, or having them regrow as GaAs elsewhere outside the cell can change the overall favorability of a reaction. As a result, it is necessary to be systematic when comparing the formation energies of different defects. In all cases where both As and Ga atoms were removed, rejecting GaAs was more favorable than separate Ga and As atoms separately, so this was the method used. Comparing these energies indicates that Te most prefers to deactivate with a Ga vacancy while resting on a substitutional site.

## Clusters of Multiple Te Atoms

Because of the favorability of  $\text{Te-V}_{\text{Ga}}$  clustering, the energies for a  $\text{Te}_2\text{-V}_{\text{Ga}}$  cluster were calculated and are shown in Figure 6-5. These will allow for calculations on the energy of a second Te atom joining an already formed cluster. Table 6-5 shows the reaction energies for two Te atoms clustering around a vacancy. These show that it is still unfavorable for two interstitials to come together, even with a vacancy to relieve the strain. Depending upon the reference energy used, such as with a pre-existing As vacancy, a substitutional and interstitial cluster formation can be favorable, although not very. The most favorable complex formation is two substitutional Te atoms with either a pre-existing Ga or As vacancy, and even the addition of a Te atom to an already formed  $\text{Te}_{\text{As}}\text{-V}_{\text{Ga}}$  cluster is favorable. Since it's unrealistic that three defects would simultaneously meet, looking at the reaction based off a  $\text{Te}_{\text{As}}\text{-V}_{\text{Ga}}$  complex already in the system gives a better idea of the energy for the second Te atom to come along and join the complex. As expected, it is slightly less favorable than the first  $\text{Te}_{\text{As}}\text{-V}_{\text{Ga}}$  complex formation.

Work up to this point covers most of the defects that could reasonably be expected to cluster with Te, but for comparison, these formation energies need to be checked with intrinsic defect cluster formation like Schottky, Frenkel and antisite defects. These supercell energies are shown in Figure 6-6. The reactions forming the intrinsic defects in their lowest energy configurations are summarized in Table 6-6. All three are unfavorable. The antisite defect used here is a reversal of Ga and As atoms, rather than one antisite atom with an excess vacancy and interstitial that would be needed for deactivation. More importantly, the Schottky and Frenkel pair formation are significantly higher energies than the 2.6eV seen experimentally for deactivation, so the

vacancies must be already present in the system in sufficient quantities for deactivation to occur. Nudged Elastic Band simulations of Ga vacancy diffusion are underway to determine if this is the limiting step in the deactivation process.

### **InAs Results**

Because the real material being studied is InGaAs, its properties are likely to fall somewhere between those of GaAs and InAs. As a result, it is necessary to perform some of the same simulations in InAs to get a rough bounds on the range of the InGaAs defect energies. The results of these reactions are shown in Table 6-7 using only the optimal defect separations as determined from GaAs, and using the perfect InAs crystal as the reference energy. As expected from In being a larger atom than Ga, Te is less likely to reside on an interstitial site than it is in GaAs. Furthermore, the energy of substitutional Te is lower than in GaAs. Te on an In site drops more in energy than Te on an As site, but  $\text{Te}_{\text{As}}$  is still the most favorable position for Te. Almost all defect cluster energies of Te in InAs were lower than in GaAs, with the noticeable exception of the  $\text{Te}_{\text{As}}\text{-V}_{\text{In}}$  cluster, which was essentially the same at 1.68eV. However, this is still the lowest energy defect pair. Clustering of two Te atoms with an In vacancy is even slightly more favorable than the  $2\text{Te}_{\text{As}}\text{-V}_{\text{Ga}}$  cluster.

### **Summary**

Overall, the energy trends were the same for GaAs and InAs, meaning that  $\text{Te}_{\text{As}}\text{-V}_{\text{III}}$  clustering is the most likely mechanism of deactivation in InGaAs. The similar energies of the two defects between GaAs and InAs mean that there is not a strong preference for vacancies of a certain element, either Ga or In, to be primarily responsible for the deactivation.

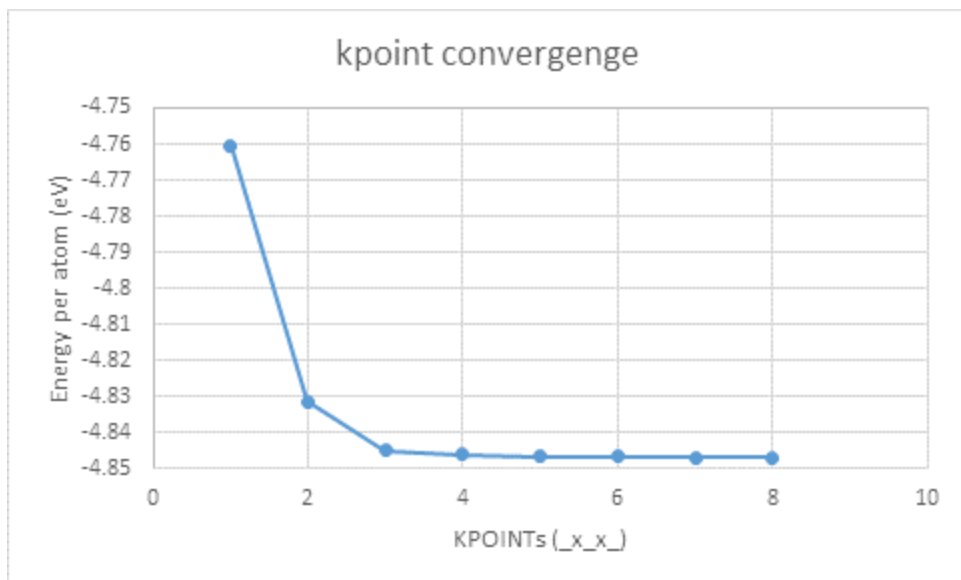


Figure 6-1. K-point convergence test with an energy change less than 0.01 eV per atom for a 4x4x4 k-point grid.

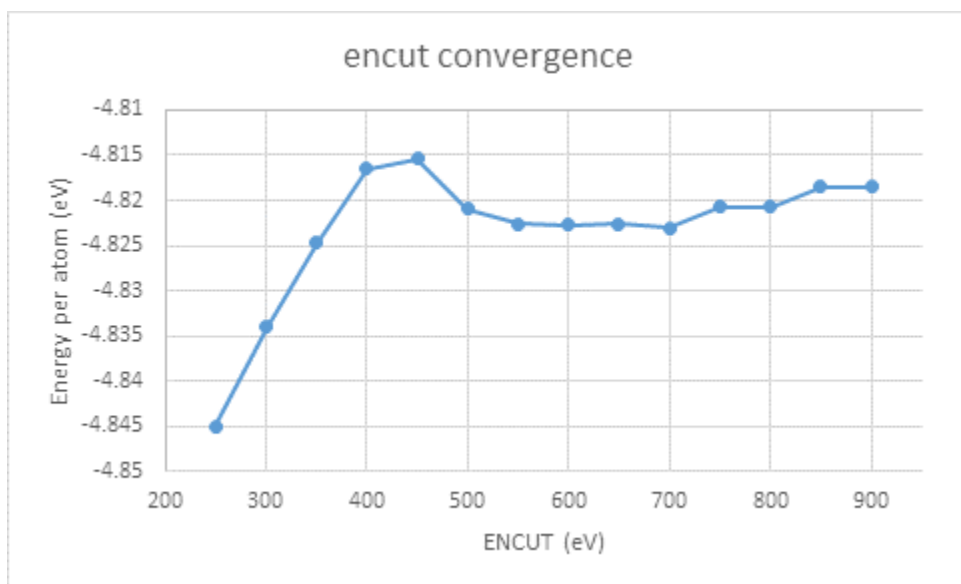


Figure 6-2. Energy cutoff convergence test with less than 0.001 eV per atom for an energy cutoff of 600 eV.

Table 6-1. Supercell energies for the elements, perfect cell and single defects.

Defect	Supercell composition	Total Energy (eV)
Ga(s)	Ga <sub>8</sub>	-28.80
As(s)	As <sub>6</sub>	-33.04
Te(s)	Te <sub>3</sub>	-11.40
Perfect unit cell	Ga <sub>32</sub> As <sub>32</sub>	-308.62
V <sub>Ga</sub>	Ga <sub>31</sub> As <sub>32</sub>	-301.97
V <sub>As</sub>	Ga <sub>32</sub> As <sub>31</sub>	-299.93
Ga <sub>TETGa-As</sub>	Ga <sub>33</sub> As <sub>32</sub>	-309.28
Ga <sub>TETGa-Ga</sub>		-309.57
Ga <sub>110-Split_Ga-As</sub>		-309.56
Ga <sub>100-Split_Ga-Ga</sub>		-308.03
As <sub>tet</sub>	Ga <sub>32</sub> As <sub>33</sub>	-310.46
As <sub>oct</sub>		-310.68
Te <sub>tet</sub> [Te-Ga]	Ga <sub>32</sub> As <sub>32</sub> Te	-308.99
Te <sub>oct</sub> [Te-As]	Ga <sub>32</sub> As <sub>32</sub> Te	-309.03
Ga <sub>As</sub>	Ga <sub>33</sub> As <sub>31</sub>	-304.78
As <sub>Ga</sub>	Ga <sub>31</sub> As <sub>33</sub>	-308.23
Te <sub>As</sub>	Ga <sub>32</sub> As <sub>31</sub> Te	-306.00
Te <sub>Ga</sub>	Ga <sub>31</sub> As <sub>32</sub> Te	-305.37

Table 6-2. Single point defect formation energies.

Defect	Reaction	Defect energy (eV/atom)
unit cell formation	$\text{Ga} + \text{As} \rightarrow \text{GaAs}$	-0.54
$V_{\text{Ga}}$	$\text{Ga}_{32}\text{As}_{32} \rightarrow \text{Ga}_{31}\text{As}_{32} + \text{Ga}$	3.06
$V_{\text{As}}$	$\text{Ga}_{32}\text{As}_{32} \rightarrow \text{Ga}_{32}\text{As}_{31} + \text{As}$	3.18
$\text{Ga}_{\text{TETGa-As}}$	$\text{Ga}_{32}\text{As}_{32} + \text{Ga} \rightarrow \text{Ga}_{33}\text{As}_{32}$	2.94
$\text{Ga}_{\text{TETGa-Ga}}$		2.65
$\text{Ga}_{110\text{-Split\_Ga-As}}$		2.67
$\text{Ga}_{100\text{-Split\_Ga-Ga}}$		4.20
$\text{As}_{\text{tet}}$	$\text{Ga}_{32}\text{As}_{32} + \text{As} \rightarrow \text{Ga}_{31}\text{As}_{33}$	3.67
$\text{As}_{\text{oct}}$		3.46
$\text{Te}_{\text{tet}} [\text{Te-Ga}]$	$\text{Ga}_{32}\text{As}_{32} + \text{Te} \rightarrow \text{Ga}_{32}\text{As}_{32}\text{Te}$	3.43
$\text{Te}_{\text{oct}} [\text{Te-As}]$		3.40
$\text{Ga}_{\text{As}}$	$\text{Ga}_{32}\text{As}_{32} + \text{Ga} \rightarrow \text{Ga}_{33}\text{As}_{31} + \text{As}$	1.93
$\text{As}_{\text{Ga}}$	$\text{Ga}_{32}\text{As}_{32} + \text{As} \rightarrow \text{Ga}_{31}\text{As}_{33} + \text{Ga}$	2.30
$\text{Te}_{\text{As}}$	$\text{Ga}_{32}\text{As}_{32} + \text{Te} \rightarrow \text{Ga}_{32}\text{As}_{31}\text{Te} + \text{As}$	0.91
	$\text{Ga}_{32}\text{As}_{31} + \text{Te} \rightarrow \text{Ga}_{32}\text{As}_{31}\text{Te}$	-2.27
$\text{Te}_{\text{Ga}}$	$\text{Ga}_{32}\text{As}_{32} + \text{Te} \rightarrow \text{Ga}_{31}\text{As}_{32}\text{Te} + \text{Ga}$	3.46
	$\text{Ga}_{31}\text{As}_{32} + \text{Te} \rightarrow \text{Ga}_{31}\text{As}_{32}\text{Te}$	0.40



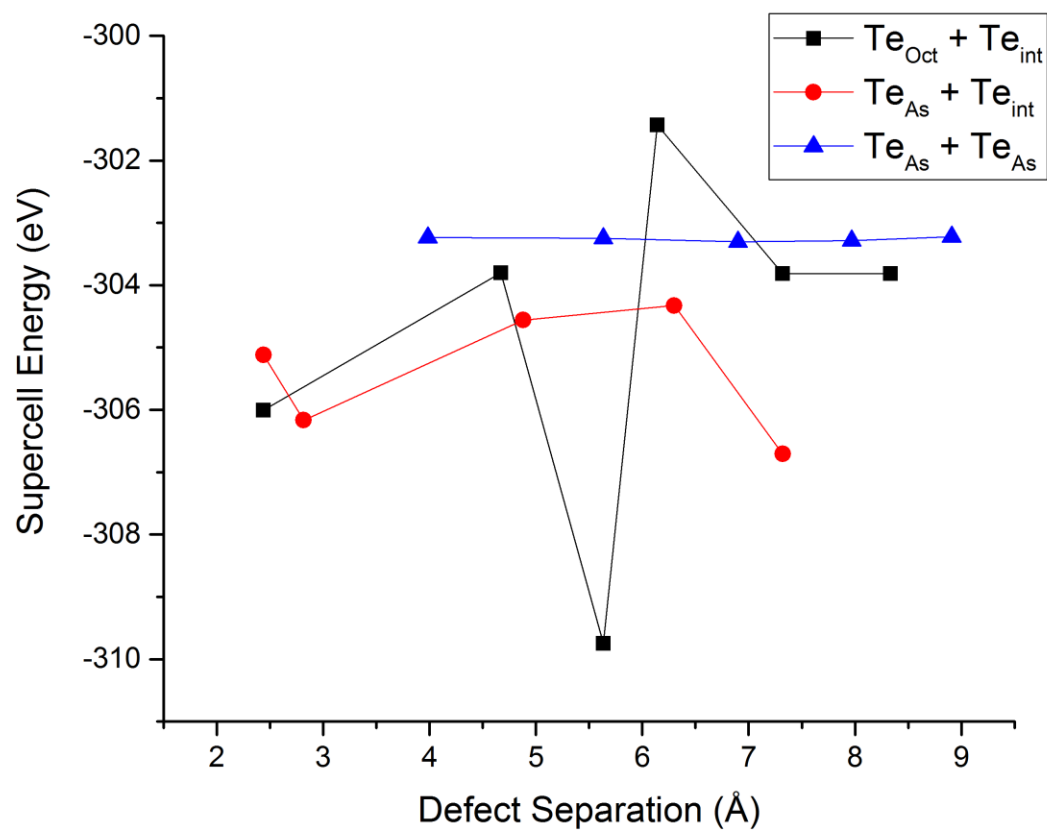


Figure 6-3. Supercell energies for Te-Te clusters.

Table 6-3. Reaction energies for Te-Te clusters.

Defect	Reaction	Defect separation (Å)	defect energy (eV/atom)
$\text{Te}_{\text{Oct}} + \text{Te}_{3\text{nn\_Oct}}$	$\text{Ga}_{32}\text{As}_{32} + 2\text{Te} \rightarrow \text{Ga}_{32}\text{As}_{32}\text{Te}_2$	5.635	6.48
$\text{Te}_{\text{As}} + \text{Te}_{2\text{nn\_Tet}}$	$\text{Ga}_{32}\text{As}_{32} + 2\text{Te} \rightarrow \text{Ga}_{32}\text{As}_{31}\text{Te}_2 + \text{As}$	2.817	4.55
	$\text{Ga}_{32}\text{As}_{31} + 2\text{Te} \rightarrow \text{Ga}_{32}\text{As}_{31}\text{Te}_2$	2.817	1.37
$\text{Te}_{\text{As}} + \text{Te}_{3\text{nn\_As}}$	$\text{Ga}_{32}\text{As}_{32} + 2\text{Te} \rightarrow \text{Ga}_{32}\text{As}_{30}\text{Te}_2 + 2\text{As}$	6.901	1.91
	$\text{Ga}_{32}\text{As}_{31}\text{Te} + \text{Te} \rightarrow \text{Ga}_{32}\text{As}_{30}\text{Te}_2 + \text{As}$	6.901	1.00

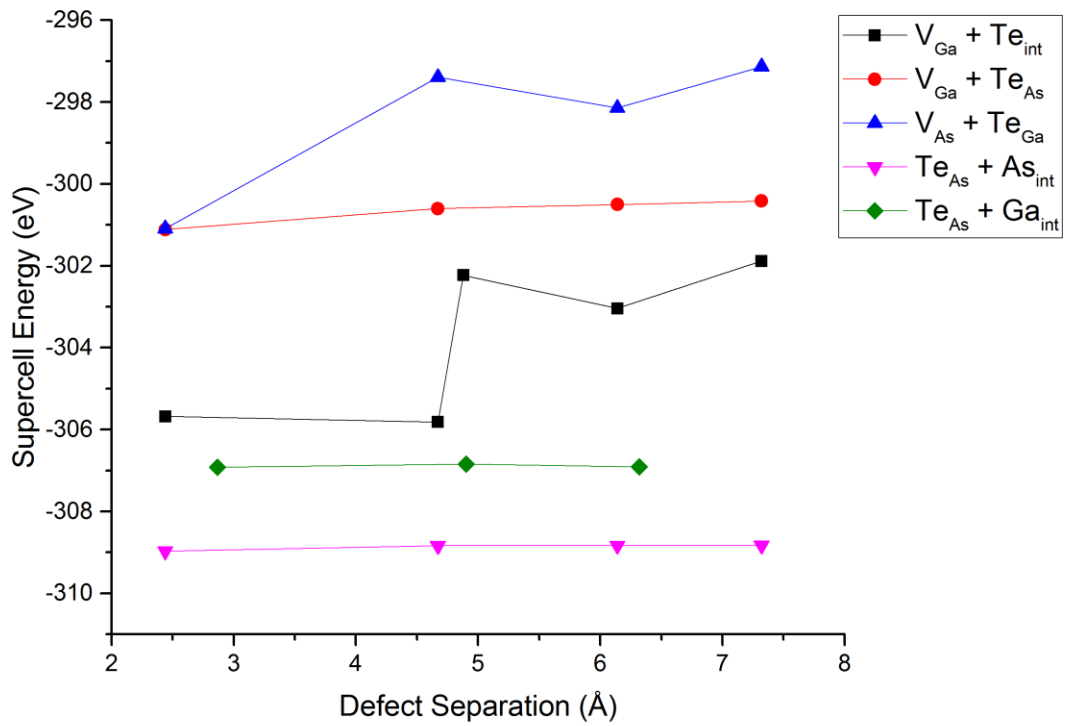


Figure 6-4. Supercell energies for Te-matrix point defect clusters

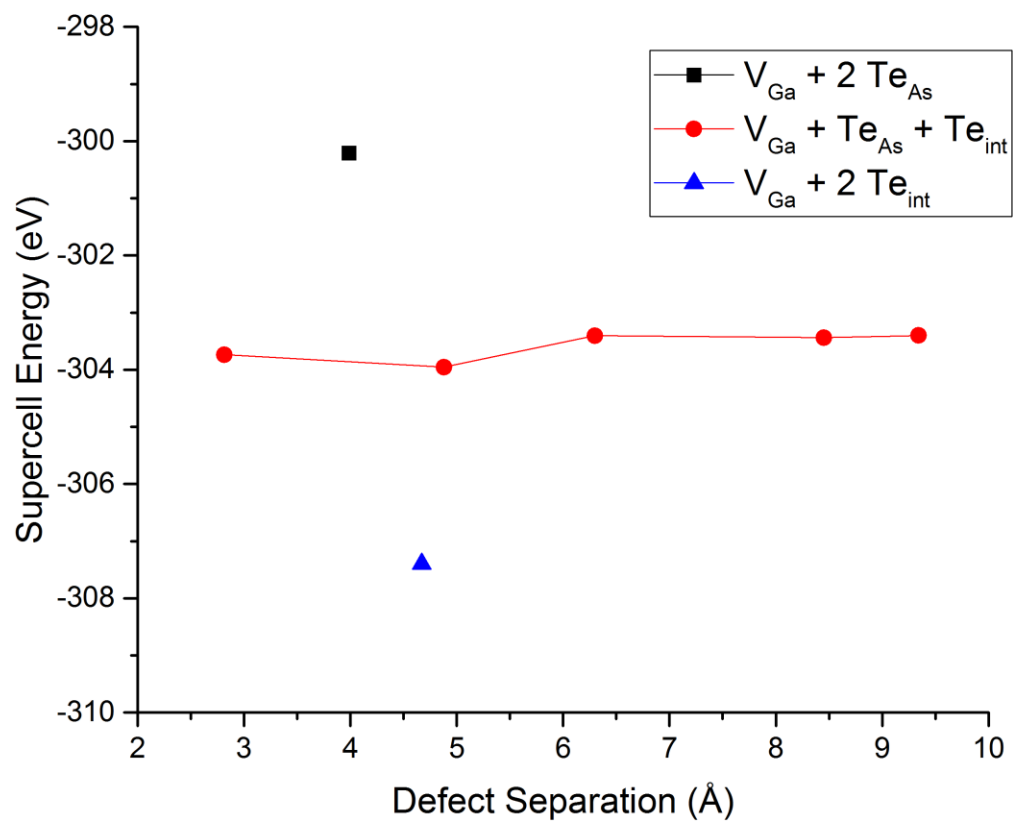


Figure 6-5. Supercell energies for two Te atoms around a Ga vacancy.

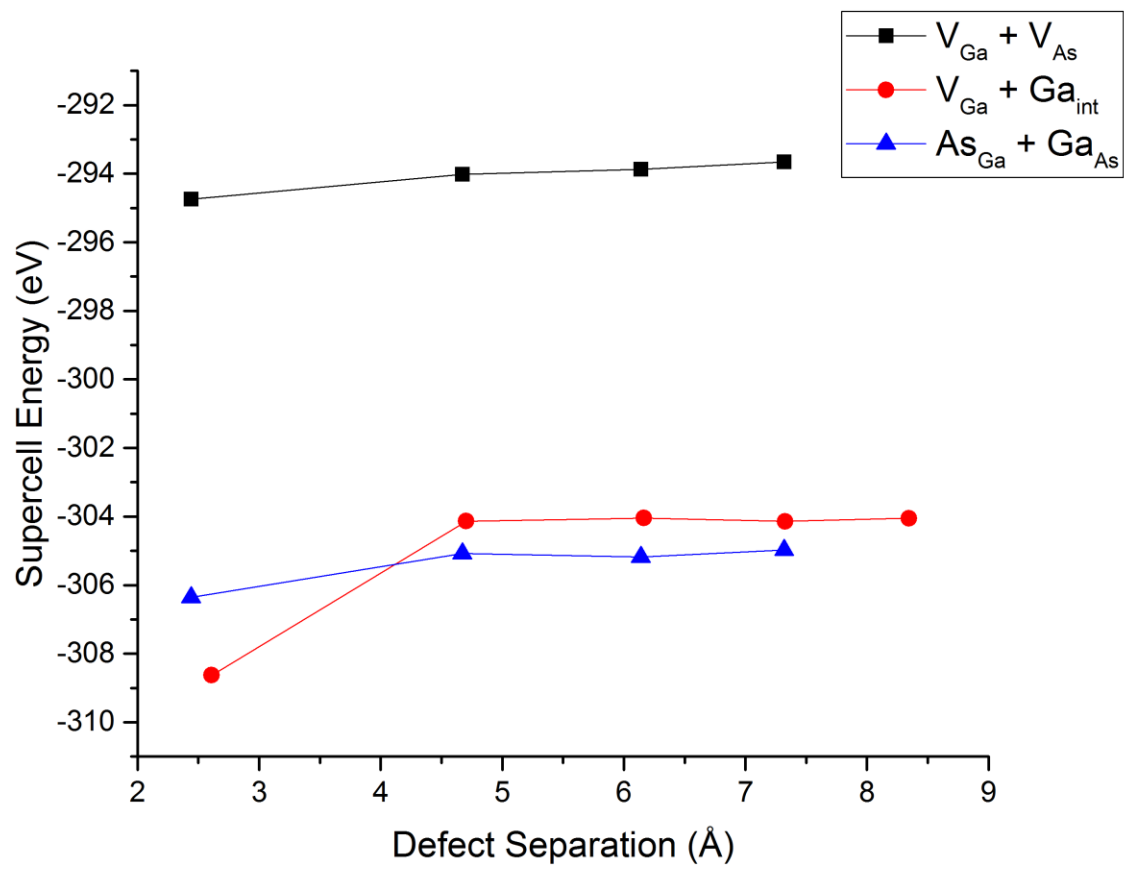


Figure 6-6. Supercell energies for intrinsic point defect clusters.

Table 6-4. Reaction energies for Te-point defect complexes.

Defect	Reaction	Defect separation (Å)	defect energy (eV/atom)
$V_{Ga} + Te_{2nn\_Tet}$	$Ga_{32}As_{32} + Te \rightarrow Ga_{31}As_{32}Te + Ga$	4.672	3.01
	$Ga_{31}As_{32} + Te \rightarrow Ga_{31}As_{32}Te$		-0.05
$V_{Ga} + Te_{1nn\_As}$	$Ga_{32}As_{32} + Te \rightarrow Ga_{31}As_{31}Te + GaAs$	2.440	1.67
	$Ga_{31}As_{32} + Te \rightarrow Ga_{31}As_{31}Te + As$		-0.86
	$Ga_{32}As_{31} + Te \rightarrow Ga_{31}As_{31}Te + Ga$		-0.98
$V_{As} + Te_{1Ga}$	$Ga_{32}As_{32} + Te \rightarrow Ga_{31}As_{31}Te + GaAs$	2.440	4.63
	$Ga_{31}As_{32} + Te \rightarrow Ga_{31}As_{31}Te + As$		2.11
	$Ga_{32}As_{31} + Te \rightarrow Ga_{31}As_{31}Te + Ga$		1.99
$Te_{As} + Ga_{1nn\_Int}$	$Ga_{32}As_{32} + Te + Ga \rightarrow Ga_{33}As_{31}Te + As$	2.868	3.60
	$Ga_{33}As_{32} + Te \rightarrow Ga_{33}As_{31}Te + As$		0.94
	$Ga_{32}As_{31}Te + Ga \rightarrow Ga_{33}As_{31}Te$		2.68
	$Ga_{33}As_{32} + Te + Ga \rightarrow Ga_{33}As_{31}Te + GaAs$		0.41
$Te_{As} + As_{1nn\_Int}$	$Ga_{32}As_{32} + Te \rightarrow Ga_{32}As_{32}Te$	2.440	3.45

Table 6-5. Reaction energies for two Te atoms clustering to a Ga vacancy.

Defect	Reaction	defect energy (eV/atom)
$2\text{Te}_{\text{As}} + \text{V}_{\text{Ga}}$	$\text{Ga}_{32}\text{As}_{32} + 2\text{Te} \rightarrow \text{Ga}_{31}\text{As}_{30}\text{Te}_2 + \text{GaAs} + \text{As}$	0.86
	$\text{Ga}_{31}\text{As}_{32} + 2\text{Te} \rightarrow \text{Ga}_{31}\text{As}_{30}\text{Te}_2 + 2\text{As}$	-1.66
	$\text{Ga}_{32}\text{As}_{31} + 2\text{Te} \rightarrow \text{Ga}_{31}\text{As}_{30}\text{Te}_2 + \text{GaAs}$	-2.32
	$\text{Ga}_{31}\text{As}_{31}\text{Te} + \text{Te} \rightarrow \text{Ga}_{31}\text{As}_{30}\text{Te}_2 + \text{As}$	-0.81
$\text{Te}_{\text{Tet\_Int}} + \text{Te}_{\text{Tet\_Int}} + \text{V}_{\text{Ga}}$	$\text{Ga}_{32}\text{As}_{32} + 2\text{Te} \rightarrow \text{Ga}_{31}\text{As}_{32}\text{Te}_2 + \text{Ga}$	5.76
	$\text{Ga}_{31}\text{As}_{32} + 2\text{Te} \rightarrow \text{Ga}_{31}\text{As}_{32}\text{Te}_2$	2.70
$\text{Te}_{\text{Tet\_Int}} + \text{Te}_{\text{Oct\_Int}} + \text{V}_{\text{Ga}}$	$\text{Ga}_{32}\text{As}_{32} + 2\text{Te} \rightarrow \text{Ga}_{31}\text{As}_{32}\text{Te}_2 + \text{Ga}$	5.23
	$\text{Ga}_{31}\text{As}_{32} + 2\text{Te} \rightarrow \text{Ga}_{31}\text{As}_{32}\text{Te}_2$	2.17
$\text{Te}_{\text{As\_2nn}} + \text{Te}_{\text{Int}} + \text{V}_{\text{Ga}}$	$\text{Ga}_{32}\text{As}_{32} + 2\text{Te} \rightarrow \text{Ga}_{31}\text{As}_{31}\text{Te}_2 + \text{GaAs}$	2.62
	$\text{Ga}_{31}\text{As}_{32} + 2\text{Te} \rightarrow \text{Ga}_{31}\text{As}_{31}\text{Te}_2 + \text{As}$	0.10
	$\text{Ga}_{32}\text{As}_{31} + 2\text{Te} \rightarrow \text{Ga}_{31}\text{As}_{31}\text{Te}_2 + \text{Ga}$	-0.02

Table 6-6. Reaction energies for multi-atom intrinsic point defect formation.

Defect	Reaction	Defect separation (Å)	Defect energy (eV/atom)
$V_{\text{Ga}} + V_{\text{As}}$	$\text{Ga}_{32}\text{As}_{32} \rightarrow \text{Ga}_{31}\text{As}_{31} + \text{GaAs}$	2.440	4.23
$\text{Ga}_{\text{INT}} + V_{\text{Ga-1nn}}$	$\text{Ga}_{32}\text{As}_{32} \rightarrow \text{Ga}_{31}\text{As}_{32} + \text{Ga}_{\text{INT}}$	2.609	4.48
$\text{As}_{\text{Ga}} + \text{Ga}_{\text{As-1nn}}$	$\text{Ga}_{\text{Ga}} + \text{As}_{\text{As}} \rightarrow \text{Ga}_{\text{As}} + \text{As}_{\text{Ga}}$	2.440	2.27

Table 6-7. InAs reaction energies.

Defect	Reaction	Defect energy (eV/atom)
unit cell formation	$\text{In} + \text{As} \rightarrow \text{InAs}$	-4.50
$V_{\text{In}}$	$\text{In}_{32}\text{As}_{32} \rightarrow \text{In}_{31}\text{As}_{32} + \text{In}$	3.02
$V_{\text{As}}$	$\text{In}_{32}\text{As}_{32} \rightarrow \text{In}_{32}\text{As}_{31} + \text{As}$	2.42
$\text{In}_{\text{As}}$	$\text{In}_{32}\text{As}_{32} + \text{In} \rightarrow \text{In}_{33}\text{As}_{31} + \text{As}$	2.04
$\text{As}_{\text{In}}$	$\text{In}_{32}\text{As}_{32} + \text{As} \rightarrow \text{In}_{31}\text{As}_{33} + \text{In}$	1.70
$\text{Te}_{\text{tet}} [\text{Te-In}]$	$\text{In}_{32}\text{As}_{32} + \text{Te} \rightarrow \text{In}_{32}\text{As}_{32}\text{Te}$	4.18
$\text{Te}_{\text{oct}} [\text{Te-As}]$		4.36
$\text{Te}_{\text{As}}$	$\text{In}_{32}\text{As}_{32} + \text{Te} \rightarrow \text{In}_{32}\text{As}_{31}\text{Te} + \text{As}$	0.39
$\text{Te}_{\text{Ga}}$	$\text{In}_{32}\text{As}_{32} + \text{Te} \rightarrow \text{In}_{31}\text{As}_{32}\text{Te} + \text{In}$	2.74
$V_{\text{In}} + \text{Te}_{1\text{nn\_As}}$	$\text{In}_{32}\text{As}_{32} + \text{Te} \rightarrow \text{In}_{31}\text{As}_{31}\text{Te} + \text{InAs}$	1.68
$\text{Te}_{\text{As}} + \text{Te}_{2\text{nn\_Tet}}$	$\text{In}_{32}\text{As}_{32} + 2\text{Te} \rightarrow \text{In}_{32}\text{As}_{31}\text{Te}_2 + \text{As}$	3.86
$\text{Te}_{\text{As}} + \text{In}_{1\text{nn\_Int}}$	$\text{In}_{32}\text{As}_{32} + \text{Te} + \text{In} \rightarrow \text{In}_{33}\text{As}_{31}\text{Te} + \text{As}$	2.73
$\text{Te}_{\text{As}} + \text{As}_{1\text{nn\_Int}}$	$\text{In}_{32}\text{As}_{32} + \text{Te} \rightarrow \text{In}_{32}\text{As}_{32}\text{Te}$	3.20
$2\text{Te}_{\text{As}} + V_{\text{In}}$	$\text{In}_{32}\text{As}_{32} + 2\text{Te} \rightarrow \text{In}_{31}\text{As}_{30}\text{Te}_2 + \text{InAs} + \text{As}$	0.54



## CHAPTER 7 CONCLUSIONS

The prevalence of modern electronics is a testament to their utility and necessity. Increases in complexity have enabled exponential growth, and in order to continue progress in this field, power consumption is the limiting factor that needs to be overcome. III-V materials and InGaAs in particular have the potential to replace silicon in the near term and in the future with lower power consumption devices. High contact resistivities are one of the plagues of III-V materials, and although solutions to this issue are known, none of them are manufacturable on a scale that lends itself to III-V integration in future electronics. Tellurium doping in InGaAs has had been incorporated by industry acceptable methods in the necessary concentrations for low contact resistivities. However, the behavior of Te in InGaAs was relatively unknown.

This work sought to illuminate the nature of Te doping in InGaAs. Initial anneals of the heavily Te doped InGaAs showed that the Te was grown in at a supersaturated electrical activation. The change in electron mobility during deactivation suggested that a new defect was forming in the deactivation process. Although the Te doping was not stable at its initial concentration, additional anneals determined an activation energy of 2.6 eV for the deactivation process, which allows for the determination of a process window for any subsequent heat treatments should Te doping in InGaAs be adopted.

Based on prior reports of Te precipitation in similar materials like GaAs, TEM examination of the deactivated layers was performed. No precipitates of Te or intermetallic alloys were observed. However, defects or clusters of atoms below the detection limits of the TEM could still have formed and be responsible for the deactivation.

Although the literature for Te precipitation appeared to not apply to Te doping in InGaAs, they also proposed clustering of Te with interstitials before complete precipitation. Another widely reported deactivation mechanism for n-type dopants in GaAs is the Ga vacancy. A silicon marker layer grown in under a heavily doped Te layer was used to look for the injection of excess point defects as a result of point defect reactions in the deactivating layer. Silicon is a vacancy diffuser in InGaAs, meaning that an excess of vacancies would enhance the Si diffusion, and an excess of interstitials would slow the diffusion. The Si diffusion was too slow to rule out interstitial injection by the capture of vacancies in the deactivating layer, but there was clearly no enhancement of the diffusion. This indicates that there are not additional interstitials participating in the deactivation of Te.

In case any point defects from the marker layer study were diffusing to the surface and recombining rather than diffusing down into the material, strained layers were placed on the InGaAs to preferentially form additional vacancies or interstitials. Samples with the InGaAs in tensile strain should try to relieve that strain with interstitials and samples under compressive strain should relieve the strain with vacancies. Across tensile, neutral, and compressively strained samples, all deactivated at the same rate. This eliminates the possibility of the surface acting as a source or sink of point defects, since they should have formed or combined more easily under strain. However, Frenkel pair formation would be fairly strain neutral so the formation of group III vacancies from Frenkel pairs or antisite formation are still possibilities.

In the final experimental technique, the heavily Te doped InGaAs layer was implanted with As ions. According to the plus one model, this shallow implant left an

excess of interstitials near the surface of the Te doped layer. The increase in the interstitial population should slow the formation of vacancies from Frenkel pairs. Deactivation initially progressed at a slower rate, however the samples deactivated to the same stable level as unimplanted material. With a high interstitial diffusivity, the interstitial concentration quickly drops several orders of magnitude and loses its effect. This supports the idea that Te deactivation is occurring with generated vacancies, since excess interstitials are able to slow the progression of deactivation.

DFT simulations based on GaAs and InAs were able to confirm most of these experimental results. Te clustering is unfavorable, as are spontaneously generated vacancies of either the group III element or As. Te prefers sitting on an As site when incorporated in the crystal, and reacts most readily with a group III vacancy. The formation energies of vacancies from Schottky and Frenkel defects are higher than the experimental energy determined for deactivation and thus cannot be the limiting step in deactivation. As a result, it is proposed that the vacancies are already present in the InGaAs before deactivation and that cluster formation or vacancy diffusion is likely the limiting step.

## LIST OF REFERENCES

1. Moore GE (1965) Cramming more components onto integrated circuits. *Electronics* 38:114–117.
2. Barrett CR (1993) Microprocessor evolution and technology impact. In: Symp. 1993 VLSI Technol. pp 7–10
3. Schulz M (1999) The end of the road for silicon? *Nature* 399:729–730. doi: 10.1038/21526
4. Lundstrom M (2003) Moore's Law Forever? *Science* 299:210–211. doi: 10.1126/science.1079567
5. Shalf JM, Leland R (2015) Computing beyond Moore's Law. *Computer* 48:14–23. doi: 10.1109/MC.2015.374
6. Lin BJ (2005) Lithography for manufacturing of sub-65nm nodes and beyond. In: IEEE Int. Devices Meet. 2005 IEDM Tech. Dig. pp 48–51
7. Bencher C, Chen Y, Dai H, et al (2008) 22nm half-pitch patterning by CVD spacer self alignment double patterning (SADP). p 69244E
8. Thompson SE, Chau RS, Ghani T, et al (2005) In search of "Forever," continued transistor scaling one new material at a time. *IEEE Trans Semicond Manuf* 18:26–36. doi: 10.1109/TSM.2004.841816
9. McKelvey JP (1993) *Solid State Physics for Engineering and Materials Science*, Original ed edition. Krieger Pub Co, Malabar, Fla
10. Kasap S (2005) *Principles of Electronic Materials and Devices*, 3 edition. McGraw-Hill Education, Boston etc.
11. Hummel RE (2013) *Electronic Properties of Materials*, 4th ed. 2011, Corr. 3rd printing 2013 edition. Springer, New York
12. Pichler P (2012) *Intrinsic Point Defects, Impurities, and Their Diffusion in Silicon*, Softcover reprint of the original 1st ed. 2004 edition. Springer, New York
13. Van Wieringen A, Warmoltz N (1956) On the permeation of hydrogen and helium in single crystal silicon and germanium at elevated temperatures. *Physica* 22:849–865. doi: 10.1016/S0031-8914(56)90039-8
14. Pearton SJ, Dautremont-Smith WC, Lopata J, et al (1987) Dopant-type effects on the diffusion of deuterium in GaAs. *Phys Rev B* 36:4260–4264. doi: 10.1103/PhysRevB.36.4260

15. Hara A (2007) Diffusion Coefficient of Hydrogen in Silicon at an Intermediate Temperature. *Jpn J Appl Phys* 46:962. doi: 10.1143/JJAP.46.962
16. Chevallier J, Dautremont-Smith WC, Tu CW, Pearton SJ (1985) Donor neutralization in GaAs(Si) by atomic hydrogen. *Appl Phys Lett* 47:108–110. doi: 10.1063/1.96284
17. Briddon PR, Jones R (1990) Ab initio calculations on the passivation of shallow impurities in GaAs. *Phys Rev Lett* 64:2535–2538. doi: 10.1103/PhysRevLett.64.2535
18. Van de Walle CG, Neugebauer J (2003) Universal alignment of hydrogen levels in semiconductors, insulators and solutions. *Nature* 423:626–628. doi: 10.1038/nature01665
19. Timp G, Bude J, Bourdelle KK, et al (1999) The ballistic nano-transistor. In: *Electron Devices Meet. 1999 IEDM99 Tech. Dig. Int. IEEE*, pp 55–58
20. Lundstrom M, Ren Z (2002) Essential physics of carrier transport in nanoscale MOSFETs. *IEEE Trans Electron Devices* 49:133–141. doi: 10.1109/16.974760
21. del Alamo JA (2011) Nanometre-scale electronics with III-V compound semiconductors. *Nature* 479:317–323. doi: 10.1038/nature10677
22. Stringfellow GB (1989) *Organometallic Vapor-Phase Epitaxy: Theory and Practice*, First Edition edition. Academic Press, Boston
23. Oktyabrsky S, Ye PD (2010) *Fundamentals of III-V Semiconductor MOSFETs*. Springer
24. Turkane SM, Kureshi AK (2016) Review of Tunnel Field Effect Transistor (TFET). *Int J Appl Eng Res* 11:4922–4929.
25. Kumar CP, Sivani K (2016) Analyzing the impact of TFETs for ultra-low power design applications. In: *2016 Int. Conf. Electr. Electron. Optim. Tech. ICEEOT*. pp 608–612
26. Alian A, Mols Y, Bordallo CCM, et al (2016) InGaAs tunnel FET with sub-nanometer EOT and sub-60 mV/dec sub-threshold swing at room temperature. *Appl Phys Lett* 109:243502. doi: 10.1063/1.4971830
27. Lin J, Cai X, Antoniadis D, Alamo JA del (2017) The Importance of Ballistic Resistance in the Modeling of Nanoscale InGaAs MOSFETs. *IEEE Electron Device Lett* PP:1–1. doi: 10.1109/LED.2017.2700385
28. 2013 ITRS. In: *Int. Technol. Roadmap Semicond.* <http://www.itrs2.net/2013-itrs.html>. Accessed 23 Feb 2015

29. Neamen D (2005) *An Introduction to Semiconductor Devices*. McGraw-Hill Science/Engineering/Math, Boston
30. Piotrowska A, Guivarc'h A, Pelous G (1983) Ohmic contacts to III–V compound semiconductors: A review of fabrication techniques. *Solid-State Electron* 26:179–197. doi: 10.1016/0038-1101(83)90083-7
31. Baraskar A, Gossard AC, Rodwell MJW (2013) Lower limits to metal-semiconductor contact resistance: Theoretical models and experimental data. *J Appl Phys* 114:154516. doi: 10.1063/1.4826205
32. Rupp K 40 Years of Microprocessor Trend Data | Karl Rupp. <https://www.karlrupp.net/2015/06/40-years-of-microprocessor-trend-data/>. Accessed 2 May 2017
33. Kimball GE (1935) The Electronic Structure of Diamond. *J Chem Phys* 3:560–564. doi: 10.1063/1.1749729
34. Jung HK, Taniguchi K, Hamaguchi C (1996) Impact ionization model for full band Monte Carlo simulation in GaAs. *J Appl Phys* 79:2473–2480. doi: 10.1063/1.361176
35. Zhang SB (2002) The microscopic origin of the doping limits in semiconductors and wide-gap materials and recent developments in overcoming these limits: a review. *J Phys Condens Matter* 14:R881. doi: 10.1088/0953-8984/14/34/201
36. Joseph M, Tabata H, Kawai T (1999) p-Type Electrical Conduction in ZnO Thin Films by Ga and N Codoping. *Jpn J Appl Phys* 38:L1205. doi: 10.1143/JJAP.38.L1205
37. Korotkov RY, Gregie JM, Wessels BW (2001) Electrical properties of p-type GaN:Mg codoped with oxygen. *Appl Phys Lett* 78:222–224. doi: 10.1063/1.1335542
38. Katayama-Yoshida H, Nishimatsu T, Yamamoto T, Orita N (2001) Codoping method for the fabrication of low-resistivity wide band-gap semiconductors in p-type GaN, p-type AlN and n-type diamond: prediction versus experiment. *J Phys Condens Matter* 13:8901. doi: 10.1088/0953-8984/13/40/304
39. Lind AG, Jr HLA, Jones KS, Hatem C (2015) Co-implantation of Al<sup>+</sup>, P<sup>+</sup>, and S<sup>+</sup> with Si<sup>+</sup> implants into In<sub>0.53</sub>Ga<sub>0.47</sub>As. *J Vac Sci Technol B* 33:051217. doi: 10.1116/1.4931030
40. Mizushima I (1998) Precipitation of Boron in Highly Boron-Doped Silicon. *Jpn J Appl Phys* 37:1171. doi: 10.1143/JJAP.37.1171
41. Olesinski RW, Abbaschian GJ (1984) The B- Si (Boron-Silicon) system. *J Phase Equilibria* 5:478–484.

42. Vailionis A, Glass G, Desjardins P, et al (1999) Electrically Active and Inactive B Lattice Sites in Ultrahighly B Doped Si(001): An X-Ray Near-Edge Absorption Fine-Structure and High-Resolution Diffraction Study. *Phys Rev Lett* 82:4464–4467. doi: 10.1103/PhysRevLett.82.4464
43. Hurle DTJ (1999) A comprehensive thermodynamic analysis of native point defect and dopant solubilities in gallium arsenide. *J Appl Phys* 85:6957–7022. doi: 10.1063/1.370506
44. Hurle DTJ (2010) A thermodynamic analysis of native point defect and dopant solubilities in zinc-blende III–V semiconductors. *J Appl Phys* 107:121301. doi: 10.1063/1.3386412
45. Kressel H, Hawrylo FZ, Abrahams MS, Buiocchi CJ (1968) Observations Concerning Radiative Efficiency and Deep-Level Luminescence in n-Type GaAs Prepared by Liquid-Phase Epitaxy. *J Appl Phys* 39:5139–5144. doi: 10.1063/1.1655934
46. Grinshtein PM, Lipkes MA, Rytova NS, Fistul VI (1975) Investigation of the Kinetics of Precipitation of a Supersaturated Solid Solution of Te in GaAs. *Sov Phys-Semicond* 9:725–728.
47. Walukiewicz W (1988) Mechanism of Fermi-level stabilization in semiconductors. *Phys Rev B* 37:4760–4763. doi: 10.1103/PhysRevB.37.4760
48. Northrup JE, Zhang SB (1994) Energetics of the As vacancy in GaAs: The stability of the 3+ charge state. *Phys Rev B* 50:4962–4964. doi: 10.1103/PhysRevB.50.4962
49. Tan TY, You H-M, Gösele UM (1993) Thermal equilibrium concentrations and effects of negatively charged Ga vacancies in n-type GaAs. *Appl Phys A* 56:249–258. doi: 10.1007/BF00539483
50. Phil Won Yu (1982) Deep-center photoluminescence in undoped semi-insulating GaAs: 0.68 eV band due to the main deep donor. *Solid State Commun* 43:953–956. doi: 10.1016/0038-1098(82)90937-1
51. Chiang SY, Pearson GL (1975) Photoluminescence studies of vacancies and vacancy-impurity complexes in annealed GaAs. *J Lumin* 10:313–322. doi: 10.1016/0022-2313(75)90054-X
52. Rossi JA, Wolfe CM, Dimmock JO (1970) Acceptor Luminescence in High-Purity n-Type GaAs. *Phys Rev Lett* 25:1614–1617. doi: 10.1103/PhysRevLett.25.1614
53. Pankove JI (1968) Cathodoluminescence of n-Type GaAs. *J Appl Phys* 39:5368–5371. doi: 10.1063/1.1655984

54. Williams EW (1968) Evidence for Self-Activated Luminescence in GaAs: The Gallium Vacancy-Donor Center. *Phys Rev* 168:922–928. doi: 10.1103/PhysRev.168.922
55. Pons D, Bourgoin JC (1985) Irradiation-induced defects in GaAs. *J Phys C Solid State Phys* 18:3839. doi: 10.1088/0022-3719/18/20/012
56. Laine T, Saarinen K, Mäkinen J, et al (1996) Observation of compensating Ga vacancies in highly Si-doped GaAs. *Phys Rev B* 54:R11050–R11053. doi: 10.1103/PhysRevB.54.R11050
57. Laine T, Saarinen K, Hautojärvi P, et al (1999) Defects in GaAs grown by molecular-beam epitaxy at low temperatures: stoichiometry, doping, and deactivation of n-type conductivity. *J Appl Phys* 86:1888–1897. doi: 10.1063/1.370984
58. Schuppler S, Adler DL, Pfeiffer LN, et al (1995) Identifying and quantifying point defects in semiconductors using x-ray-absorption spectroscopy: Si-doped GaAs. *Phys Rev B* 51:10527–10538. doi: 10.1103/PhysRevB.51.10527
59. Chadi DJ, Citrin PH, Park CH, et al (1997) Fermi-Level-Pinning Defects in Highly  $n$ -Doped Silicon. *Phys Rev Lett* 79:4834–4837. doi: 10.1103/PhysRevLett.79.4834
60. Sette F, Pearton SJ, Poate JM, et al (1986) Local structure of S impurities in GaAs. *Phys Rev Lett* 56:2637.
61. Chadi DJ, Chang KJ (1989) Energetics of DX-center formation in GaAs and  $\text{Al}_x\text{Ga}_{1-x}\text{As}$  alloys. *Phys Rev B* 39:10063–10074. doi: 10.1103/PhysRevB.39.10063
62. Ma J, Wei S-H (2013) Electron-limiting defect complex in hyperdoped GaAs: The  $\text{Si}_2\text{V}_{\text{Ga}}$  center. *Phys Rev B* 87:115210. doi: 10.1103/PhysRevB.87.115210
63. Neave JH, Dobson PJ, Harris JJ, et al (1983) Silicon doping of MBE-grown GaAs films. *Appl Phys A* 32:195–200. doi: 10.1007/BF00820260
64. Schuppler S, Adler DL, Pfeiffer LN, et al (1993) Can electrical deactivation of highly Si-doped GaAs be explained by autocompensation? *Appl Phys Lett* 63:2357–2359. doi: 10.1063/1.110500
65. Domke C, Ebert P, Heinrich M, Urban K (1996) Microscopic identification of the compensation mechanisms in Si-doped GaAs. *Phys Rev B* 54:10288–10291. doi: 10.1103/PhysRevB.54.10288
66. Akintunde JA (1993) Effects of heat treatments on the electrical properties of Te-implanted laser-annealed GaAs. *Phys Status Solidi A* 140:501–508. doi: 10.1002/pssa.2211400221



67. Tang ACT, Sealy BJ, Rezazadeh AA (1990) The influence of heat treatment on the electrical characteristics of selenium-implanted GaAs. *J Appl Phys* 67:307–311. doi: 10.1063/1.345253
68. Chen CY, Cohen RM (1996) Zn solubility limit in GaAs: growth versus equilibrium. *J Cryst Growth* 167:17–23. doi: 10.1016/0022-0248(96)00203-5
69. Porter DA, Easterling KE, Sherif M (2009) *Phase Transformations in Metals and Alloys*, Third Edition, 3 edition. CRC Press, Boca Raton, FL
70. Fuller CS, Wolfstirn KB (1962) Diffusion, Solubility, and Electrical Behavior of Li in GaAs Single Crystals. *J Appl Phys* 33:2507–2514. doi: 10.1063/1.1729005
71. Fuller CS, Wolfstirn KB (1963) Changes in Electron Concentration of Donor-Doped GaAs Crystals Caused by Annealing. *J Appl Phys* 34:2287–2289. doi: 10.1063/1.1702731
72. Lietoila A, Gibbons JF, Magee TJ, et al (1979) Solid solubility of As in Si as determined by ion implantation and cw laser annealing. *Appl Phys Lett* 35:532–534. doi: 10.1063/1.91198
73. Tsuchiya T, Nagai H, Meguro T, Sakaguchi H (1994) Thermal stability of highly Se-doped specular surface of In<sub>0.5</sub>Ga<sub>0.5</sub>As grown by low-pressure metalorganic vapor phase epitaxy. *J Cryst Growth* 145:403–407. doi: 10.1016/0022-0248(94)91083-9
74. Takamura Y, Jain SH, Griffin PB, Plummer JD (2002) Thermal stability of dopants in laser annealed silicon. *J Appl Phys* 92:230–234. doi: 10.1063/1.1481975
75. Sorg V, Zhang SN, Hill M, et al (2015) (Invited) Dopant Activation and Deactivation in InGaAs during Sub-Millisecond Thermal Annealing. *ECS Trans* 66:117–124. doi: 10.1149/06604.0117ecst
76. Lind AG, Aldridge HL, Bomberger CC, et al (2015) Annealing Effects on the Electrical Activation of Si Dopants in InGaAs. *ECS Trans* 66:23–27. doi: 10.1149/06607.0023ecst
77. Lind AG, Aldridge Jr HL, Bomberger CC, et al (2015) Comparison of thermal annealing effects on electrical activation of MBE grown and ion implant Si-doped In<sub>0.53</sub>Ga<sub>0.47</sub>As. *J Vac Sci Technol B* 33:021206. doi: 10.1116/1.4914319
78. Watkins GD (2000) Intrinsic defects in silicon. *Mater Sci Semicond Process* 3:227–235. doi: 10.1016/S1369-8001(00)00037-8
79. Brudnyi VN, Kolin NG, Potapov AI (2003) Electrical properties of InAs irradiated with protons. *Semiconductors* 37:390–395. doi: 10.1134/1.1568456

80. Brudnyi VN, Kolin NG, Smirnov LS (2007) The model of self-compensation and pinning of the Fermi level in irradiated. Semiconductors 41:1011–1020. doi: 10.1134/S1063782607090023
81. Wendler E (2009) Mechanisms of damage formation in semiconductors. Nucl Instrum Methods Phys Res Sect B Beam Interact Mater At 267:2680–2689. doi: 10.1016/j.nimb.2009.05.059
82. CZOCHRALSKI J (1918) Ein neues Verfahren zur Messung der Kristallisationsgeschwindigkeit der Metalle. Z Phys Chem 92:219–221.
83. Teal GK, Little JB (1950) Growth of germanium single crystals. In: Phys. Rev. AMERICAN PHYSICAL SOC ONE PHYSICS ELLIPSE, COLLEGE PK, MD 20740-3844 USA, pp 647–647
84. Zulehner W (1983) Czochralski growth of silicon. J Cryst Growth 65:189–213. doi: 10.1016/0022-0248(83)90051-9
85. Bridgman PW (1925) Certain Physical Properties of Single Crystals of Tungsten, Antimony, Bismuth, Tellurium, Cadmium, Zinc, and Tin. Proc Am Acad Arts Sci 60:305–383. doi: 10.2307/25130058
86. Stockbarger DC (1936) The Production of Large Single Crystals of Lithium Fluoride. Rev Sci Instrum 7:133–136. doi: 10.1063/1.1752094
87. Metz EPA, Miller RC, Mazelsky R (1962) A Technique for Pulling Single Crystals of Volatile Materials. J Appl Phys 33:2016–2017. doi: 10.1063/1.1728885
88. Weiner ME, Lassota DT, Schwartz B (1971) Liquid Encapsulated Czochralski Growth of GaAs. J Electrochem Soc 118:301–306. doi: 10.1149/1.2408023
89. Gladkov P, Monova E, Weber J (1993) Liquid phase epitaxy of n-type GaAs from Bi solution. J Appl Phys 74:5020–5024. doi: 10.1063/1.354308
90. Williams JS (1983) Solid phase epitaxial regrowth phenomena in silicon. Nucl Instrum Methods Phys Res 209:219–228. doi: 10.1016/0167-5087(83)90803-7
91. Campisano SU, Rimini E, Baeri P, Foti G (1980) Supersaturated solid solutions after solid phase epitaxial growth in Bi-implanted silicon. Appl Phys Lett 37:170–172. doi: 10.1063/1.91812
92. Blood P, Brown WL, Miller GL (1979) Incorporation of implanted In and Sb in silicon during amorphous layer regrowth. J Appl Phys 50:173–182. doi: 10.1063/1.325686
93. Gamo K, Inada T, Mayer JW, et al (1977) Reordering of implanted amorphous layers in gaas. Radiat Eff 33:85–89. doi: 10.1080/00337577708237472

94. Licoppe C, Nissim Y i., Meriadec C, Krauz P (1986) Interface structure evolution and impurity effects during solid-phase-epitaxial growth in GaAs. *J Appl Phys* 60:1352–1358. doi: 10.1063/1.337309
95. Belay KB, Llewellyn DJ, Ridgway MC (1996) Solid-phase epitaxial growth of amorphized GaAs: The influence of macroscopic nonstoichiometry. *Appl Phys Lett* 69:2534–2536. doi: 10.1063/1.117730
96. Bhattacharya RS, Rai AK, Pronoko PP, et al (1983) Damage annealing behavior of Se implanted GaAs. *J Phys Chem Solids* 44:61–69. doi: 10.1016/0022-3697(83)90031-8
97. Kular SS, Sealy BJ, Stephens KG, et al (1980) Electrical, Rutherford backscattering and transmission electron microscopy studies of furnace annealed zinc implanted GaAs. *Solid-State Electron* 23:831–838. doi: 10.1016/0038-1101(80)90099-4
98. Sadana DK (1985) Mechanisms of amorphization and recrystallization in ion implanted III–V compound semiconductors. *Nucl Instrum Methods Phys Res Sect B Beam Interact Mater At* 7:375–386. doi: 10.1016/0168-583X(85)90585-3
99. Woodhouse JD, Donnelly JP, Nitishin PM, et al (1984) Annealing of damage in Se+-implanted indium phosphide. *Solid-State Electron* 27:677–686. doi: 10.1016/0038-1101(84)90139-4
100. Pearson SJ (1993) Ion implantation in III–V semiconductor technology. *Int J Mod Phys B* 7:4687–4761.
101. Lind AG, Rudawski NG, Vito NJ, et al (2013) Maximizing electrical activation of ion-implanted Si in In<sub>0.53</sub>Ga<sub>0.47</sub>As. *Appl Phys Lett* 103:232102. doi: 10.1063/1.4835097
102. Gwilliam RM, Anjum M, Sealy BJ, et al (1996) Electrical characterisation of magnesium and tellurium implanted indium gallium arsenide. In: *Proc. 11th Int. Conf. Ion Implant. Technol.* pp 702–704
103. Foxon CT, Harvey JA, Joyce BA (1973) The evaporation of GaAs under equilibrium and non-equilibrium conditions using a modulated beam technique. *J Phys Chem Solids* 34:1693–1701. doi: 10.1016/S0022-3697(73)80135-0
104. Tsong TT (2001) Mechanisms of surface diffusion. *Prog Surf Sci* 67:235–248. doi: 10.1016/S0079-6816(01)00026-0
105. Ehrlich G, Hudda FG (1966) Atomic View of Surface Self-Diffusion: Tungsten on Tungsten. *J Chem Phys* 44:1039–1049. doi: 10.1063/1.1726787
106. Schwoebel RL, Shipsey EJ (1966) Step Motion on Crystal Surfaces. *J Appl Phys* 37:3682–3686. doi: 10.1063/1.1707904

107. Schwoebel RL (1969) Step Motion on Crystal Surfaces. II. *J Appl Phys* 40:614–618. doi: 10.1063/1.1657442
108. Grandjean N, Massies J (1993) Epitaxial growth of highly strained  $\text{In}_x\text{Ga}_{1-x}\text{As}$  on  $\text{GaAs}(001)$ : the role of surface diffusion length. *J Cryst Growth* 134:51–62. doi: 10.1016/0022-0248(93)90008-K
109. Massies J, Grandjean N, Etgens VH (1992) Surfactant mediated epitaxial growth of  $\text{In}_x\text{Ga}_{1-x}\text{As}$  on  $\text{GaAs}(001)$ . *Appl Phys Lett* 61:99–101. doi: 10.1063/1.107626
110. Heckingbottom R, Todd CJ, Davies GJ (1980) The Interplay of Thermodynamics and Kinetics in Molecular Beam Epitaxy (MBE) of Doped Gallium Arsenide. *J Electrochem Soc* 127:444–450. doi: 10.1149/1.2129685
111. Chai YG, Chow R, Wood CEC (1981) The effect of growth conditions on Si incorporation in molecular beam epitaxial  $\text{GaAs}$ . *Appl Phys Lett* 39:800–803. doi: 10.1063/1.92562
112. Massies J, Grandjean N (1993) Surfactant effect on the surface diffusion length in epitaxial growth. *Phys Rev B* 48:8502–8505. doi: 10.1103/PhysRevB.48.8502
113. Heckingbottom R, Davies GJ, Prior KA (1983) Growth and doping of gallium arsenide using molecular beam epitaxy (MBE): Thermodynamic and kinetic aspects. *Surf Sci* 132:375–389. doi: 10.1016/0039-6028(83)90548-4
114. Baraskar A, Jain V, Wistey MA, et al (2010) High doping effects on in-situ Ohmic contacts to n- $\text{InAs}$ . In: 2010 Int. Conf. Indium Phosphide Relat. Mater. IPRM. pp 1–4
115. Dormaier R, Mohny SE (2012) Factors controlling the resistance of Ohmic contacts to n- $\text{InGaAs}$ . *J Vac Sci Technol B* 30:031209. doi: 10.1116/1.4705730
116. Law JJM, Carter AD, Lee S, et al (2013) Co-doping of  $\text{In}_x\text{Ga}_{1-x}\text{As}$  with silicon and tellurium for improved ultra-low contact resistance. *J Cryst Growth* 378:92–95. doi: 10.1016/j.jcrysgro.2012.12.122
117. Baraskar AK, Wistey MA, Jain V, et al (2009) Ultralow resistance, nonalloyed Ohmic contacts to n- $\text{InGaAs}$ . *J Vac Sci Technol B* 27:2036–2039. doi: 10.1116/1.3182737
118. Stareev G, Künzel H, Dortmann G (1993) A controllable mechanism of forming extremely low-resistance nonalloyed ohmic contacts to group III-V compound semiconductors. *J Appl Phys* 74:7344–7356. doi: 10.1063/1.355002
119. Lin JC, Yu SY, Mohny SE (2013) Characterization of low-resistance ohmic contacts to n- and p-type  $\text{InGaAs}$ . *J Appl Phys* 114:044504. doi: 10.1063/1.4816097

120. Seshan K (2001) Handbook of Thin Film Deposition. William Andrew
121. Glew RW (1984) Zinc Doping of MOCVD GaAs. *J Cryst Growth* 68:44–47. doi: 10.1016/0022-0248(84)90395-6
122. Stringfellow GB (1984) A critical appraisal of growth mechanisms in MOVPE. *J Cryst Growth* 68:111–122. doi: 10.1016/0022-0248(84)90405-6
123. Hersee SD, Duchemin JP (1982) Low-Pressure Chemical Vapor Deposition. *Annu Rev Mater Sci* 12:65–80. doi: 10.1146/annurev.ms.12.080182.000433
124. Tao M (2000) A kinetic model for metalorganic chemical vapor deposition from trimethylgallium and arsine. *J Appl Phys* 87:3554–3562. doi: 10.1063/1.372380
125. Dapkus PD (1982) Metal Organic Chemical Vapor Deposition. *Annu Rev Mater Sci* 12:243.
126. Seki H, Koukitu A (1986) Thermodynamic analysis of metalorganic vapor phase epitaxy of III–V alloy semiconductors. *J Cryst Growth* 74:172–180. doi: 10.1016/0022-0248(86)90261-7
127. Keizer LC, Tang X, van Meerten RZC, Giling LJ (1990) Doping of gallium arsenide in MOCVD: Equilibrium calculations. *J Cryst Growth* 102:667–677. doi: 10.1016/0022-0248(90)90427-M
128. Stringfellow GB (1986) The role of impurities in III/V semiconductors grown by organometallic vapor phase epitaxy. *J Cryst Growth* 75:91–100. doi: 10.1016/0022-0248(86)90229-0
129. Veuhoff E, Kuech TF, Meyerson BS (1985) A Study of Silicon Incorporation in GaAs MOCVD Layers. *J Electrochem Soc* 132:1958–1961. doi: 10.1149/1.2114261
130. Mashita M (1989) Mass Spectrometric Studies on Silicon Doping of OMVPE GaAs. *Jpn J Appl Phys* 28:1298. doi: 10.1143/JJAP.28.1298
131. Orzali T, Vert A, Lee RTP, et al (2015) Heavily tellurium doped n-type InGaAs grown by MOCVD on 300 mm Si wafers. *J Cryst Growth* 426:243–247. doi: 10.1016/j.jcrysgro.2015.05.007
132. Jiang L, Lin T, Wei X, et al (2004) Effects of V/III ratio on InGaAs and InP grown at low temperature by LP-MOCVD. *J Cryst Growth* 260:23–27. doi: 10.1016/j.jcrysgro.2003.08.013
133. Chichibu S, Iwai A, Matsumoto S, Higuchi H (1992) Heavily Si-doped GaAs grown by low-pressure metalorganic chemical vapor deposition using tertiarybutylarsine and silane. *Appl Phys Lett* 60:489–491. doi: 10.1063/1.106645

134. Eisen FH, Welch BM, Müller H, et al (1977) Tellurium implantation in GaAs. *Solid-State Electron* 20:219–223. doi: 10.1016/0038-1101(77)90187-3
135. Pashley RD, Welch BM (1975) Tellurium-implanted N<sup>+</sup> layers in GaAs. *Solid-State Electron* 18:977–981. doi: 10.1016/0038-1101(75)90115-X
136. Hayt W, Buck J (2011) *Engineering Electromagnetics*, 8 edition. McGraw-Hill Education, New York, NY
137. Hall EH (1879) On a New Action of the Magnet on Electric Currents. *Am J Math* 2:287–292. doi: 10.2307/2369245
138. van der PAUW L (1958) A method of measuring specific resistivity and Hall effect of discs of arbitrary shape. *Philips Res Rep* 13:1–9.
139. Secula EM (2010) Resistivity and Hall Measurements. In: NIST. <https://www.nist.gov/pml/engineering-physics-division/resistivity-and-hall-measurements>. Accessed 22 May 2017
140. Jain SH, Griffin PB, Plummer JD (2003) Hall measurements of bilayer structures. *J Appl Phys* 93:1060–1063. doi: 10.1063/1.1529093
141. Williams DB, Carter CB (2009) *Transmission Electron Microscopy: A Textbook for Materials Science*, 2nd edition. Springer, New York
142. Fultz B, Howe J (2012) *Transmission Electron Microscopy and Diffractometry of Materials*, 4th ed. 2013 edition. Springer, Heidelberg ; New York
143. Giannuzzi LA, Stevie FA (2005) *Introduction to focused ion beams: instrumentation, theory, techniques, and practice*. Springer, New York
144. Park Y c., Park B c., Romankov S, et al (2014) Use of permanent marker to deposit a protection layer against FIB damage in TEM specimen preparation. *J Microsc* 255:180–187. doi: 10.1111/jmi.12150
145. Giannuzzi LA, Stevie FA (1999) A review of focused ion beam milling techniques for TEM specimen preparation. *Micron* 30:197–204. doi: 10.1016/S0968-4328(99)00005-0
146. Schaffer M, Schaffer B, Ramasse Q (2012) Sample preparation for atomic-resolution STEM at low voltages by FIB. *Ultramicroscopy* 114:62–71. doi: 10.1016/j.ultramic.2012.01.005
147. Mayer J, Giannuzzi LA, Kamino T, Michael J (2007) TEM Sample Preparation and FIB-Induced Damage. *MRS Bull* 32:400–407. doi: 10.1557/mrs2007.63
148. Pecharsky V, Zavalij P (2008) *Fundamentals of Powder Diffraction and Structural Characterization of Materials*, Second Edition, 2 edition. Springer US

149. Vickerman JC, Brown A, Reed NM (1990) Secondary Ion Mass Spectrometry: Principles and Applications. Oxford University Press, Oxford : Oxford ; New York
150. Benninghoven A, Rudenauer FG, Werner HW (1987) Secondary Ion Mass Spectrometry: Basic Concepts, Instrumental Aspects, Applications and Trends, 1 edition. Wiley-Interscience, New York
151. Hwang JC (1969) Effect of Heat Treatment on Photoluminescence of Te Doped GaAs. J Appl Phys 40:1983–1984. doi: 10.1063/1.1657885
152. Hutchinson PW, Dobson PS (1975) Interstitial condensation in n+ GaAs. J Mater Sci 10:1636–1641. doi: 10.1007/BF01031865
153. Verner VD, Maksimov SK, Nichugovskii DK (1976) The nature of defects of crystalline structure in GaAs heavily doped with Te. Phys Status Solidi A 33:755–763. doi: 10.1002/pssa.2210330235
154. Hutchinson PW, Dobson PS (1978) Preferential precipitation on dislocation loops in Te-doped gallium arsenide. Philos Mag A 38:15–23. doi: 10.1080/01418617808239214
155. Hughes B, Narayanan GH (1978) On annealing-induced prismatic dislocation loops and electrical changes in heavily Te-doped GaAs. Phys Status Solidi A 46:627–637. doi: 10.1002/pssa.2210460228
156. Pearton SJ, Williams JS, Short KT, et al (1989) Implantation temperature dependence of electrical activation, solubility, and diffusion of implanted Te, Cd, and Sn in GaAs. J Appl Phys 65:1089–1098. doi: 10.1063/1.343044
157. Fewster PF (1981) A defect model for undoped and tellurium doped gallium arsenide. J Phys Chem Solids 42:883–889. doi: 10.1016/0022-3697(81)90013-5
158. Farrow RFC (1974) The evaporation of InP under Knudsen (equilibrium) and Langmuir (free) evaporation conditions. J Phys Appl Phys 7:2436. doi: 10.1088/0022-3727/7/17/318
159. Arthur JR (1967) Vapor pressures and phase equilibria in the Ga–As system. J Phys Chem Solids 28:2257–2267. doi: 10.1016/0022-3697(67)90251-X
160. Haynes TE, Chu WK, Aselage TL, Picraux ST (1986) Initial decomposition of GaAs during rapid thermal annealing. Appl Phys Lett 49:666–668. doi: 10.1063/1.97562
161. Haynes TE, Chu WK, Picraux ST (1987) Direct measurement of evaporation during rapid thermal processing of capped GaAs. Appl Phys Lett 50:1071–1073. doi: 10.1063/1.97973

162. Campbell PM, Aina O, Baliga BJ (1986) Prevention of thermal surface damage in GaAs by encapsulated annealing in an arsine ambient. *J Electron Mater* 15:125–131. doi: 10.1007/BF02655325
163. del Alamo JA, Mizutani T (1987) Rapid thermal annealing of InP using GaAs and InP proximity caps. *J Appl Phys* 62:3456–3458. doi: 10.1063/1.339316
164. Armiento CA, Prince FC (1986) Capless rapid thermal annealing of GaAs using an enhanced overpressure proximity technique. *Appl Phys Lett* 48:1623–1625. doi: 10.1063/1.96837
165. Oberstar JD, Streetman BG (1983) Thin film encapsulants for annealing GaAs and InP. *Thin Solid Films* 103:17–26. doi: 10.1016/0040-6090(83)90421-2
166. Gyulai J, Mayer JW, Mitchell IV, Rodriguez V (1970) Outdiffusion through silicon oxide and silicon nitride layers on gallium arsenide. *Appl Phys Lett* 17:332–334. doi: 10.1063/1.1653422
167. Lile DL, Collins DA, Zeisse CR (1983) Transient annealing of indium phosphide. *IEEE Electron Device Lett* 4:231–233. doi: 10.1109/EDL.1983.25715
168. Puurunen RL (2005) Surface chemistry of atomic layer deposition: A case study for the trimethylaluminum/water process. *J Appl Phys* 97:121301. doi: 10.1063/1.1940727
169. Hwang CS (2014) Atomic Layer Deposition for Semiconductors. doi: 10.1007/978-1-4614-8054-9
170. ASM International (1990) ASM handbook, 10th edition. ASM International, Materials Park, Ohio
171. Mullin JB, Straughan BW, Driscoll CMH, Willoughby AFW (1976) Lattice superdilation phenomena in doped GaAs. *J Appl Phys* 47:2584–2587. doi: 10.1063/1.322977
172. Bak-Misiuk J, Leszczynski M, Domagala J, Zytewicz Z (1995) Lattice constants and thermal expansion of  $\text{Al}_x\text{Ga}_{1-x}\text{As:Te}$ . *J Appl Phys* 78:6994–6998. doi: 10.1063/1.360467
173. Drozdov YN, Danil'tsev VM, Drozdov MN, et al (2017) Investigation of X-ray diffraction limitations upon the analysis of tellurium-atom injection into GaAs epitaxial layers. *J Surf Invest X-Ray Synchrotron Neutron Tech* 11:361–365. doi: 10.1134/S1027451017020069
174. Ayers JE (1994) The measurement of threading dislocation densities in semiconductor crystals by X-ray diffraction. *J Cryst Growth* 135:71–77. doi: 10.1016/0022-0248(94)90727-7



175. Paquette B, Ilahi B, Aimez V, Arès R (2013) Inhibition of Te surfactant effect on surface morphology of heavily Te-doped GaAs. *J Cryst Growth* 383:30–35. doi: 10.1016/j.jcrysgro.2013.08.015
176. Hennen L, Granneman EHA, Kessels WMM (2012) Analysis of blister formation in spatial ALD Al<sub>2</sub>O<sub>3</sub> for silicon surface passivation. In: 2012 38th IEEE Photovolt. Spec. Conf. pp 001049–001054
177. Vermang B, Goverde H, Simons V, et al (2012) A study of blister formation in ALD Al<sub>2</sub>O<sub>3</sub> grown on silicon. In: 2012 38th IEEE Photovolt. Spec. Conf. pp 001135–001138
178. Glicksman ME (1999) *Diffusion in Solids: Field Theory, Solid-State Principles, and Applications*, 1 edition. Wiley-Interscience, New York
179. Karelina TA, Lavrishchev TT, Prihod'ko GL, Khludkov SS (1974) Diffusion of tellurium in GaAs. *Izv Akad Nauk SSSR Neorganicheskie Mater* 10:228–230.
180. Su YK, Chou YC, Chang CY (1986) Investigation of Se-doped GaAs epilayers grown by low-pressure metal-organic chemical vapor deposition. *J Phys Chem Solids* 47:105–108. doi: 10.1016/0022-3697(86)90184-8
181. Willardson RK, Goering HL (1962) *Compound Semiconductors, Volume 1: Preparation of III-V Compounds*. Reinhold Pub. Corp., New York
182. Uematsu M, Wada K, Gösele U (1992) Non-equilibrium point defect phenomena influencing beryllium and zinc diffusion in GaAs and related compounds. *Appl Phys A* 55:301–312. doi: 10.1007/BF00324076
183. Deppe DG, Holonyak N, Plano WE, et al (1988) Impurity diffusion and layer interdiffusion in Al<sub>x</sub>Ga<sub>1-x</sub>As-GaAs heterostructures. *J Appl Phys* 64:1838–1844. doi: 10.1063/1.341759
184. Yu S, Gösele UM, Tan TY (1989) A model of Si diffusion in GaAs based on the effect of the Fermi level. *J Appl Phys* 66:2952–2961. doi: 10.1063/1.344176
185. Dąbrowski J, Northrup JE (1994) Microscopic theory of diffusion on the Ga sublattice of GaAs: Vacancy-assisted diffusion of Si and Ga. *Phys Rev B* 49:14286–14289. doi: 10.1103/PhysRevB.49.14286
186. Murray JJ, Deal MD, Allen EL, et al (1992) Modeling Silicon Diffusion in GaAs Using Well Defined Silicon Doped Molecular Beam Epitaxy Structures. *J Electrochem Soc* 139:2037–2041. doi: 10.1149/1.2221170
187. Aldridge H, Lind AG, Bomberger CC, et al (2016) Implantation and Diffusion of Silicon Marker Layers in In<sub>0.53</sub>Ga<sub>0.47</sub>As. *J Electron Mater* 45:4282–4287. doi: 10.1007/s11664-016-4616-0

188. Aldridge Jr HL, Lind AG, Law ME, et al (2014) Concentration-dependent diffusion of ion-implanted silicon in  $\text{In}_{0.53}\text{Ga}_{0.47}\text{As}$ . *Appl Phys Lett* 105:042113. doi: 10.1063/1.4892079
189. Lee J, Wei L, Tanigawa S, Kawabe M (1991) Impurity effects on both the creation and the migration of Ga vacancies in GaAs. *J Appl Phys* 70:674–684. doi: 10.1063/1.349647
190. Aziz MJ (1998) Pressure and Stress Effects on Diffusion in Si. *Defect Diffus Forum* 153–155:1–10. doi: 10.4028/www.scientific.net/DDF.153-155.1
191. Park H, Jones KS, Slinkman JA, Law ME (1995) Effects of hydrostatic pressure on dopant diffusion in silicon. *J Appl Phys* 78:3664–3670.
192. Zhao Y, Aziz MJ, Gossmann H-J, et al (1998) Activation volume for boron diffusion in silicon and implications for strained films. *Appl Phys Lett* 74:31–33. doi: 10.1063/1.123123
193. Bonapasta AA, Giannozzi P (2000) Effects of Strain and Local Charge on the Formation of Deep Defects in III-V Ternary Alloys. *Phys Rev Lett* 84:3923–3926. doi: 10.1103/PhysRevLett.84.3923
194. Osada K, Zaitsev Y, Matsumoto S, et al (1995) Effect of Stress in the Deposited Silicon Nitride Films on Boron Diffusion of Silicon. *J Electrochem Soc* 142:202–206. doi: 10.1149/1.2043867
195. Ahn ST, Kennel HW, Plummer JD, Tiller WA (1988) Film stress-related vacancy supersaturation in silicon under low-pressure chemical vapor deposited silicon nitride films. *J Appl Phys* 64:4914–4919. doi: 10.1063/1.342441
196. Hess DW (1984) Plasma-enhanced CVD: Oxides, nitrides, transition metals, and transition metal silicides. *J Vac Sci Technol A* 2:244–252. doi: 10.1116/1.572734
197. Tarraf A, Daleiden J, Irmer S, et al (2004) Stress investigation of PECVD dielectric layers for advanced optical MEMS. *J Micromechanics Microengineering* 14:317. doi: 10.1088/0960-1317/14/3/001
198. Ghrib A, Kersauson M de, Kurdi ME, et al (2012) Control of tensile strain in germanium waveguides through silicon nitride layers. *Appl Phys Lett* 100:201104. doi: 10.1063/1.4718525
199. Claassen W a. P, Valkenburg WGJN, Willemsen MFC, Wijgert WM v d (1985) Influence of Deposition Temperature, Gas Pressure, Gas Phase Composition, and RF Frequency on Composition and Mechanical Stress of Plasma Silicon Nitride Layers. *J Electrochem Soc* 132:893–898. doi: 10.1149/1.2113980

200. Cianci E, Schina A, Minotti A, et al (2006) Dual frequency PECVD silicon nitride for fabrication of CMUTs' membranes. *Sens Actuators Phys* 127:80–87. doi: 10.1016/j.sna.2005.11.053
201. Jones KS, Prussin S, Weber ER (1988) A systematic analysis of defects in ion-implanted silicon. *Appl Phys A* 45:1–34. doi: 10.1007/BF00618760
202. Akano UG, Mitchell IV, Shepherd FR, Miner CJ (1995) Ion implantation damage of InP and InGaAs. *Nucl Instrum Methods Phys Res Sect B Beam Interact Mater At* 106:308–312. doi: 10.1016/0168-583X(95)00724-5
203. Lee SR, Wright AF, Modine NA, et al (2015) First-principles survey of the structure, formation energies, and transition levels of As-interstitial defects in InGaAs. *Phys Rev B*. doi: 10.1103/PhysRevB.92.045205
204. Sholl D, Steckel JA (1993) *Density Functional Theory: A Practical Introduction*, 1st ed. Wiley-Interscience, Hoboken, New Jersey
205. Hohenberg P, Kohn W (1964) Inhomogeneous Electron Gas. *Phys Rev* 136:B864–B871. doi: 10.1103/PhysRev.136.B864
206. Kohn W, Sham LJ (1965) Self-Consistent Equations Including Exchange and Correlation Effects. *Phys Rev* 140:A1133–A1138. doi: 10.1103/PhysRev.140.A1133
207. Perdew JP, Zunger A (1981) Self-interaction correction to density-functional approximations for many-electron systems. *Phys Rev B* 23:5048.
208. Van de Walle CG, Neugebauer J (2004) First-principles calculations for defects and impurities: Applications to III-nitrides. *J Appl Phys* 95:3851–3879. doi: 10.1063/1.1682673
209. Fleszar A (2001) LDA, GW, and exact-exchange Kohn-Sham scheme calculations of the electronic structure of  $\text{sp}^3$  semiconductors. *Phys Rev B* 64:245204. doi: 10.1103/PhysRevB.64.245204
210. Kresse G, Joubert D (1999) From ultrasoft pseudopotentials to the projector augmented-wave method. *Phys Rev B* 59:1758.
211. Blöchl PE (1994) Projector augmented-wave method. *Phys Rev B* 50:17953–17979. doi: 10.1103/PhysRevB.50.17953
212. Kresse G, Hafner J (1993) Ab initio molecular dynamics for liquid metals. *Phys Rev B* 47:558–561. doi: 10.1103/PhysRevB.47.558

## BIOGRAPHICAL SKETCH

Ethan Kennon was born in Benicia, California and grew up loving math and science and wanted to become an astronaut or engineer. After graduating from Benicia High School in 2008, he pursued his interests in engineering by enrolling at the University of California, Davis. He completed his Bachelor's degree in Electronic Materials Engineering with a minor in French in June 2013. He then proceeded to the University of Florida to continue pursuing materials science under Dr. Kevin Jones. He completed his Master's in Materials Science and Engineering in May 2015, and continued his PhD work while simultaneously earning a Master's in Management in May 2017. Upon Completion of his PhD, he will be working at Keysight Technologies as an IC Product Engineer.